Frequency domain Lamb wave analysis for damage detection

Cardiff University

Frederick Andrew Faure Purcell

A thesis submitted in fulfilment for the degree of
Doctor of Philosophy

School of Engineering

March 2021

Abstract

Non-Destructive Testing (NDT) techniques are prevalent in the aerospace, green energy and automotive industries. With the ability to identify defects in service or at the manufacturing stage, NDT is a vital tool in creating safe and efficient structures. Existing NDT methods face many limitations when working with advanced materials such as composites. Further limitations are met by conventional NDT methods in terms of resolution, measurement time and levels of access required to the structure for measurements to be taken. This work presents the development of a band-pass mode filtering technique in the frequency wavenumber domain for the purpose of damage detection. Data were captured in the temporal and spatial domain using a 3D Scanning Laser Doppler Vibrometer (SLDV) with piezoelectric transducers exciting the structure with a variety of steady-state signals ranging in frequency. A thickness map or damage map was created based on the frequency and wavelength of the A_0 Lamb wave mode. The technique was first demonstrated on two aluminium specimens with dimensions of 400mm by 400mm with a thickness range of 0.5mm to 8mm with distinct geometric features. Using multi-frequency excitation combined with mode based filters, an estimation of thickness was achieved with a mean percentage thickness error of 15%. Circular thickness reductions with a diameter of 10mm were clearly identified at the maximum plate thickness of 8mm. The proposed mode filtering technique was furthered to work on highly non-isotropic composites using no prior knowledge of the material. Dispersion characteristics were taken from the measurement data and determined the shape of the mode filters. This method was demonstrated on three different composite specimens and was able to identify single ply changes in a fibre-glass specimen as well as a delamination defect in a carbon fibre plate. Multi-frequency steady-state excitation was also shown using multiple driving transducers on a single structure. Further work was completed to enable these techniques to function with wavefield data gained from non-developable surfaces. Through geometrical transforms of the wavefield it was shown that wave mode filtering could be completed on complex geometries. The application of wavenumber-based NDT was demonstrated to give highly accurate results with good spatial and depth resolution on parts with complex geometries, as well as composite and metallic parts. This work presented a new embodiment of wavenumber-based NDT that showed a significant step towards real world implementation and offers a number of advancements over existing techniques.

This thesis is dedicated to all those who believed I would get to where I am

Acknowledgements

I would also like to thank the EPSRC for funding this research. All my thanks goes to my amazing supervisors, Prof. Rhys Pullin, Dr. Mark Eaton and Dr. Matthew Pearson. Your support and belief in my ability has been second to none and has had an immeasurable impact on both the quality and the enjoyment of my work. A special thanks goes to Rhys who has been a pivotal part of my time at university. From getting me excited about engineering on interview day to taking me on as an extra dissertation student, all the way through to supporting and inspiring me to pursuit a PhD. I would also like thank Paul Leech and Garry Shipley for their support manufacturing samples.

A massive thanks goes to all those in the CUSP lab. Your willingness to share your knowledge and help never failed to humble me. You made the CUSP lab a fun, Nerf gun filled and inspiring place to work.

No small thanks goes to the boy band who simultaneously managed to be the most supportive friends and a terrible influence. University would not have been half the fun without you and I could not have asked for a better group of people to meet along the way. Special thanks to Rob and Rhoss who put up with me for those few extra years.

I was also lucky enough to meet Millie during my PhD. You have made the last few years the best and I can't really imaging doing things without you. Your support of me and my work, especially during lockdown, is what has got me through this write up in one piece, even having quite a lot of fun along the way.

Finally to my amazing family, I don't think it is possible to fully express my gratitude. My wonderful sister, you have been my biggest mentor and inspiration, from reading me books through to taking me to university open days. To my dad for nurturing my love of all things engineering and supporting me on all my adventures along the way. And finally to my mum, your unwavering belief in me is what has got me to where I am and given me the opportunities I now have. I don't know what I would have done without you.

Contents

List of Figures

List of Tables

Acronyms

AE	Acoustic Emission
ARAP	As-Rigid-As-Possible
AWS	Acoustic Wavenumber Spectroscopy
CM	Condition Monitoring
CNN	Convolutional Neural Networks
CT	Computerised Tomogrpahy
FEA	Finite Element Analysis
FFT	Fast Fourier Transform
FM	Frequency Modulated
FML	Fibre Metal Laminate
GFRP	Glass Fibre Reinforced Polymer
GLARE	Glass Laminate Aluminium Reinforced Epoxy
GMM	Global Matrix Method
IFFT	Inverse Fast Fourier Transform
IR	Infrared
IW	Instantaneous Wavenumber
LDV	Laser Doppler Vibrometer
LISA	Local Interaction Simulation Approach
MPE	Mean Percentage Error
NDT	Non-Distructive Testing
PVDF	polyvinylidine fluoride
PZT	Lead Zirconate Titrate
RMS	Root Mean Squared
SAFE	Semi Analytical Finite Element
SH	Shear Horizontal
SHM	Structural Health Monitoring
SLDV	Scanning Laser Doppler Vibrometer
TMM	Transfere Matrix Method
TNDT	Thermal Non Destructive Testing
TPT	Thermal Pulse Tomography
TWT	Thermal Wave Tomography

UD	Unidirectional
UT	Ultrasonic Testing
VI	Visual inspection
WMS	Wave Mode Spectroscopy

Nomenclature

Symbol	Description	SI Units
λ	Wavelength	m
λ_L	Lamè constant	Pa
μ_L	Lamè	Pa
ν	Poisson's ratio	$-$
ω	Angular frequency	$rad \cdot s^{-1}$
ω_0	Resonant frequency	$rad \cdot s^{-1}$
ρ	Density	$kg \cdot m^{-3}$
σ	Standard deviation	$-$
θ	Angle	$-$
$\tilde{\nu}$	Linear wavenumber	m^{-1}
c	Filter number	$-$
c_g	Group velocity	$m \cdot s^{-1}$
c_l	Longitudinal speed of sound	$m \cdot s^{-1}$
c_p	Phase velocity	$m \cdot s^{-1}$
c_t	Transverse speed of sound	$m \cdot s^{-1}$
d	Plate thickness	m
d_{ij}	Strain constant	V^{-1}
E	Young's modulus	Pa
e_{ij}	Strain constant	C^{-1}
f	Linear frequency	Hz
h	Half plate thickness	m
i	Complex number	$\sqrt{-1}$
K	Gaussian curvature	m^{-2}
k	Angular wavenumber	$rad \cdot m^{-1}$
k_x	Angular wavenumber in x axis	$rad \cdot m^{-1}$

k_y	Angular wavenumber in y axis	$rad \cdot m^{-1}$
L	Crystal length	m
N	Total number of samples	$-$
n	Sample	$-$
r	Radius	m
t	Time	s
u	Velocity	$m \cdot s^{-1}$
V	Speed of sound in material	$m \cdot s^{-1}$
X	Spatial axis	m
x	Spatial axis	m
Y	Spatial axis	m
y	Spatial axis	m
Z	Acoustic impedance	$Pa \cdot s \cdot m^{-3}$
z	Spatial through thickness axis	m

1. Introduction

1.1 Introduction

In an age where we so heavily rely on our infrastructure, there is an ever present need to determine their health. In order for us to interact effectively with the world around us in a sustainable manner a deep understanding of the structures we place in it is needed. By monitoring the health and condition of these structures we can better utilise them whilst still ensuring safety. Structural Health Monitoring (SHM) is the development of a strategy that is used to detect damage in a structure [1]. Through a combination of sensing technologies that are implemented on the structure, commonly using sensors such as fibre optic, acoustic or strain gauges, measurements are made at regular intervals in time [2]. This information is then used to inform the SHM system which is then able to detect the presence of damage. In industries from aerospace, to civil structures, such as dams, to green power, such as wind, SHM will help increase efficiency, safety and life span as well as minimising down time. As infrastructure is ageing and many structures, such as bridges, are being operated well past their initial designed lifespan, SHM seeks to allow these structures to remain in service with the knowledge that damage will be detected as they degrade. Furthermore SHM brings with it the promise of being able to reduce the weight of some safety critical structures as the ability to detect damage allows designers to reduce safety factors [2]. In the aerospace industry for example this could lead to major weight savings, helping to drive a reduction in fuel use. When implementing the same concept as SHM on rotating or reciprocating machinery it is considered Condition Monitoring (CM) [1]. This can encompass everything from the generators of wind turbines to lathes.

While SHM aims to detect damage in a timely manner and at a low cost, damage still needs to be characterised and assessed in a more detailed manner. It is this information that is especially important when making decisions on the condition of safety critical structures.

This is where Non-Distructive Testing (NDT) techniques are advantageous. NDT is a class of techniques that seeks to characterise the material properties, therefore detecting discontinuities or damage such as cracks [3]. These techniques are per-

formed without damaging the part being examined. NDT techniques may be applied at various points in the life of a part. Tests can be performed during manufacture, as well as during the service life of the part. In some cases NDT can even be performed in-situ, blurring the lines between NDT and SHM [2]. This work is focused on methods that fall under the remit of NDT.

During the manufacturing stage NDT techniques can show defects as well as deviations from the planned design. These can be present in all forms of manufacturing processes but can be particularly challenging to identify in processes such as additive manufacturing or the manufacture of composite structures [4].

The ability to identify and quantify damage in all manufactured parts allows for better informed decisions to be made about their ability to be put into service or remain in service. Furthermore, issues with the manufacturing process can be identified at an earlier stage with the help of good NDT. This allows waste to be reduced as high value parts may be repaired if defects are identified with sufficient accuracy. If these NDT techniques are sufficiently fast, accurate and cost-effective to deploy they can also allow for higher quantity of parts to be tested giving greater certainty of their quality. This again can allow designs to use smaller safety factors, thereby creating lighter and more efficient structures.

When parts are in service NDT techniques give vital information as part of the ongoing inspections. Some NDT techniques can be applied in-situ. This can allow detailed damage characterisation to complement SHM. Structures such as offshore wind turbines, for example, are challenging to inspect, repair and access. The challenging environment and costly access of offshore wind turbines further drives up the cost of inspection giving incentive to develop fast and simple-to-deploy NDT techniques. The ability to detect damage or degradation in structures such as these facilitates early repair, reducing further damage and unplanned downtime. By deploying NDT that offers greater precision the possibility to reduce inspection intervals is also introduced.

While a broad range of NDT techniques are available and well established, from Computerised Tomogrpahy (CT) to visual inspection, these techniques have a number of limitations. From cost, to the time taken for an inspection, to accuracy, the benefits and challenges faced by each technique are numerous and there is a great need for an NDT system that can improve on these limitations.

1.2 Aims and Objectives

Wavenumber based NDT techniques have been proposed to address many of the challenges faced by existing NDT techniques, offering the prospect of a fast, quantitative, fully non-contact and highly automated NDT system. A number of different

wavenumber based NDT techniques have been proposed. [5, 6, 7, 8]. Spatially local changes in wavelength signify changes in thickness for a given material and frequency. As such these changes in wavelength can be used to identify damage that changes the effective thickness, such as delamination or corrosion defects. With the use of a Laser Doppler Vibrometer (LDV) or air coupled ultrasound wavefield data can be gathered with a high spatial sampling density over a surface giving a map of damage. This presents a new class of NDT techniques that has been under investigation for the last decade [9, 10, 11, 12].

While these techniques have gained interest their inability to quickly measure structures as well as their limited effectiveness in terms of spatial and depth resolution have remained limiting factors.

This work aims to develop and demonstrate a novel wavenumber based NDT technique. Unlike previous work it will use full multi-frequency data and aim to determine changes in thickness within a structure not simply based on the change in wavelength but changes in in the characteristics of a particular Lamb wave mode.

Key areas of investigation:

- Use of theoretical dispersion relations to establish thickness maps from multi-frequency data using mode filtering.
- Investigate the ability of this approach to be furthered and optimised for non-isotropic materials where dispersion characteristics can not be easily obtained or are unknown.
- Investigate geometric transforms in order to allow wavelength to be determined on curved structures with the use of a Scanning Laser Doppler Vibrometer (SLDV).

1.3 Novelty statement

- Development of a frequency-domain mode based Lamb wave filtering technique, Wave Mode Spectroscopy (WMS) for isotropic materials.
- Investigation on effect of filter shape and bandwidth.
- Demonstration of technique on plate structures, quantifying ability and accuracy for damage detection.
- Expansion of WMS for application on non-isotropic composite samples with no prior knowledge of material, dispersion characteristics or nature of anisotropy.

- Developed and demonstrated WMS setup on complex geometries using no prior knowledge of the part or its location relative to the measurement setup.

1.4 Published work

F. A. F. Purcell et al. "Non-destructive evaluation of isotropic plate structures by means of mode filtering in the frequency-wavenumber domain". In: *Mechanical Systems and Signal Processing* 142 (2020), p. 106801. ISSN: 0888-3270. DOI: 10.1016/j.ymssp.2020.106801. URL: https://doi.org/10.1016/j.ymssp.2020.106801.

F. A. F. Purcell et al. "Lamb wave mode spectroscopy on complex structures with amplitude based feature detection". In: *Submitting pending patent application completion* (2020).

F. A. F. Purcell et al. "Non-destructive evaluation of non-isotropic composite structures by means of frequency-wavenumber domain filtering with no prior knowledge of material". In: *Submitting pending patent application completion* November (2019).

1.5 Covid-19 statement

The covid-19 pandemic begun during the completion of this piece of work. During the last 12 months of work no lab access was permitted for extended periods of time. Once lab access was regained it came with time limitations as well as limited access to technicians. This meant that not all planned experiments could be completed. Plans to manufacture further test specimens were also not able to be realised.

2. Literature review

2.1 Ultrasonic waves

Since the development of the first ultrasonic transducer in 1915 [13] in an attempt to detects object on the ocean floor, ultrasound has been used in a broad range of applications ranging all the way from simple rangefinders to 3D medical imaging. Ultrasound is generally defined as a sound wave above the range of human hearing [13]. This is mostly taken to be over 20kHz. Whilst ultrasound can exist in a liquid, gaseous or solid medium this work will only deal with solid media.

In solid media it is possible to broadly class ultrasonic waves as either being a bulk wave or a guided wave. A bulk wave travels, as its name suggests, through the bulk of a material [14]. The two types of bulk waves are longitudinal waves and transverse (or shear) waves as shown in Figure 2.1 [14].

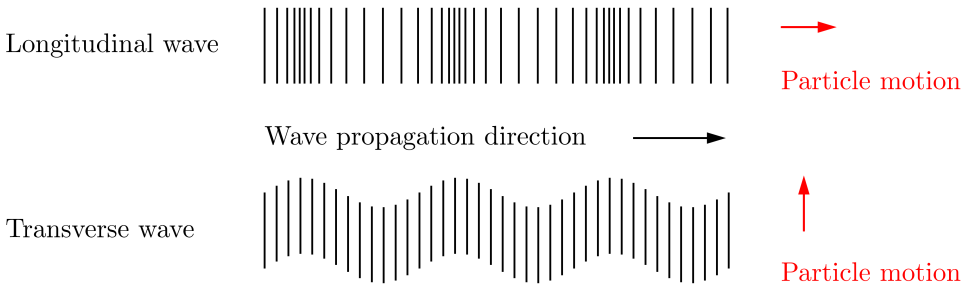

Figure 2.1: Longitude and transverse wave motion.

It is possible to determine the longitudinal, c_l, and transverse, c_t speed of sound in a given material from some physical parameters. The Lamè constants, λ_L and μ_L, are given in Equation (2.1) and (2.2) [15].

$$\lambda_L = \frac{\nu E}{(1+\nu)(1-2\nu)} \tag{2.1}$$

$$\mu_L = \frac{E}{2(1-2\nu)} \tag{2.2}$$

The Young's modulus is given by E and the ν gives the Poisson's ratio. Using the Helmholz theorem and the Lamè constants it is possible to show that the values of c_t and c_l can be given by Equations (2.3) and (2.4), where material density is given by ρ [15].

$$c_t = \sqrt{\frac{\nu}{\rho}} \tag{2.3}$$

$$c_l = \sqrt{\frac{\lambda + 2\nu}{\rho}} \tag{2.4}$$

While these waves interact with material boundaries, reflect and scatter, they are very different in nature to guided waves despite being governed by the same equations of motion [14].

Guided waves are ultrasonic waves that are bound and "guided" by the boundary of a material, so occur in plate-like or shell-like structures. Some common types of guided waves are Lamb, Rayleigh, Shear Horizontal (SH) Love waves and Stonley waves [14]. Schematics of three wave types are shown in Figure 2.2.

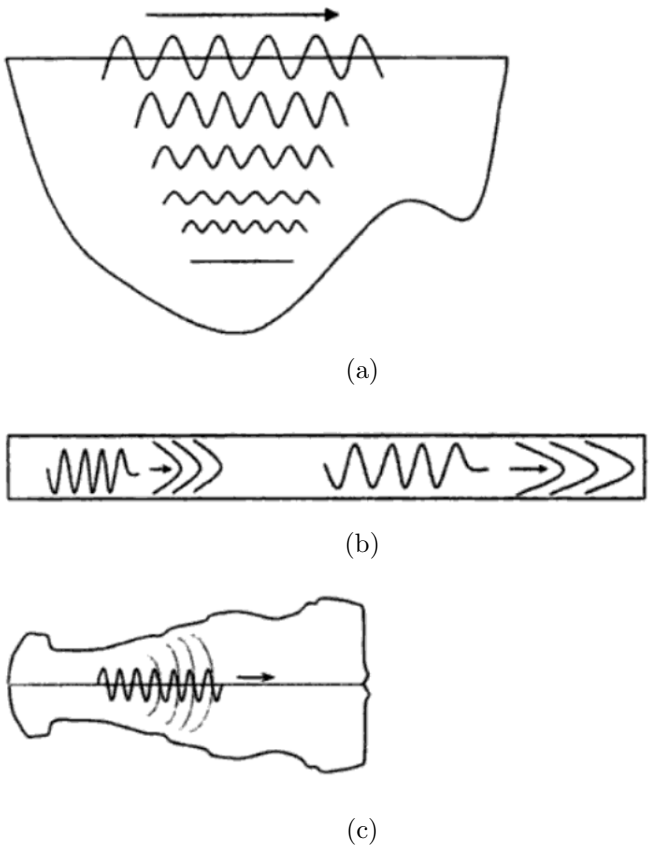

(a)

(b)

(c)

Figure 2.2: (a) Rayleigh, (b) Lamb and (c) Stonely wave [14].

Rayleigh waves occur on the surface of the material as shown in Figure 2.2 [16].

There are also other surface waves such as Love waves [16]. While the particle motion of a Rayleigh wave is elliptical; that of a Love wave is in-plane with the direction of propagation [14]. The particular motion of SH waves is perpendicular to the direction of propagation and in-plane with the bounding surface of the material [14]. Lamb waves are also present in free plate structures and their particle motion is perpendicular to the bounding surface [14]. For these wave types to be exploited for NDT they will need to interact with damage to detect it. As Rayleigh and Love waves decay with depth they are of less practical use for most NDT application. The same is true for Stonely waves which occur at the boundary between two solids. While these wave types may be used in certain applications the prevalence of plate-like components in structures such as aircraft make Lamb waves a prime candidate for NDT applications. While other wave types might not be desirable for certain NDT applications it is important to understand their nature as they may unintentionally be generated depending on the wave excitation method. They may also arise from mode conversion that may occur as a particular wave interacts with a defect or feature [16]. A useful analogy for a Lamb wave may be to think of it as similar to light running down a fibre optic. Much like the light being reflected off the edge of the fibre due to the change in optical impedance, Lamb waves are reflected within plate-like structures at the edge where a change in acoustic impedance is experienced.

2.2 Lamb waves

Lamb waves exist in a theoretically infinite number of modes [16]. These can be grouped into two classes, symmetric and antisymmetric modes. As shown in Figure 2.3 the symmetry is referenced about the center of the material thickness.

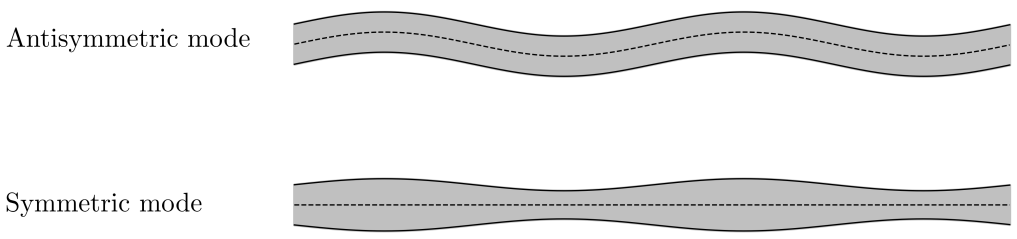

Figure 2.3: Antisymmetric and Symmetric Lamb wave modes.

2.2.1 Lamb waves in isotropic material

Lamb waves can exist in isotropic materials as well as non-isotropic multi-layered materials common in engineering applications such as composites.

The motion vector at a point **u** can be described in terms of a scalar, ϕ, and a vector, ψ, as shown by Equation (2.5) [15]. Here a scalar describes the magnitude with in the vector space and a vector is the combination of magnitude and direction [15]. It should be noted that ϕ is irrotational and $\boldsymbol{\psi}$ is divergence-free and that ∇ is the vectors differential operator. A irrotational vector has a curl of zero, that is to say the vector *phi* does not rotate [15]. The lack of divergence of the vector field in this application can be thought of as a lack of loss of energy.

$$\boldsymbol{u} = \nabla\phi + \nabla \times \boldsymbol{\psi} \tag{2.5}$$

Equations (2.6) and (2.7) is then given by substituting in Equations (2.3) and (2.4) and must be true to satisfy the elastic theory wave equation [17].

$$\nabla^2\phi + c_l^2\phi = 0 \tag{2.6}$$

$$\nabla^2\boldsymbol{\psi} + c_t^2\boldsymbol{\psi} = 0 \tag{2.7}$$

Equations (2.6) and (2.7) can then be solved for thin plate structures to give Equations (2.8) and (2.9), given the constant vectors $\boldsymbol{A_1}$, $\boldsymbol{A_2}$, $\boldsymbol{B_1}$ and $\boldsymbol{B_2}$ [15].

$$\phi = (\boldsymbol{A_1}cosh(pz) + \boldsymbol{A_2}sinh(pz))e^{(ikx-i\omega t)} \tag{2.8}$$

$$\boldsymbol{\psi} = (\boldsymbol{B_1}cosh(qz) + \boldsymbol{B_2}sinh(qz))e^{(ikx-i\omega t)} \tag{2.9}$$

The x and z axes refer to the direction of propagation and through thickness axes respectively. These are shown in Figure 2.4.

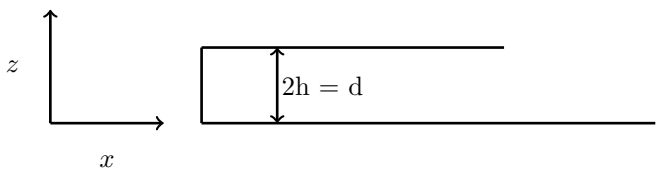

Figure 2.4: Cross section of semi-infinite plate of thickness 2h.

Equations (2.10) and (2.11) give the values for p and q.

$$p^2 = \frac{\omega^2}{c_l^2} - k^2 \tag{2.10}$$

$$q^2 = \frac{\omega^2}{c_t^2} - k^2 \tag{2.11}$$

Wavenumber is the representation of spatial frequency. k denotes the angular spatial frequency, given in $2\pi/\lambda$, where λ is the wavelength. The linear wavenumber, $\tilde{\nu}$ on the other hand is given in $1/\lambda$. Depending on the context both linear and angular wavenumber are used in this work. Likewise ω denotes the angular temporal frequency in $2\pi/s$ and f denotes the linear temporal frequency, given in $1/s$. If we consider a matrix with two spatial and one temporal axis, $u(x, y, t)$, and convert this into the frequency domain, it could be denoted using angular frequencies as $U(k_x, k_y, \omega)$, or linear frequencies, $U(\tilde{\nu}_x, \tilde{\nu}_y, f)$. The modes are commonly notated as S for symmetric and A for anti-symmetrical subscripted by their mode number [14]. Using this notation the fundamental symmetrical mode is denoted as S_0 and the fundamental antisymmetrical is denoted as A_0.

p and q are then substitute into Equations (2.8) and 2.9 and then substituted into the elastic relations given in Equations 2.12 and 2.12.

$$\sigma_{xz} = \mu \left(2\frac{\delta^2 \phi}{\delta x \delta z} - \frac{\delta^2 \boldsymbol{\psi}}{\delta x^2} + \frac{\delta^2 \boldsymbol{\psi}}{\delta z^2} \right) \tag{2.12}$$

$$\sigma_{zz} = \gamma \left(\frac{\delta^2 \phi}{\delta x^2} + \frac{\delta^2 \phi}{\delta z^2} \right) + \left(\frac{\delta^2 \phi}{\delta z^2} - \frac{\delta^2 \boldsymbol{\psi}}{\delta x \delta y} \right) \tag{2.13}$$

Here γ and ν are Lamè constants. Taking $\sigma_{xz} = \sigma_{zz} = 0$ at $z = 0$ or $z = 2h$ as the traction free boundry conditions the Rayleigh-Lamb equations can be found [15]. Rayleigh-Lamb equations for symmetrical and antisymmetrical modes are then given by Equation 2.14 and (2.15) respectively.

h denotes the half thickness of a plate of thickness d as shown in Figure 2.4.

$$\frac{tanh(qh)}{tanh(ph)} = \frac{4k^2 pq}{(q^2 + k^2)^2} \tag{2.14}$$

$$\frac{tanh(qh)}{tanh(ph)} = \frac{(q^2 + k^2)^2}{4k^2 pq} \tag{2.15}$$

These characteristic equations have an infinite number of solutions for a complex wavenumber, k, where $k = k + i * k$. The imaginary number, i, represents the value $\sqrt{(}-1)$. There is a physical interpretation for non-zero complex wavenumber components. If $k_{im} > 0$ the wave decays exponentially with distance so is of no concern for this application as it will not propagate [14]. If $k_{im} < 0$ on the other hand suggests that the wave grows exponentially with distance. These waves are

not known to exist [14]. As such only the real component, k_{real}, is taken.

The wavenumber can be related to the phase velocity through Equation (2.16).

$$c_p = \frac{\omega}{k} \tag{2.16}$$

The phase velocity, c_p, describes the velocity of a peak, or phase of a wave. The group velocity, c_g, on the other hand describes the velocity of a wave group as shown in Figure 2.5. The group velocity is given by the change in frequency to wavenumber ratio as shown in Equation (2.17) [15].

$$c_g = \frac{d\omega}{dk} \tag{2.17}$$

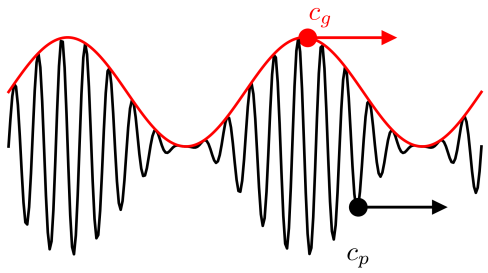

Figure 2.5: Phase velocity, c_p, and group velocity, c_g, of a wave.

The Rayleigh-Lamb equations are not exactly solvable so must be solved using an approximation methods such as bisection or the Monte Carlo method [14]. In this work the bisection method was chosen. The Rayleigh-Lamb equations were solved over a range of wavenumber values for a given frequency thickness value. A sign change in these solutions was then used to indicate the presence of a zero cross, indicating a solution. Near the zero cross this process can then be repeated with smaller steps in the wavenumber values to give more precise results. The Monte Carlo method randomly selects wavenumber and frequency thickness values and determines the solution. If this solution is sufficiently close to zero it is taken to be a root.

A key characteristic of Lamb waves is their dispersive nature. A dispersive wave will have a velocity that is dependant on the frequency [14]. That means for a given material and material thickness the wave velocity will be different at different frequencies. Using the Rayleigh-Lamb equations dispersion relations can be found in terms of the phase velocity, c_p, and a frequency thickness, fd. Figure 2.6 show the solutions for a 3mm thick aluminium plate.

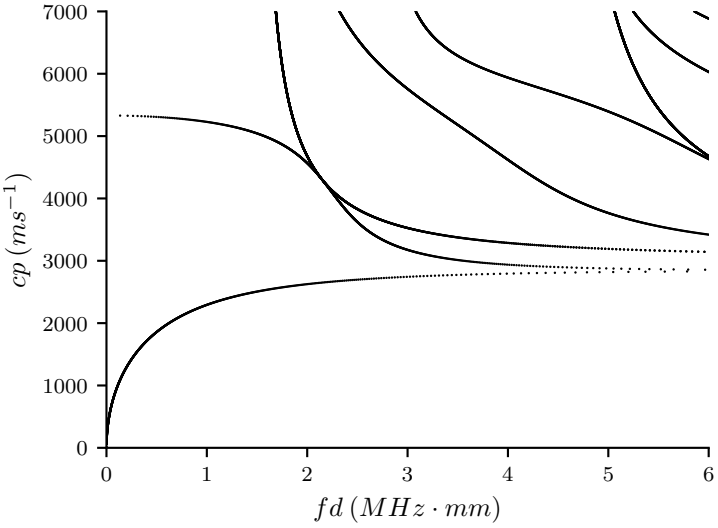

Figure 2.6: Lamb wave dispersion curves giving phase velocity.

The Rayleigh-Lamb equations dispersion relations can also be found in terms of the wavenumber, k, and a frequency thickness, fd. Figure 2.7 shows these solutions, also for a 3mm thick aluminium plate.

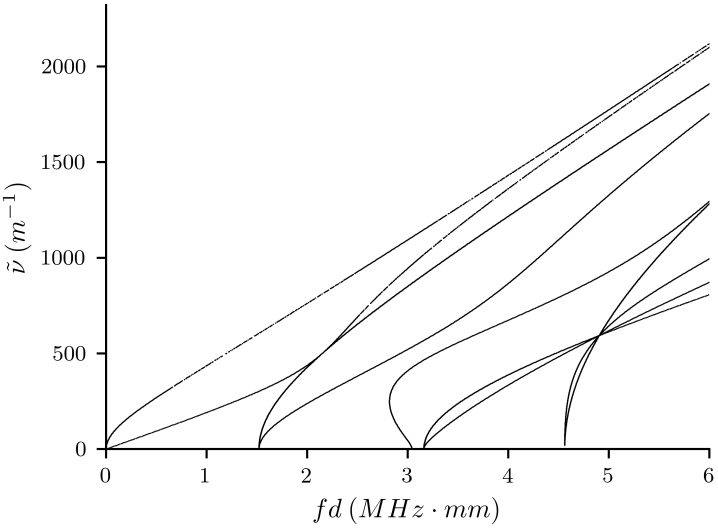

Figure 2.7: Solutions for Rayleigh-Lamb equation for aluminium.

2.2.2 Lamb waves in non-isotropic material

While the behaviour of Lamb waves in isotropic plates has been well described, their behaviour in anisotropic materials such as composites is markedly more complex. That is however not to say dispersion relations can not be determined theoretically. As theoretical calculation of composite dispersion curves are not a key part of this work a few key techniques are only briefly discussed to gain an understanding of their capabilities and limitations as covered by Kamal et al. [18].

Two key analytical methods are the Transfere Matrix Method (TMM) and Global

Matrix Method (GMM) as used in the DISPERSE software [19]. The TMM is advantageous as it can reduce the number of equations required and offers one of the computationally lightest methods of calculating dispersion curves [20]. A key drawback is its lack of stability at higher frequency thickness products [21]. The GMM on the other hand does not suffer these instabilities making it suitable even for large frequency thickness products [15]. By combining the stress at the boundaries of each layer into one matrix dispersion is calculated. While this still keeps the calculation to a single matrix it does result in a large matrix when considering composites with a large number of layers [20]. These analytical methods can be powerful tools but often do not offer an exact match with experimental data [21, 22]. While there are certain limitations to the analytical methods this error is often due to the fact that there are many challenges faced when trying to produce highly consistent and regular composites. As such determining the elastic properties of any given material is of key importance to being able to theoretically determine dispersion relations [22].

While Finite Element Analysis (FEA) does also offer the ability to solve these problems it is computationally extremely resource intensive, preventing it from being a viable option for most applications [18]. FEA does however offer the ability to model thick and complex materials with much greater ease. By using methods such as Semi Analytical Finite Element (SAFE) time can be reduced by applying a FEA approach through the thickness of the material and an analytic approach along the plane of propagation. This allows computational time to be vastly reduced while retaining the benefits of an FEA approach [22]. Local Interaction Simulation Approach (LISA) is another simulation approach that uses elastodynamic equations to describe the behaviour of a local region [23]. Due to the local nature of the method discontinuities and defects are much more easily modeled [22].

While there are different methods to determine dispersion relations a key feature of Lamb waves in composite materials is their tendency to travel faster along the fibre direction and slower across it [21]. So a material with all fibres aligned in a single direction will have very different wave velocities across and along the fibre [21]. Likewise a composite with random fibre placement or fibres oriented in a large number of directions will display similar wave velocity in all directions [21].

2.3 Lamb Wave sensing and generation

Characteristics such as their ability to propagate large distances in plate, shell or pipe like structure and their interaction with damage features makes Lamb waves ideal candidates for various SHM techniques [24]. A broad range of techniques have been proposed to detect damage using Lamb waves. These have been applied to

a variety of structures and damage types. Despite the great diversity, Lamb wave based SHM techniques can be categorised as either being passive or active techniques [25]. While passive techniques only detect ultrasonic signals from a structure to gain information about its health, active techniques both generate and detect an ultrasonic signal. Passive methods only require signal sensing, whereas active methods require both signal sensing and generation.

2.3.1 Piezoelectric materials

The most common and established way to both generate and receive Lamb waves, or any form of ultrasound, is through the use of a piezoelectric material. A piezoelectric material is any material that converts mechanical energy to an electronic potential and vice versa [14]. This property is present mostly in crystal structures with the most widely used being Lead Zirconate Titrate (PZT). While it can occur naturally in materials most undergo a process of polling whereby the material is heated and then cooled with a strong electric field across it [26]. This aligns dipoles in the crystal [26]. As the crystal is then mechanically deformed a charge is formed as the charged titanates move, breaking the symmetry and causing an imbalance in charge. Likewise by placing an electric charge over the PZT crystal the dipoles in the molecules will move causing mechanical displacement.

There are a number of different ways PZT crystals can be polled and cut. This results in different types of displacement when a voltage is applied over the crystal. The novel polled crystals has been proposed in the context of NDT to isolate specific wave modes or direction [27].

PZT crystals can also be used in composite form. This allows piezoelectric properties and shape to be further tailored [26]. PZT crystal have slots sawn in them that are then filled with a polymer [26]. By varying the cut size and number of axes in which the crystal is cut the crystal can be shaped and the acoustic impedance of the composite can be changed [26]. Acoustic impedance of a transducer is of key importance as a lower difference in acoustic impedance between the transducer and the material into which energy is being driven will maximise energy transfer. It is also possible to build flexible PZT transducers using this method by incorporating a flexible polymer[28].

Polymer based piezoelectric materials are commonly also favoured for their ability to be flexible [26]. One such material is polyvinylidine fluoride (PVDF). The film is commonly polarized through either stretching, being placed in a large electric field or through curing the film under high pressure [29]. The surface of the film then has an electrode deposited on it [30]. Benefits include flexibility, low cost and a low acoustic impedance that is similar to that of water, making it of particular interest for medical applications [26].

2.3.2 Piezoelectric Ultrasonic transducers

The piezoelectric element, such as PZT, forms part of a packaged transducer. The active elements are combined with other components to achieve better sensing and pulsing characteristics as well as making a transducer practical for real world application where it may be exposed to harsh environments [31]. Figure 2.8 shows a common structure of a single element transducer [31].

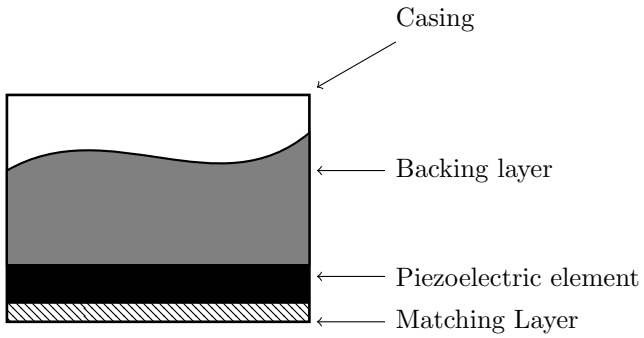

Figure 2.8: Single element transducer schematic.

The transducer is built around the piezoelectric element. This may be any piezoelectric material such as PZT or PVDF. The active element is backed by a damping material or backing layer. This layer is made to be thick and helps prevent ringing in the active element. Ringing refers to the continuous displacement of the element after an impulse excitation. When using Acoustic Emission (AE) system to locate damage, backing is of great importance as it shortens the impulse of the transducer response [31] helping locate it in time. To ensure good energy transfer from the active piezoelectric element into the backing layer it should be made of a material with similar acoustic impedance and high attenuation [31]. Acoustic impedance can be thought of much like optical or electrical impedance. It can be defined by,$Z = \rho V$ [32] where V is the speed of sound in the material, ρ the density and Z the acoustic impedance.

To minimise reflections from, and maximise energy transfer into the sample a matching layer is also added. Reflections are reduced by choosing a material that "matches" the acoustic impedance of the piezoelectric element and the sample. This is half way between the acoustic impedance of the two elements [31]. The matching layer can also have its thickness optimised to increase transmission [33]. A commonly used value is one quarter of the wavelength of the central frequency. To couple the transducer to the sample, coupling fluids such as grease, water or gels are commonly used. In some applications where transducers are permanently attached with glue, this can also be used as part of the matching layer to improve energy transfer [33].

In transducer applications, where the active elements are usually thin in relation to their width and length, the longitudinal-thickness mode has a dominant effect on resonance [34]. For example considers a piezoelectric crystal polarized in its thickness, with a voltage placed across its two faces that vibrates in a direction orthogonal to the applied field, in the direction of its length. In this case the resonance frequency, ω_0 is dependant on the length, L, of the crystal, its density, ρ, and its Young's modulus, E [35]. Their relation is given by Equation (2.18).

$$L = \frac{\pi}{\omega_0}\sqrt{\frac{E}{\rho}} \tag{2.18}$$

The temperature dependence of these properties also means that a temperature rise of a crystal will reduce the resonance [35]. Temperature changes are not only dependant on the surroundings but increases in temperature can also be caused by particular vibration regimes of the crystal [35].

2.3.3 Air coupled ultrasound

Not all applications allow for direct contact to be made. As such there are a number of ways with which ultrasonic energy can be driven into a structure without making contact with it. One such method is air coupled ultrasound. It is based on a transducer similar in construction to those used in contact setups but the energy is passed through an air gap before being driven into the structure. The high acoustic impedance of air means high power ultrasound is required. This also means when using air coupled transducers stand-off distances can not be large and are typically on the scale of centimeters [36]. Some work has shown much larger stand-off distances on the scale of meters but this has only been shown in the region of tens of kHz [36]. At higher frequencies these large stand-off distances are not practical due to the high attenuation in air and higher attenuation present at higher frequencies [37]. Furthermore it can be challenging to move a transducer over a complex surface geometry and maintain good coupling by controlling distance and orientation to the part.

2.3.4 Laser ultrasound

While piezoelectric material based sensing offers many benefits there are key limitations. One of these is the fact that piezoelectric transducers will be resonant in their nature. While this is often not of concern, a resonant transducer will not be able to capture all frequencies equally meaning transducers may only be applicable to certain applications. A further limitation is temperature range in which materials such as PZT can operate. While high temperature transducers have been developed the

Curie temperature of a single PZT crystal is around $160°C$ [26] making work in hot locations challenging. Many of these limitations can be overcome by using a laser ultrasound for non-contact Lamb wave sensing and generation. Unlike piezoelectric based sensors, laser ultrasound is not based on one principle that can be used to both sense and generate waves.

2.3.5 Laser Doppler vibrometer

For sensing of Lamb waves a Laser Doppler Vibrometer (LDV) is used which works on the Doppler principle. Figure 2.9 shows a simple schematic of a LDV.

A laser beam is split with one half being sent to a test sample under investigation. The reflected laser light from the test sample is then recombined with a reference beam split from the original laser light. If the test sample is not in motion the reflected beam will have the same frequency as the reference beam. Likewise if the test sample is in motion there will be a difference in frequency which will lead to interference at the the detector [38]. To be able to determine the direction of motion an optical-moderator, known as a Bragg cell, is introduced to the reference beam. This causes a constant frequency offset in the reference beam [38], allowing a direction of motion to be determined.

The simplest form of a LDV is a 1D system which has a single laser able to measure a single point. Furthermore it is only able to detect motion in line with the laser beam. While it is possible to mount a LDV on a linear stage, movement can often be limited in both range and speed [38]. Scanning Laser Doppler Vibrometer (SLDV) is an extension of a LDV system that includes a galvanometer mirror system. The mirrors can be used to rapidly and accurately drive the laser to different points. This allows for fast data acquisition at high spatial resolution.

As with an LDV system an SLDV is only able to detect motion in line with the laser beam. This means when there is a large angle of incidence between the laser and the surface of the sample, less out-of-plane more in-plane motion is being measured. While not an issue for many applications, when it comes to Lamb waves this also means that the predominantly out-of-plane A_0 mode will appear less dominant and the predominantly in-plane S_0 mode will be more visible.

A further extension of this setup is a 3D SLDV. The system consists of three laser beams. By having three lasers at different spatial locations measuring the same point, the angle between the lasers can be used to determine the velocity at the measurement point in all three axes [38]. LDVs have long been used to detect guided Lamb waves [39, 40, 41]. It is possible to get full-field response data, analogous to a video of a Lamb wave passing through a structure.

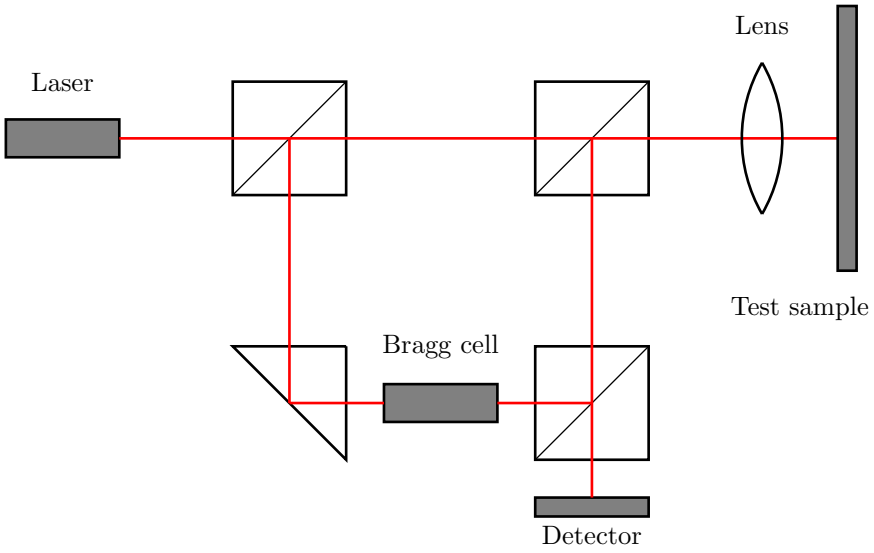

Figure 2.9: Schematic of LDV.

2.3.6 Laser Ultrasound generation

Guided Lamb waves can also be generated using the likes of a Q-switching laser [10, 12, 42]. There are two distinct regimes that are use to generate laser ultrasound. In thermoelastic regime guided waves are generated by the laser causing thermal expansion and constriction at its focal point on the structure [43]. The thermal changes cause a shock wave to be generated. The wave characteristic can be tuned by changing the wavelength, power and pulse length of the laser [42]. In the ablative regime a small amount of the surface is ablated by the laser, which in turn causes a shock wave [44]. The ablative regime is able generate higher energy waves than the thermoelastic regime but it has the significant disadvantage of damaging the samples surface. Using a laser pulse to generate Lamb waves holds a number of advantages over contact methods. As with air coupled ultrasound its non-contact nature offers advantages when access is limited. Unlike air coupled ultrasound greater stand-off distances can be achieved adding to the practicality of the method. Furthermore through the use of a mirror system the laser can quickly be driven to different points on a sample [12, 45]. The impulse excitation is also capable of generating a broad range of modes and frequencies in the structure [42]. Laser ultrasound can be used to either drive ultrasonic energy continually into a structure or produce a single, highly repeatable pulse [42, 45]. An inherent disadvantage of laser generated Lamb waves in the ablative regime is surface damage by the laser. This is particularly relevant when high energy excitation is required which can not be achieved in the thermoelastic regime [42]. Methods have been proposed to overcome surface damage problems such as indirect excitation through generating a laser plasma close to the

sample, causing a shock wave impulse [43]. Unlike the lasers used for sensing of Lamb waves those for generation are of much greater energy, meaning safety precautions must be taken when using laser pulsing ultrasound. These same risks are not faced when air-coupled or contact ultrasound methods are used.

2.4 Ultrasound NDT techniques

While ultrasonic based NDT is a very broad category that encompasses many varied methods it is useful to understand a number of methods that are able to generate similar results to the new techniques proposed in this work. Key considerations are similar spatial resolution and measurement speed or depth resolution. A further consideration is the ability of the technique to work on advanced composite materials.

2.4.1 Ultrasonic testing

A long standing contact NDT method is Ultrasonic Testing (UT). While techniques differ there are some commonalities. Broadly, data can be classed as either A-scan, B-scan or C-scan [46]. An A-scan is the simplest form, giving data with a time and amplitude axis. An ultrasonic pulse is emitted from the transducer and driven into the part. The back face of a part or any imperfections inside the part will then cause part of the ultrasonic pulse to be reflected back, exciting the piezoelectric element and producing an electric potential [46]. By knowing the speed of sound in the bulk of the material and the time between the pulse and the reflected wave the depth of any defect can be quantified. A simple schematic is shown in Figure 2.10.

A B-scan can be thought of as an A-scan repeated on multiple points along an axis [46]. This would give data analogous to a cross sectional cut. A C-scan furthers this by covering two axes giving data 2D image, allowing the identification, sizing, location and depth of defects to be determined [46].

These types of measurements may either be performed with transducers either side or on a single side of the sample. When on a single side a single transducer creates the pulse and then switches to sense the echo. This is known a pulse echo configuration. Two transducers can also be used with one driving and one receiving the echo on the same side in a pitch-catch configuration [47]. By placing a transducer on either side of the sample, through-transition setups can be used to determine the attenuation or scatter caused by defects in the sample [47].

Key advantages are the ease with which these techniques can be applied, for in situ testing as well as their high sensitivity [47]. Disadvantages include the need for skilled users, inabilities to easily locate the damage in reference to the global

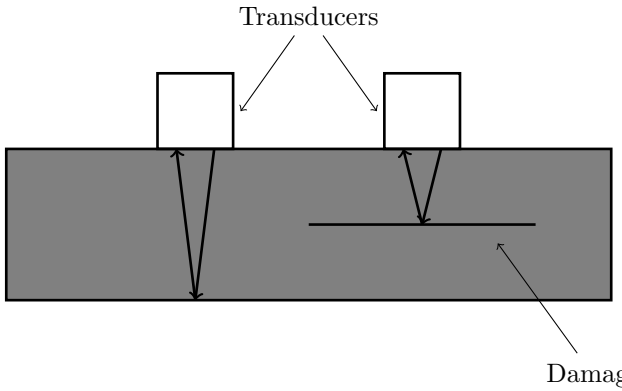

Figure 2.10: Schematic of UT in plate with and without damage.

structure and the requirement for contact and coupling in most applications [47].

2.4.2 Phased array

Phased array ultrasonic inspection offers further advancements, especially in terms of resolvable detail and sensitivity to small defects. By using an array of elements that generate an ultrasonic pulse with slight offsets in time it is possible to focus and steer the ultrasonic beam [48]. By varying the angle at which the ultrasonic beam intersects with a defect sensitivity can be vastly increased [45, 48]. Phased array ultrasound setups are common choices for in situ tests and can be effectively used to detect defects ranging from delamination in composites to weld cracking [45]. Further challenges are faced when it comes to complex materials such as Glass Laminate Aluminium Reinforced Epoxy (GLARE) where many internal boundaries are present even when damage is not present [49]. As with other ultrasonic methods the contact nature of phased array scanning means that automating the testing of large areas is challenging. Without automation it also is challenging to gain positional information of any identified defects.

2.5 Non-ultrasound NDT techniques

Ultrasound based NDT techniques are used in a broad range of industries. There are however a number of other techniques that can identify similar defects and should be considered as they are viable alternatives to the methods developed in this work. They also serve to demonstrate limitations to current NDT methods.

2.5.1 Visual inspection

Visual inspection (VI) is one of the longest standing NDT techniques and can be used to identify a broad range of defects from cracks to dent defects [45]. The nature of VI means its quality is highly dependant on the skill and experience of the individual carrying out the inspection. While they are able to move around many structures with ease the need to be close to the part means challenges are faced when inspection of hard to reach structures such as wind turbine blades or bridges is required [45]. The requirement for close proximity also limits this technique in hostile chemical or nuclear environments. While VI can identify surface damage it can not identify internal damage such as internal corrosion defects. This poses particular problems in composite structures where delamination defects are common but often not externally visible [45]. Visual inspection can however be very effective at detecting cracks in structures when using dye penetrates. Small cracks in structures can be challenging to detect using other methods such a guided ultrasound techniques.

2.5.2 X-ray NDT

While the category of X-ray NDT techniques is broad they hold a number of common features. The basis of the technique relies on an X-ray source emitting X-rays onto a specimen. A detector on the other side of the specimen can then detect the X-rays that pass through the part [45]. By analysing the transmitted radiation a detailed view of the part can be gained. Information down to the crystal structure of metals can be resolved [45]. By moving the source and emitter 3D information can also be acquired. This is usually done in the form of a CT scan where the structure and/or emitter are moved between measurements [50]. While X-ray NDT can give a highly in depth view of a part it comes with limitations. The cost of running equipment is high and highly trained users are required [50]. Parts also need to be accessible from both sides for X-ray inspection to be used. This meaning extensive disassembly is often required and even then it is not a suitable technique for many structures. The high levels of radiation involved further increase safety precautions required and make this method unsuitable for any form of in situ testing.

2.5.3 Thermal non-destructive testing

Thermal Non Destructive Testing (TNDT) includes a range of techniques such as Thermal Pulse Tomography (TPT) and Thermal Wave Tomography (TWT). These techniques have been proposed in a number of materials from metallic structures to composites [51]. Most TNDT operate on a principle of rapidly heating an area

of a sample, usually using a thermal source like Infrared (IR), and observing the temperature change during the heating or cooling process [51]. Areas of different thicknesses will cool or heat at different rates allowing defects such as delaminations, disbonds or corrosion defects to be detected. While this can be a fast and effective technique in many applications it is limited by the lack of an absolute measure in depth. Furthermore many components used in industries, such as the aerospace industry, are coated with thermally resistant coatings to protect them from harsh environments [51]. Methods have been proposed whereby cracks can be detected using thermal methods [52]. These methods usually rely on generating some level of thermal flux across the surface of the sample allowing the lower thermal conductivity of a crack to be shown.

2.5.4 Eddy Current testing

Eddy Current testing offers high resolution and detailed information about a part. By driving an alternating current through a conductor a magnetic field is created. the conductor is then placed close to the sample to be examined. This sample must also be electrically conductive. The magnetic field generates an eddy current in the sample [53]. That current will itself have a magnetic field which can be detected by a sensor close to the sample. Changes in properties of the material such as porosity, thickness change or cracks will all effect the eddy current and its magnetic field, allowing detection [53]. To ensure correct measurement, distances between the current coils and the part need to be accurately maintained. This creates challenges when examining geometrically complex structures. The largest limitation of this technique is however the fact that it relies on the sample being conductive, limiting it to materials such as aluminium or steel [53].

2.6 Wave analysis methods

Before further discussing Lamb wave and wavenumber based NDT techniques it is useful to consider some useful techniques used to analyse waves. An understanding of fundamental wave features such as frequency, phase and amplitude is vital to signal analysis. In this work frequency analysis is of particular importance.

2.6.1 Fast Fourier Transform (FFT)

Wave data is commonly recorded ether in relation to time or spatial position. These waves would be describes as being in ether the temporal or spatial domain.

The FFT a powerful analysis technique that allows data to transformed into the frequency domain. In this work data are gathered with relation to spatial position,

time or both. The Fourier transform allows for the transformation from any domain into the frequency domain. The equation for the Fourier transform is given in Equation 2.19 [54].

$$\hat{f}(\xi) = \int_{-\infty}^{\infty} f(x) e^{-2\pi i x \xi} dx \tag{2.19}$$

Here $\hat{f}$ denotes the transformation of the function f, and ξ denotes any real number. The operation on a function $f(x)$ is usually denoted by $\mathcal{F}$ as shown in equation 2.20.

$$\hat{f}(\xi) = F(f(x)) \tag{2.20}$$

We can briefly consider a 2D signal as shown in Figure 2.11. The signal shows a sine wave with a wavenumber of $40m^{-1}$ in the X direction and with no frequency component in the Y direction. This wavefield was then transformed into the frequency domain using a 2D FFT as shown in Figure 2.11 (b). As such the corresponding frequency representation of the 2D signals shows two spikes at the negative and positive wavenumber of $\tilde{\nu}_x = 40m^{-1}$. There is however no energy in the $\tilde{\nu}_y$ direction indicating no frequency present in that axis.

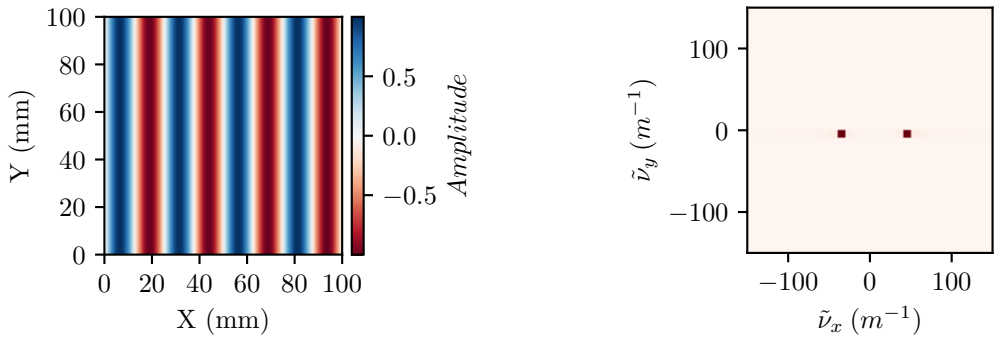

(a) (b)

Figure 2.11: A sine wave with a wavenumber of $40m^{-1}$ in the X direction, in (a) the time domain and (b) frequency domain.

If we now consider the wavefield with the same wavenumber in the X direction and a higher wavenumber of $80m^{-m}$ in the Y direction we get the wavefield shown in in Figure 2.12 (a). After applying a 2D FFT to that signal we get the frequency domain representation shown in 2.12 (a).

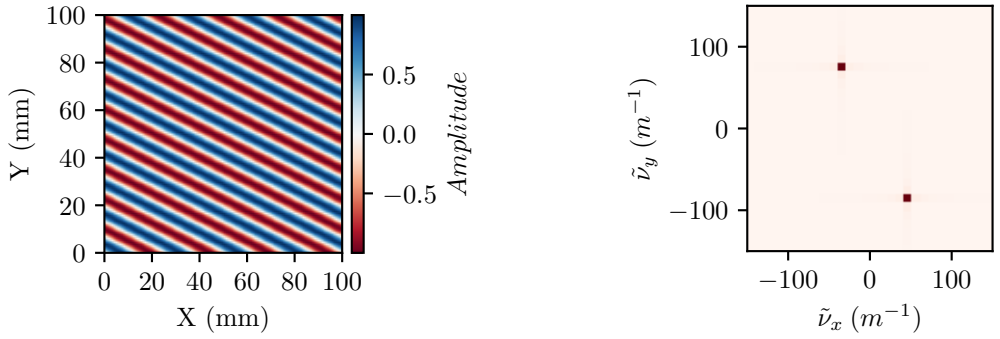

(a) (b)

Figure 2.12: A sine wave with a wavenumber of $40m^{-1}$ in the x direction and $80m^{-m}$ in the y direction, in (a) the time domain and (b) frequency domain.

Considering only the $\tilde{\nu}_y$ in the frequency domain in Figure 2.12 (b) we can observe that the two bright spots align with $\tilde{\nu}_y = 80m^{-1}$ and $\tilde{\nu}_y = -80m^{-1}$. If we now consider the same spots but in the $\tilde{\nu}_x$ axis we still obverse the frequencies of $\tilde{\nu}_y = 40m^{-1}$ and $\tilde{\nu}_y = -40m^{-1}$.

This same concept can be applied over any number of dimensions.

2.6.2 Hilbert transform

The Hilbert transform is another powerful tool for signal analysis that is able to given an analytical signal from which features such as phase and local amplitude can be determined. The Hilbert transform has a relationship with the Fourier transform, allowing for a useful definition of the Hilbert transform in the frequency domain. If we consider a real function, $f(t)$, who's frequency representation is $F(\omega)$, the frequency domain Hilbert transform of is given by $F_h(\omega)$ as shown in Equation 2.21 [55].

$$F_h(\omega) = \begin{cases} F(\omega), & \omega > 0 \\ -F(\omega), & \omega < 0 \\ F(0), & \omega = 0 \end{cases} \tag{2.21}$$

The frequency domain analytic signal, $F_a(\omega)$ is then given by adding the original signal to its Hilbert transform as shown in Equation 2.22

$$F_a(\omega) = F(\omega) + F_h(\omega) \tag{2.22}$$

To generate the Hilbert transform of a signal the sign of the negative frequencies is turned negative. As such we can also show the Hilbert transform with the help of a signum function, given in Equation 2.23 [55].

$$sgn(x) = \begin{cases} 1, & x > 0 \\ -1, & x < 0 \\ 0, & x = 0 \end{cases} \tag{2.23}$$

The signum function is shown graphically in Figure 2.13.

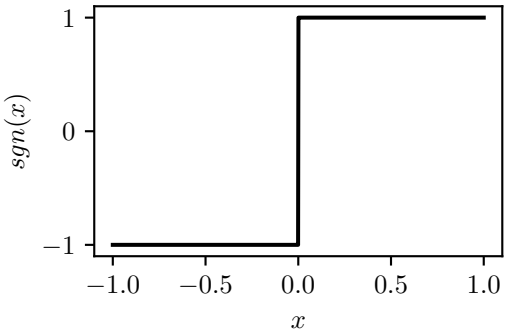

Figure 2.13: The signum function of x.

The analytic signal can then be found with Equation (2.24).

$$F_a(\omega) = (1 + sgn(\omega))F(\omega) \tag{2.24}$$

The local phase, $\phi(t)$, and amplitude, $A(t)$, of a signal $f(t)$ can determined using the Hilbert transform of that signal, $f_h(t)$ as shown in Equation 2.25 and 2.26 [55].

$$\phi(t) = arctan\left(\frac{f_h(t)}{f(t)}\right) \tag{2.25}$$

$$A(t) = \sqrt{f(t)^2 + f_h(t)^2} \tag{2.26}$$

2.6.3 Monogenic signal analysis

While the Hilbert transform is a powerful tool it is limited to 1D problems. The Riesz signal is a mutli-dimensional extension of the Hilbert tranform. Where the Hilbert transform is used to give an analytic signal, the Riesz transform uses the same concept to give a monogenic signal. Given a real 2D signal, $u(x, y)$, with the frequency domain representation of $U(k_x, k_y)$ the monogenic signal will have three components as shown in Equation (2.27), (2.28) and (2.29) [56] . These are analogous to the two components, $F_h(\mu$ and $F(\mu)$ of the Hilbert transform.

$$L_{ox}(k_x, k_y) = i\frac{k_x}{\sqrt{k_x^2 + k_y^2}}U(k_x, k_y) \tag{2.27}$$

$$L_{oy}(k_x, k_y) = i\frac{k_y}{\sqrt{k_x^2 + k_y^2}}U(k_x, k_y) \tag{2.28}$$

$$L(k_x, k_y) = U(k_x, k_y) \tag{2.29}$$

$L_{ox}(k_x, k_y)$ and $L_{oy}(k_x, k_y)$ are the two odd filters in the frequency domain and their imaginary components are shown in Figure 2.14 and Figure 2.15. Their lack of symmetry in the frequency domain means they are purely imaginary in the spatial domain [57].

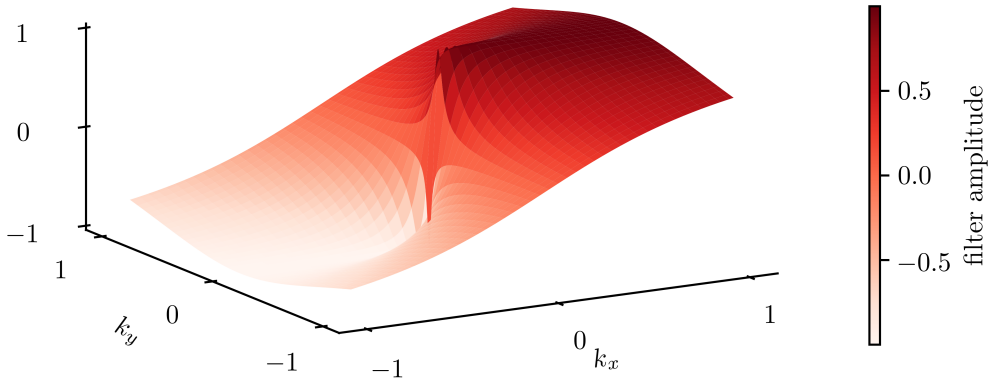

Figure 2.14: L_{ox} filter.

The amplitude of the 2D signal can then be found using Equation (2.30) where $l(x, y)$ is the Inverse Fast Fourier Transform (IFFT) of $L(k_x, k_y)$.

$$A(x, y) = \sqrt{l(k_x, k_y)^2 + l_{ox}(k_x, k_y)^2 + l_{oy}(k_x, k_y)^2} \tag{2.30}$$

It is worth noting the analytical signal for a 1D problem is found by multiplying the frequency domain representation, $F(\mu)$, of a real signal, $f(x)$ by a signum function, as given by Equation (2.23), where all negative frequency values undergo a sign change [57].

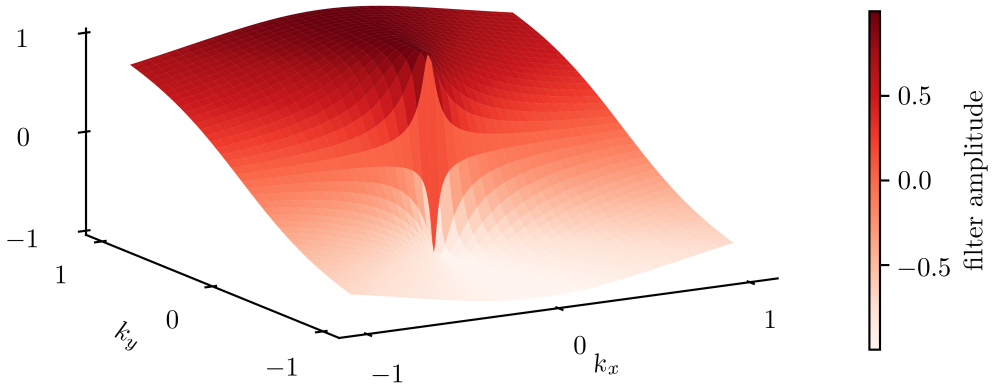

Figure 2.15: L_{oy} filter.

The same signum function can be seen along $k_y = 0$ and $k_x = 0$ axes in the 2D extension in Figure 2.14 and 2.15 respectively.

2.7 Full-field wavenumber NDT

As previously discussed Lamb waves are dispersive in their nature, meaning for a particular Lamb wave mode the material, material thickness, wavelength and temporal frequency are related [14]. This relationship is described by the dispersion curves as shown in Equation (2.7). As such if a single frequency Lamb wave is generated in a plate-like structure thickness changes can be identified by changes in wavelength. Using full-field data with a high spatial sampling frequency (about 2mm between measurement points) it is possible to get a detailed image of damage. A technique such as this may be able to give comparable results to a C-scan ultrasonic test. As such, a number of attempts have been made to identify changes in wavelength of guided Lamb waves. While this is theoretically possible with any Lamb wave mode the dominant out-of-plane motion of the A_0 make it preferable. The out-of-plane motion allows for easier detection of the wave using both PZT sensors, or other sensors such as an LDV. In material such as aluminium with thicknesses from $0mm$ to about $15mm$ the A_0 mode also shown greater dispersion, which means the wavelength will change more for a given thickness change than the S_0 mode. Other NDT techniques also use changes in wavelength to identify damage in combination with lower sensor density [6, 58, 59]. While these techniques are related they differ in their results and application and will not be covered in detail in this section.

2.7.1 Full-field data

Full-field data are commonly gathered using a single PZT transducer attached to the structure with a LDV on a mechanical stage or a SLDV to record the response at a grid of spatial sampling points [10, 60, 61, 62]. The reverse of this method is also possible whereby a fixed transducer is used to record the signal generated by a pulsing laser that is moved over a spatial grid [10]. There are two distinct excitation regimes: transient or steady-state. For a transient measurement the pulse signal is generated in the specimen, triggering a measurement at a sample point. The response at the point is recorded and the specimen is given time to ring down. To reduce noise this may be completed a number of times at the same spatial point. The measurement device is moved to the next spatial sample point and the process is repeated. This technique gives a clear image of a wave front moving through the structure. A snapshot in time of a transient wave is given in Figure 2.16. This method offers advantages such as high signal-to-noise-ratio

and the ability to detect damage based on wave reflection [60, 61, 63]. A major disadvantage however is the large time taken for a measurement as a ring down time is required after each excitation. Steady-state excitation on the other hand continually drives a waveform into the structure so that a 'steady-state' of excitation is reached. Measurements can then be taken at a spatial point at any time as long as they are phase synchronised with the excitation signal, therefore vastly reducing the time require to take a measurement [40, 64, 65]. A greater wave amplitude can also be generated improving the signal-to-noise-ratio meaning fewer averages need to be taken at each sample point, allowing a further reduction in measurement time.

Figure 2.16 (b) shows a snap shot in time of a steady-state response. Each result was normalised by its maximum value to show the wavefield clearly. It should however be noted the the maximum amplitude of the steady-state excitation was substantially greater than that of the transient excitation. This is due to the fact that larger amounts of energy can be driven into the structure when using steady-state excitation, improving signal-to-noise-ratio and propagation in materials with high attenuation such as composites [6]. There have been a number of methods proposed to utilise this data for damage detection. The commonality of all these methods is that they use changes in wavenumber to detect areas of damage.

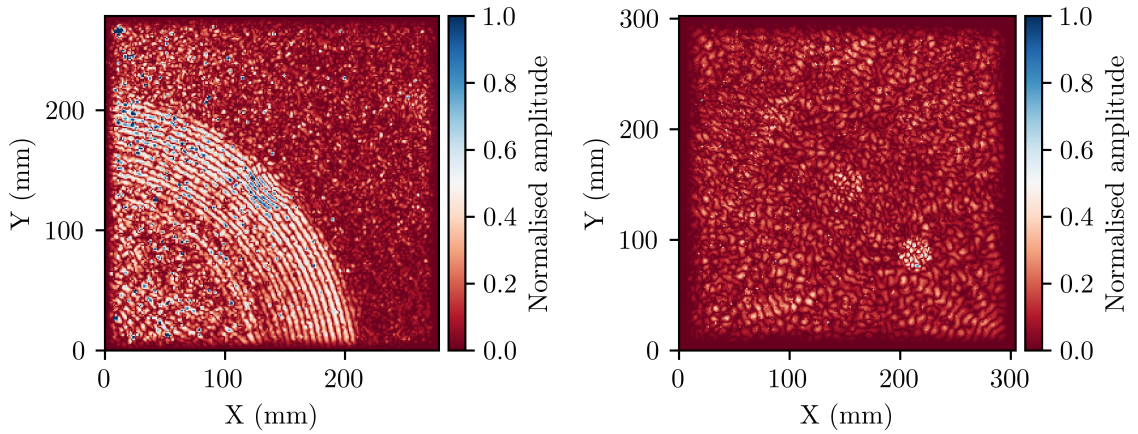

Figure 2.16: Snapshot in time of (a) transient and (b) steady-state response.

2.7.2 Local wavenumber

Imaging through direct wavelength measurement was first proposed by Flynn et al. [10]. This technique incorporated a broad band mode filter to remove the S_0 mode. Once the data had been filtered to a single mode in the frequency-wavenumber domain it was converted to the spatial frequency domain. A single frequency slice was selected giving a 2D velocity matrix with two spatial axis, $u(x, y)$, at a given frequency. The analytic signal was then determined in the dominant direction of

propagation. As such this can be thought of as a series of 1D problems where the dominant frequency is to be determined along the length of a signal at each sampling point. This was achieved by removing a wavenumber component though a bandpass filter centred around a wavenumber, k_c, and then determining the amount of energy remaining after the filtering process by finding the envelope of the analytic signal [10]. This enabled the direct measurement of the wavelength but transducer location is vital for accurate results. That is to say with a circular wave-front, as the spatial location moves further out of line of the transducer the wavelength will be over estimated. This method will also suffer from distortions around discontinuities that cause scattering of Lamb waves. This technique was able to to give some clear image of defects but it was not able to determine characteristics such as depth of a delamination defect. Furthermore features such as sensitivity to the location of the excitation transducer left further challenges.

In the work of Rogge and Leckey [9] many of these limitations were overcome. Like the previous work, they used transient full-field data, $u(x, y, t)$, and filtered it to a single Lamb wave mode. Once filtered, it was broken up into spatially windowed sections that were converted into the frequency domain with a 3D Fourier transform $U_{mn}(k_x, k_y, \omega)$ [9]. From the spatially windowed data the dominant frequency slice was then taken and the dominant wavenumber found [9]. This process is somewhat analogous to a short-time Fourier transform extended to a two-dimensional problem. Window sizes ranging from 7mm to 11mm were used [9]. As with a short-time Fourier transform there is a direct trade-off between frequency and spatial resolution. With the frequency in this work referring to the spatial frequency, or wavenumber, this trade-off is between spatial resolution and depth resolution. At larger material thicknesses this problem would be further exacerbated as the wavenumber change reduces for a given thickness change at greater material thicknesses for a given frequency. In thicker components the wavelength will also be longer for a given frequency [14]. To resolve a wave the spatial window should be at least the size of two wavelengths according to work by Juarez et al. [66]. While not shown in this work it is suggested that it is possible to create a thickness map using the wavenumber and dispersion characteristics. It is however also recognised that the anisotropy of the material is not taken into account.

Attempts to reduce the trade-off by spatial windowing were first made by Mesnil et al. [62]. A technique referred to as Instantaneous Wavenumber (IW) was proposed. The IW was calculated by taking the spatial derivative of the phase obtained from the Hilbert transform [62]. The spatial and temporal measurement data, $u(x, y, t)$, was turned into the spatial-frequency domain, $u(x, y, \omega)$. From there the response at a dominant single frequency was found, $u_\omega(x, y)$. As wavelength is frequency dependant having a single frequency allowed for correlation to thickness

at a later stage. The Hilbert transform is inherently a 1D algorithm so is extended by performing it in both the x and y axis. The wavelength is then determined by taking the magnitude of the x and y component [62]. While this can be effective on simple 2D wavefields this is not a true multi-dimensional extension of the Hilbert transform [56]. This technique was compared with the previously developed local wavenumber approach that spatially windowed the wavefield and found the dominant wavenumber at the dominant frequency slice [9]. A spatial windowed approach was shown to give much better results compared to the IW [62]. The local wavenumber approach was extended to thickness correlation [62]. Dispersion characteristics of the material were determined through SAFE. The wavenumber map was then be used to create an effective thickness map [62]. Mesnil et al. furthered their IW technique in later work [67] but were unable to overcome many limitations so did not provide significantly improved results.

While this showed some good results for the local wavenumber approach this technique still faces many limitations. The composite plate used was 1.6mm thick at 8 ply. At greater thicknesses depth resolution would be lost due to the large bin size in the wavenumber domain caused by the small number of samples in a spatial window. To improve this a larger spatial window would need to be taken, resulting in lower spatial resolution. Work by Fan et al. also used dispersion relations to related wavenumber maps back to material thickness on an aluminium panel [68]. The wavenumber maps in the work were also found through the local wavenumber approach inherently limiting both the depth and spatial resolution [68].

2.7.3 Wavenumber Spectroscopy

These inherent limitations of spatial windowing were first overcome successfully by Flynn et al. in their 2014 work [12]. All previous work also used transient excitation whereas Flynn moved to steady-state excitation which greatly reduced measurement time [12]. A single frequency sine waveform was continually driven in to the structures at either 100kHz or 200kHz. This allowed a spatial grid of sampling points to be measured without having to wait for the structure to ring down between measurements.

To further increase measurement speed Flynn et al. used a continuous measurement [12]. Unlike previous work where the LDV was driven to a spatial point to take a measurement in time, the laser was continually driven over the surface of the structure. The rate of motion was chosen so that an integer number of excitation cycles passed during the time it took to drive the laser between sampling points. Knowing the scan speed this data were then broken up into a time history map, $u(x, y, t)$. Using a broadband mode filter in the frequency domain a single wave mode was identified. As in all previous work the A_0 mode was chosen due to its

dominant out-of-plane nature as well as the fact that a thickness change will have a greater effect on the wavelength of the A_0 mode than the S_0 mode. A time domain Fourier transform was then used to identify the response map, $r(x, y)$, at the driving frequency [12]. The single mode response was passed through a bank of narrow band wavenumber filters in the wavenumber domain. A 2D envelope was then determined for the wavefield once it had been narrow band filtered. The central wavenumber of the filter that maximised the 2D envelope at a given point is then assigned to that point. This method was refined in a later paper [69] and given the name Acoustic Wavenumber Spectroscopy (AWS). Figure 2.17 shows a visual representation of the technique [69].

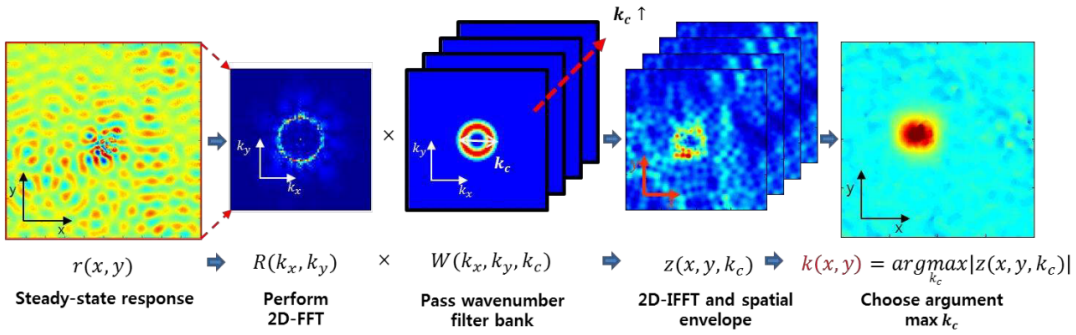

Figure 2.17: AWS process [69].

This technique can be compared with local wavenumber mapping as first proposed by Rogge et al. [9]. A schematic describing this method is given in Figure 2.18.

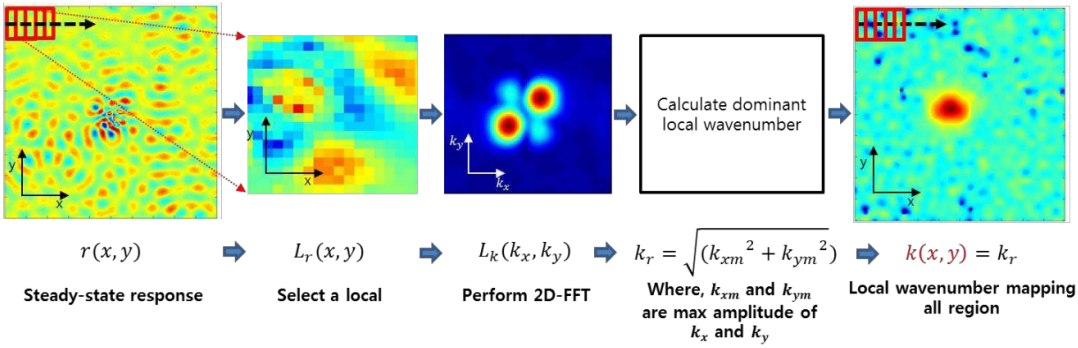

Figure 2.18: LWM process [69].

These techniques were both demonstrated on an aluminium plate with a corrosion defect, a pressure thinning on a steel pipe and a dis-bond stiffener on a composite panel. Results were able to give consistent wavenumber results for areas of similar thickness, thereby highlighting the damage [69].

2.7.4 Wavelet transform

The same limitations of wavenumber resolution when using spatial windowing were addressed using a wavelet transform [70, 71]. The wavefield data are processed using a 2D wavelet. This reduces the issues present when using spatial windowing as the wavelet is scaled and shifted allowing it to maintain frequency and spatial resolution [71]. The use of a 2D wavelet transform does however carry with it different limitations. A wavelet transform is able to identify instantaneous frequency, in this case the spatial frequency or wavenumber [72]. This is obviously beneficial when trying to identify changes in the wavelength. Wavelet transforms face limitations in terms of spatial resolution when large wavelengths are considered [72]. This would limit the use of wavelet transform based techniques when applied to thick materials, or materials with high phase velocity's. On the other hand wavenumber spectroscopy is not effected in the same way allowing for better damage detection, especially when considering thicker materials where the Lamb wave wavelengths will be larger.

2.7.5 3D structures

The works referenced so far have all made use of LDVs or SLDVs. As discussed this technique gives only out-of-plane velocity data. The measurement of complex shapes is not easily achieved without complex automation to manipulate the position of parts when using LDVs. All the previous work has also been limited to flat plate-like structures with the exception of some measurements carried out on pipes, these include Flynn et al. [10], Kang et al. [69] and Truong et al. [73]. These were measured using a SLDV and while they can measure velocity at incidence angles as high as 45°, signal-to-noise-ratio decreases and in-plane velocity is included in the data, making the need for mode filtering even greater [40]. Koskelo and Flynn further investigate the ability of AWS to be used on complex structures [40]. By placing a mirror between the LDV and test specimen a high angle of incidence was simulated between the laser and the part [40]. The wavefield was then distorted to correct for this by mapping the plate coordinates on the measurement plane and then interpolating the values. As the measurement plane did not line up with the sample the wavefield was in essence compressed in one axis and stretched to correct it. Minimising distortion in the wavefield is crucial as it will cause distortion in the wavenumber-wavenumber domain. With filters being applied in that domain distortion will cause errors in wavenumber estimation.

While wavefields with curvature in a single plane can easily be projected onto a flat plane, no solutions are offered for parts that show curvature in two planes. A surface that is not developable can not be translated onto a single plane without some form of distortion. The problem investigated by Koskelo and Flynn [40] could

also be solved by the application of a 3D SLDV system that can use triangulation to determine the direction of velocity. It is also important to note that while it is possible to project wavefields of curved or angled surfaces onto a flat plane it requires information about the parts surface geometry and its positional relation to any measurement device such as a SLDV.

2.7.6 Multi-frequency excitation

Multi-frequency excitation was utilised by Flynn et al. [65] in conjunction with the AWS technique he had proposed [12]. A continuous excitation tone with three frequency components was used to generate a steady-state response in a 1.5mm thick aluminium plate and 7mm thick carbon panel [12]. While the excitation varied the processing algorithm did not stray far from previous work. The steady-state response was broken up into three distinct response maps, each at one of the tone frequencies [12]. These were then separately processed to give wavenumber maps for each response map. Due to the dispersive nature of Lamb waves a different wavenumber is prominent at a given thickness at the different frequencies. The wavenumber of the plate and the defect was plotted on a dispersion curve for a 1.5mm aluminium plate but no attempt was made to correlate to thickness or combine the three separate maps [12]. For the composite plate the anisotropic nature of the dispersion means even a simple comparison of expected and calculated values is not undertaken [12].

Juarez and Leckey [66] also demonstrated multi-frequency excitation in their work. They used chirp excitation as also used by Micheals et al. [74]. A 20kHz to 1MHz 1μs chirp was used to generate a transient wavefield. A spatial windowing technique as proposed by Leckey and Rogge and was applied [9, 66]. While a frequency range of 300kHz to 400kHz was used a window size of 10mm was selected as it would be twice as large a the A_0 wavelength at that frequency range in the given material [66]. As such, the dominant wavenumber for each spatial window at each frequency was determined. By calculating a dispersion curve for each ply thickness in the plate it was then possible to determine which dispersion curve best describes the wavenumber relations of each spatial window and frequency [66]. As such, a ply thickness can be assigned to each spatial window. Good results were shown using this method. Apart from the inherent limitations of using spatial windows a key limitation of this technique is the detailed prior knowledge required of the composite. A full description of the lay up is required to select window size and determine dispersion curves. Furthermore if the material displays anisotropic properties, as many complex composite structures do, the wavenumber will be different at different angles of propagation at the same material thickness and frequency. This also means the technique will not easily be extended to support steady-state excitation, placing

a limit on the minimum measurement time achievable. Multi-frequency excitation does show many benefits. Being able to generate a wavenumber map at different frequency responses is analogous to multiple single frequency measurements. This can allow results to be combined, reducing noise and increasing accuracy [12]. With that there is however a trade-off, as the more frequencies are excited, the lower the energy input at each individual frequency [12]. Lamb waves also attenuate differently at different frequencies and plate thicknesses [75]. Higher frequencies and thinner plate structures tend to display higher attenuation of Lamb waves for a given material [75]. Spatial resolution however drives the need to use a high frequency. Lamb waves are generally taken to only interact meaningfully with defects that are on a scale of their wavelength [66]. While this is a useful rule of thumb for techniques such as AU and AE, this limit is a result of the diffraction limit which states that a wave will diffract when it interacts with obstacles, in this case defects [76]. The full wavefield technique proposed in this work does however not rely on diffraction but rather a change in wavelength, as such it should be possible to resolve sub wavelength damage. The diffraction of waves on the scale of features is also one of the reason that not all frequencies will propagate will in composite structures. The internal structures of the composites will result in diffraction and attenuation of wavelengths on their scale. Due to these factors wavelength selection is particularly important when using a single frequency wave in composites.

It has been shown that Lamb wave interaction with defects it dependant on many aspects such as thickness frequency product and defect shape and size [77]. Without prior knowledge of the thickness of the structure, or when presented with a structure that has a large thickness range, single frequency excitation may not be able to adequately excite Lamb waves in all parts of the structure that will interact meaningfully with damage. As such, multi-frequency excitation offers great advantages when real world applications are considered. A further key step for realising this technique for real world application is reducing measurement time. A significant step forward was taken by Flynn et al. [78] who were able to utilise single frequency steady-state excitation in conjunction with continuous measurement using a SLDV. For a scan area of $314cm^2$, scan times as low as $0.7s$ were achieved. For higher signal-to-noise-ratios the scan time was increased to a maximum of $21s$.

One form of damage that does not effect the wavelength of a Lamb wave is through thickness crack damage. Techniques have been proposed to identify these damage types through wave reflections in wavefields. Ruzzene et al. [60] proposed a method of removing incident waves in the frequency-wavenumber domain to identify reflected waves and thereby visualise discontinuities in a structure through the use of a Root Mean Squared (RMS) map [60]. This process requires a transient wave and will also show up discontinuities that are part of the part geometry mak-

ing this technique less effective for complex geometries. A similar approach was taken by Michaels et al. [61]. A wavefield was filtered to a particular wave mode and then filtered in the frequency-wavenumber domain to remove the incident wave [61]. As such an RMS map can be created from the back scattered wave. This approach was also demonstrated on a composite plate with non-isotropic characteristics. Filtering in the polar domain while in the frequency-wavenumber domain allowed for mode separation even in non-isotropic plates [60] but the same limitations that applied to the work of Ruzzene et al. apply here. This work was based on frequency-wavenumber domain filtering but it did not attempt to directly determine the wavelength of a Lamb wave.

It has been shown that wavenumber based NDT techniques hold promise but are still limited in a number of respects. The use of spatial windowing will inherently limit spatial and depth resolution so is not considered a good option for determining damage based on wavenumber. The issues of spatial windowing are broadly addressed through the use of wave number filters in the spatial domain as presented by [12]. While addressing many of the shortcomings of instantaneous wavenumber techniques and methods that rely on spatial windowing, wavenumber filtering does not allow for the use of multi-frequency excitation to be combined into a single result as part of the technique. The use of multi-frequency excitation is important to ensure full excitation of complex structures. Furthermore, the use of different filter window shapes and widths has not been investigated but is known to significantly effect the depth and spatial resolution. The investigation of previous work also showed no direct optimisation of this technique for composite structures. While wavenumber based techniques have been demonstrated on composite parts, these have been limited to ones that are quasi-isotropic in their dispersion characteristics.

2.8 Conclusions

While there are a broad range of effective NDT techniques available there is still a clear need for a fast and effective technique that can be applied in a broad set of use cases. Full-field, guided wave based techniques offer solutions to many of these challenges, namely their potential for high speed as well as their ability to be applied in a non-contact configuration. Much work is however still needed to develop these techniques to the point where they can effectively be applied to complex structures and a variate of materials. A key requirement for any such technique, which is not met by excising techniques, is the lack of any requirement for prior knowledge of the structure or its material. The rest of this work seeks to meet this requirements and ultimately propose and innovative and effective full-field approach.

3. Wave mode spectroscopy

3.1 Introduction

This chapter proposes a novel method of bandpass mode filtering called Wave Mode Spectroscopy (WMS). Mode filter shapes were determined using the Rayleigh-Lamb equation and centred around a particular thickness in order to determine the most probable thickness at each measurement point. Contrary to previous methods that aim to determine the wavenumber in a response map at a particular frequency slice, a method was developed that utilises all the data in the frequency wavenumber domain. By finding the instantaneous amplitude post filtering to a given mode a thickness map can be found by assigning the thickness of the filter that maximises energy at each point. Unlike previous techniques this allows multi-frequency excitation to be used and analysed with a single filter stack as the dispersive nature of Lamb waves is taken into account. The aim of the algorithm proposed is to use multi-frequency excitation to achieve a greater data volume and attain low noise and accurate thickness maps. Multi-frequency excitation will further help ensure Lamb waves are generated in a broad range of plate thicknesses making it suitable for parts with thickness ranges larger then 5mm.

Current techniques are limited in this respect by their inability to utilise broadband multi-frequency data for a single result. The use of the full frequency domain data also helps to minimise the trade-off between spatial and depth resolution.

3.1.1 Aims and objectives

The aim of this chapter is to develop and demonstrate the concept of mode based filtering for thickness identification on isotropic plate-like structures. Particular challenges faced by other work help define certain requirements. Steady-state excitation was used to reduce measurement time and, to help improve spatial resolution, spatial windowing was not utilised. This work aims to demonstrate the ability of this algorithm by demonstrating it on two test specimens. A key limitation in previous work, and an inherent limitation of this method, is depth resolution. As such this work has a particular focus on obtaining high spatial and depth resolution at greater part thicknesses.

3.2 Experimental setup

This section covers the general experimental setup used to gathering full-field response maps.

3.2.1 Test specimens

Two test specimens were manufactured to test the algorithm developed in this chapter. The first one, specimen 1, was manufactured out of 6082 T6 Aluminium. It consisted of a 3mm x 350mm x 350mm plate with three circular areas of 30mm diameter with reduced thickness of 1mm, 1.5mm and 2mm. The low thickness and large defect area was chosen to test the algorithms ability to accurately determine thicknesses. The large defects would also give the ability to determine the clarity of thickness step changes. A thickness map of specimen 1 is given in Figure 3.1 (a).

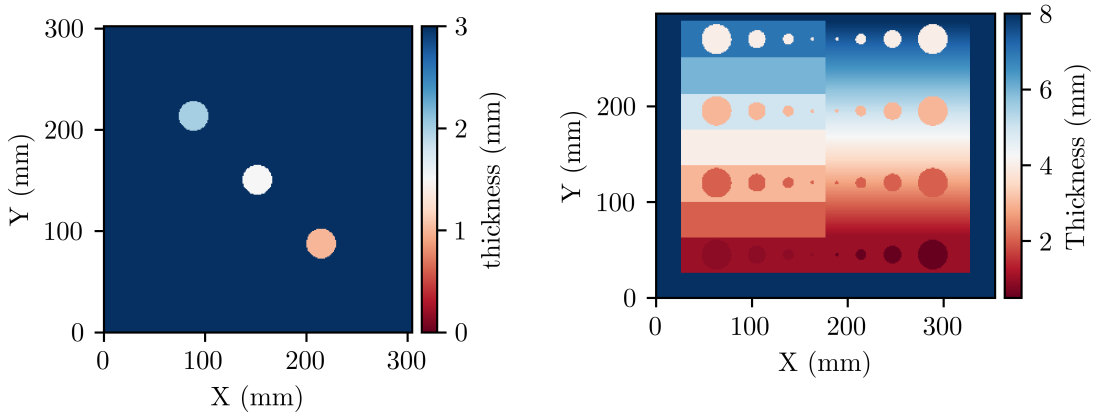

Figure 3.1: (a) specimen 1 and (b) specimen 2 thickness maps.

To validate the abilities of this algorithm over a larger thickness range a second plate, specimen 2, was also manufactured. Specimen 2 consisted of a flat 400mm x 400mm, 8mm thick 6082 T6 aluminium plate with a stepped and a ramped thickness change from 1mm to 8mm. Circular thickness changes were also present at every second 1mm thickness step and were mirrored on the thickness ramp. These were 30mm, 17.5mm, 10mm and 4mm in diameter. The 1mm thick area of the plate had thickness reductions from 1mm to 0.9mm and 0.5mm. Over the rest of the plate thickness reductions were from 3mm to 2mm, 5mm to 3mm and from 7mm to 4mm. This allowed spatial and depth resolution to be tested over a large range of thicknesses and defect size. A thickness map of specimen 2 is given in Figure 3.1 (b). Both thickness maps given in Figure 3.1 were calculated so that a pixel would represent the same spatial step as was taken between measurement points.

At smaller defects in specimen 2 this caused some quantization. As such these thickness maps can be thought of as ideal results. The resolution was however not limited in the thickness domain.

3.2.2 Signal acquisition

All measurements were completed using a 3D SLDV. The full-field data were captured using the Polytec PSV-500-3D-M in conjunction with an external camera. Data were exported from Polytec's proprietary software containing three-dimensional spatial coordinates of each sample point as well as the velocity in three dimensions for that point. For specimen 1 an area of 300mm by 300mm with an evenly spaced grid of 280 points in each axis was measured. For specimen 2 an area of 350mm by 300mm was measured with 285 and 239 samples in the respective directions. 50 measurements were averaged at each sample point. The maximum temporal sampling frequency of 2.56 MHz with a sample length of 0.0004 seconds was used. For specimen 2 this means that 23 minutes were required to capture all the temporal data. The measurement times were however between 20 and 30 hours with the extra time taken to perform steps such as 3D triangulation of the laser heads. No efforts were made to reduce measurement times at this stage in the work. The fact that the time spend on data capture is such a small proportion of the total measurement time, indicates that the measurement time can be reduced greatly.

3.2.3 Signal generation

The specimen plates were excited with either a Vallen System VS900-M PZT transducer with a face diameter of 20mm or a Pancom Pico-Z PZT transducer with a face diameter of 5mm. The Pancom Pico-Z transducer has a resonant range of $200kHz$ to $500kHz$ whereas the Vallen System VS900-M PZT transducer has a slightly broader resonant range of $100kHz$ to $900kHz$. For specimen 1 the transducer was located at $X = 312.5mm$ and $Y = -12.5mm$. The transducer location relative to the scan area is shown in Figure 3.3 (a). For specimen 2 the transducers were placed at $X = 175mm$ and $Y = 350mm$. Again the transducer location relative to the scan area is shown in Figure 3.3 (b). On both specimens transducers were coupled with grease and clamped to the specimen. For multi-frequency excitation a FM sine wave signal was modulated upwards between 75 kHz and 400 kHz at a rate of 2.45 kHz at 200Vpp. The FM signal was windowed using a Tukey window allowing the signal to be continually repeated without transient spikes between repetitions. The Tukey window, $w(n)$, of length n is given by Equation (3.1) [79].

$$w(n) = \begin{cases} 1, & 0 \leq |n| \leq \alpha\dfrac{N}{2} \\ 0.5\left[1 + \cos\left[\pi\dfrac{n - \alpha\frac{N}{2}}{2(1-\alpha)\frac{N}{2}}\right]\right], & \alpha\dfrac{N}{2} \leq |n| \leq \dfrac{N}{2} \end{cases} \tag{3.1}$$

As α varies from zero to unity, the window, of length N, varies from a rectangular window to a cosine window. Specimen 2 was excited using both transducers with the FM signal. Only the larger Vallen System transducer was used to generate the FM signal in specimen 1. As a comparison specimen 2 was also driven at single frequencies within the range of the FM excited. A continuous 200Vpp sine wave signal was driven at either 75 kHz, 150 kHz, 300 kHz or 400 kHz using the Vallen System transducer. All signals were generated using a Red Pitaya STEMLab 125-14 in conjunction with a Krohn-Hite 7500 amplifier. Figure 3.2 shows a steady-state multi-frequency response for both specimen 1, (a), and specimen 2, (b).

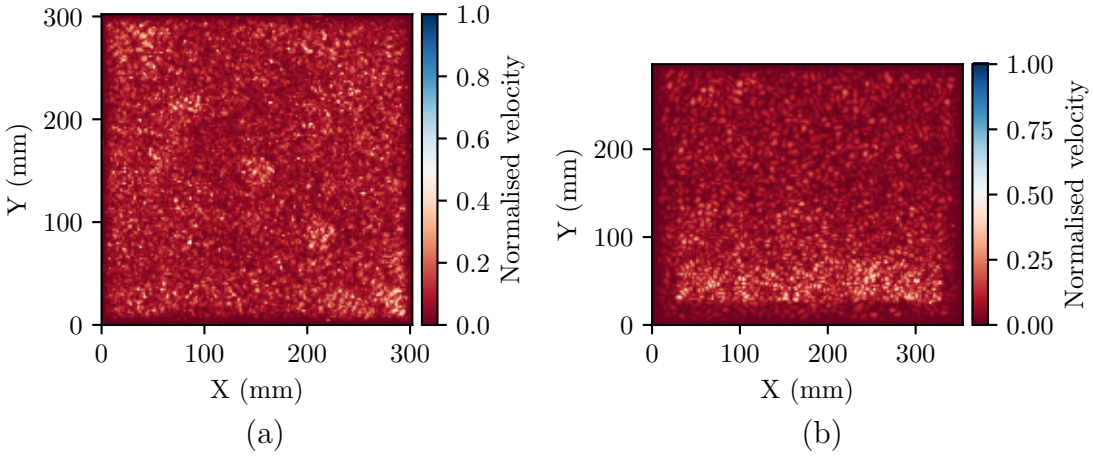

Figure 3.2: Response map at time t of (a) specimen 1 and (b) specimen 2.

While transient excitation can offer clear wavefield images the time taken to acquire data are significantly larger than that taken to acquire data from steady-state excitation. As an example a representative scan area of 300mm by 300mm with a spatial sampling resolution of $1000m^{-1}$ and 20 measurements per point would require 12 minutes for a full measurement assuming data are continually taken with a temporal sample length of 0.0004 seconds. For a transient measurement a ring down time would have to be added to let waves disperse, taking the time for a single measurement to 0.01 seconds resulting in a full measurement time of 10 hours. therefore steady-state excitation is chosen for this work. Steady-state excitation further allows signal-to-noise-ratio to be improved in smaller plates as waves will be reflected off all edges and thickness change features. While this adds complication to the nature of the wave-field it is a desirable feature as the multiple propagation directions add more information in the wavenumber-wavenumber domain to which each mode is filtered, reducing error. This effect could be further enhanced by

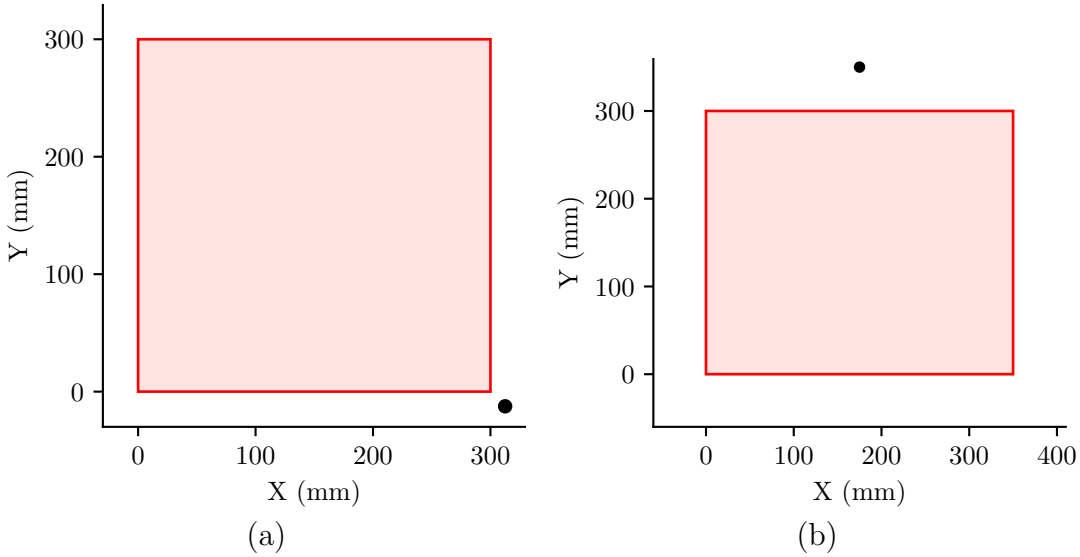

Figure 3.3: Measurement area (red) and transducer (black) of (a) specimen 1 and (b) specimen 2.

simultaneously driving multiple transducers on a single structure. The reflections within the plate also makes transducer location less critical as energy is relatively evenly distributed around the plate. This can be seen in Figure 3.2 (b) where it is not clear simply by the amplitude of the wavefield where the transducer is located. In larger structures with fewer reflective surfaces or materials such as composites with higher attenuation, increased damping as distance from the transducer is increased, is likely to affect measurements. This effect could also be mitigated by using multiple transducers. A diagram of the experimental setup is shown in Figure 3.4.

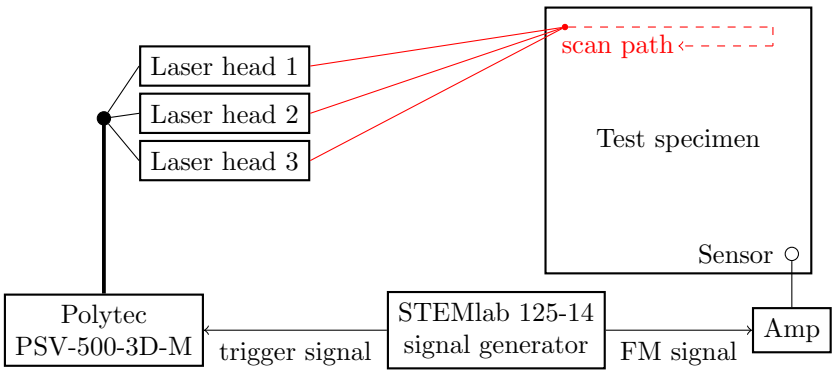

Figure 3.4: Experimental setup.

3.3 Processing algorithm

The following sections describe the developed processing algorithm used to calculate a thickness estimate map from wavefield data using WMS. While this is presented

as a general processing method for isotropic materials the steady-state FM response from specimen 1 is used to clarify and visualise a number of the processing steps. The nature of the algorithm means it can be applied to a broad variety of scenarios, using different windowing, excitation and frequencies. As such it is presented in general terms. The following sections investigate some of these aspects using the two test specimen constructed. Figure 3.5 shows a flow chart summarising the processing algorithm.

3.3.1 Dispersion calculation

Lamb waves are dispersive, that is to say their velocity changes with their frequency thickness product [14]. The relation between frequency, thickness and wavenumber are described by the Rayleigh-Lamb Equations [14] as given in Equations (2.14) and (2.15). The dispersion curves, in terms of frequency thickness product and wavenumber, was calculated using a bisection method. Further information on solving the Rayleigh-Lamb Equations can be found in [14]. Figure 3.6, shows dispersion curves calculated for the fundamental modes of both S_0 and A_0 waves in a 3mm thick aluminium plate.

For rolled aluminium $c_l = 6420ms^{-1}$ and $c_t = 3040ms^{-1}$ were used [80]. As solutions are simply points of a zero cross a process was used to identify separate modes where two close points were identified and a linear regression drawn between those points. The frequency value of the next point was taken and a wavenumber calculated using the linear relation determined from the previous points. If the actual wavenumber of the next point fell within a range of the value calculated from the linear relation it would be deemed to be part of the same line. For these thickness and frequency ranges the A_0 mode is used as its out-of-plane motion gives a better signal-to-noise-ratio. In addition its dispersive nature means that a greater change in wavenumber would be expected for a given thickness change compared with the S_0 mode. In different materials and thicknesses it may however be advantageous to use the S_0 mode. For examples in thicker materials or at higher frequencies the S_0 mode will become more dispersive.

3.3.2 Frequency-wavenumber domain data

The full-field wave velocity data that is captured can be stored in the form of a 3D matrix, $u(x, y, t)$, with two spatial domain axes, x and y, and one temporal domain axis, t. This will make further processing much faster and simpler as processes such as a FFT can be directly applied to the data. To ensure even spatial sampling, the wavefield at each time sample was interpolated in 2D using spatial coordinates as given by the 3D SLDV and re-sampled over an evenly spaced grid in the spatial

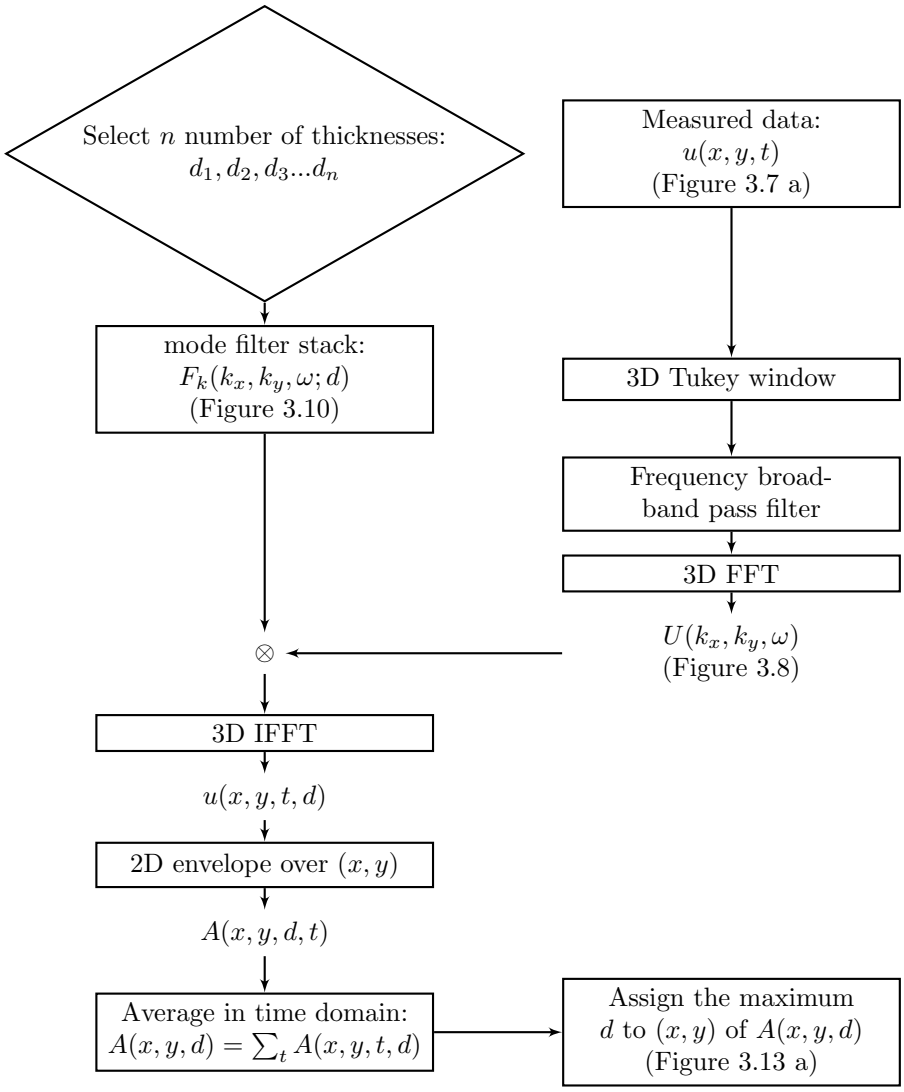

Figure 3.5: Thickness correlation algorithm flow chart.

domain of the same number of points measured. Interpolation was done using a cubic spline as in the analysis of Dierckx [81]. While 3D velocity data were gathered for this work only out-of-plane velocity was considered. A 1D LDV would have sufficed for this work, however the use of a 3D system will help allow this technique to be expanded to 3D structures in the future.

Figure 3.7 (a) shows a snapshot in time of the response of specimen 1 besides the true thickness map given in Figure 3.7 (b). Through visual comparison it is possible to identify areas of thinning. This is however not easily done through identifying a reduction in wavelength but rather an increase in velocity amplitude. It should be noted that there are noticeable differences in wavelength in the areas of consistent thickness due to the multi-frequency excitation present.

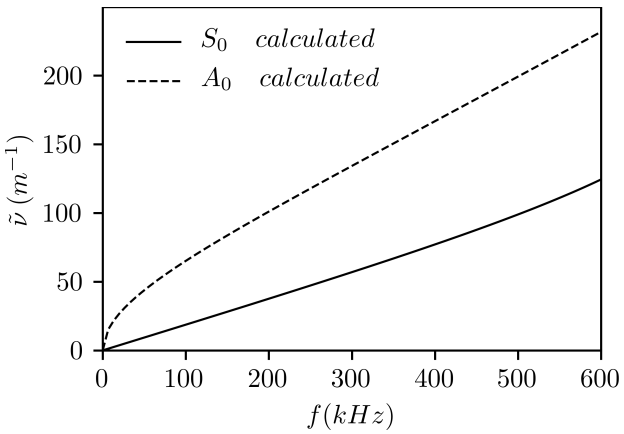

Figure 3.6: S_0 and A_0 dispersion curves for 3mm thick aluminium plate.

In order to convert the wavefield data to the frequency domain, $U(k_x, k_y, \omega)$, it is windowed using a 3D Tukey window. This is a 3D extension of the one dimensional Tukey window, w_n as given by Equation (3.1). A Tukey (also known as tapered cosine) window [79] was chosen for its ability to smooth to zero at the edges while minimising the amount of information lost [79].

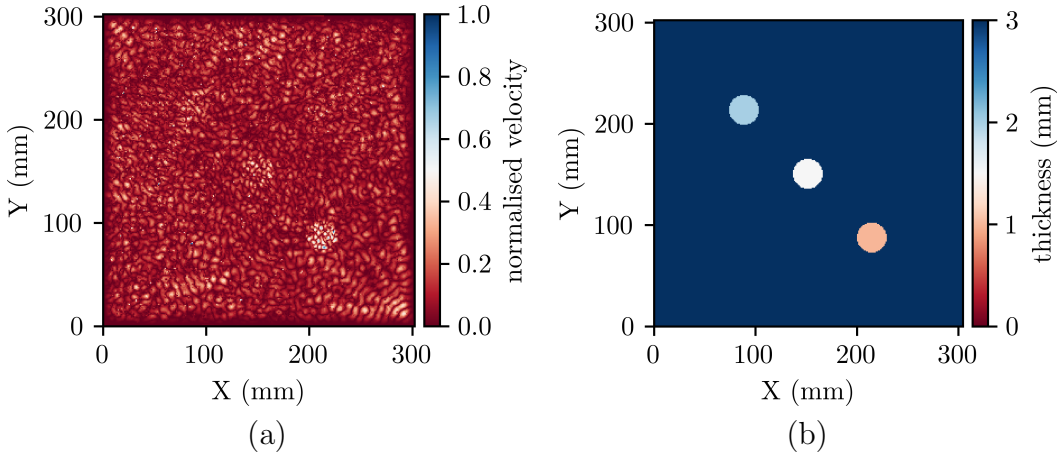

Figure 3.7: Specimen 1 (a) wave-field response at time t (b) True thickness map.

After windowing, the data are zero buffered spatially to the nearest power of two. Depending on the number of original samples taken this might result in a large zero buffer. While a large zero buffer will reduce the frequency bin size in the frequency spectrum, it can not be considered as a way of increasing frequency resolution. it must rather be thought of as interpolation in the frequency spectrum. This is important when considering frequency bin size in later steps of the process. The prime motivation for zero buffering is to ensure efficient execution of the FFT. A 3D FFT, as shown in Equation (3.2), is applied, converting each axis of the data into its corresponding frequency domain.

$$U(k_x, k_y, \omega) = \mathcal{F}_{3d}(u(x, y, t)) \tag{3.2}$$

While in the frequency domain a broadband bandpass temporal frequency filter may be applied which removes frequencies outside of the excitation range. Generally the pass band will be larger than the excitation frequency range and only be used to remove environmental noise rather then separating different frequency responses. A 3^{rd} order Butterworth bandpass filter was used as it has a very flat frequency response in the pass band [82] and any inaccuracies in cut-in and cut-off frequencies are not of great concern.

3.3.3 Lamb wave mode filter design

Using the Equations (2.14) and (2.15) the expected wavenumber for a given frequency and mode can be found. Figure 3.8 shows full-field data from specimen 1 sliced in a temporal (a) and spatial (b) frequency axes. On each figure values are also plotted that have been calculated for a 3mm thick plate using the Rayleigh-Lamb equations described in Section 3.3.1. Both Figure 3.8 (a) and (b) show a band of energy around the calculated values of the A_0 mode. A filter can be built around this distinct band of energy.

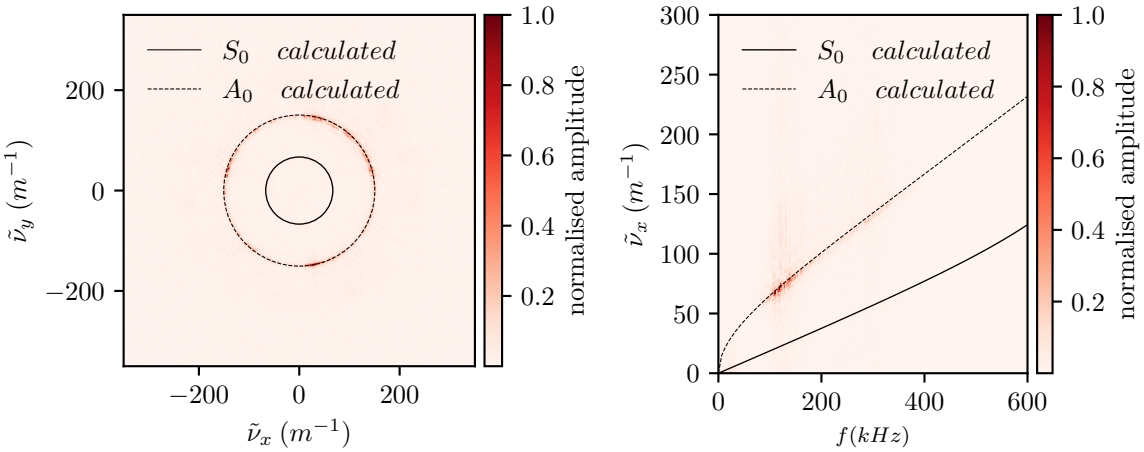

Figure 3.8: Frequency domain data $U(\tilde{\nu}_x, \tilde{\nu}_y, f)$ sliced at (a) $f = 200kHz$ and (b) $\tilde{\nu}_y = 0$ and Rayleigh-Lamb equation solutions.

To ensure symmetry in the wavenumber domain the filter is calculated as a stack of 2D filters at each frequency slice ω in the wavenumber-wavenumber domain.

The frequency slice of the mode filter was calculated in polar form, $F_\omega(k, \theta)$, where the value k is given by Equation (3.3) and θ is the angle ranging from 0 to 2π.

$$k = \sqrt{k_x^2 + k_y^2} \tag{3.3}$$

It is also worth noting that the angle of propagation, θ is given by Equation (3.4)

$$\theta = \left(tan^{-1} \frac{k_y}{k_x} \right) \tag{3.4}$$

For this example a flattop window was chosen but any windowing function, $w(n)$, can be applied. As can be seen in Figure 3.8, k will be constant for any angle of propagation for a given frequency due to the isotropic nature of the material. The bandpass center is given by k_{pass} and the bandpass width is given by k_{width}.

As such a bandpass wavenumber filter was calculated using Equation (3.5) where k_{width} is the width of bandpass window.

$$F_\omega(k,\theta) = \begin{cases} 0, & 0 \leq k \leq k_{pass} - \dfrac{k_{width}}{2} \\ w(k - k_{pass} - \dfrac{k_{width}}{2}), & k_{pass} - \dfrac{k_{width}}{2} \leq k \leq k_{pass} + \dfrac{k_{width}}{2} \\ 0 & k_\theta + \dfrac{k_{width}}{2} > k \end{cases} \tag{3.5}$$

Figure 3.9 shows a flattop filter slice in the polar domain with a bandpass width of $k_{width} = 240m^{-1}$ and a bandpass center of $k_{pass} = 120m^{-1}$.

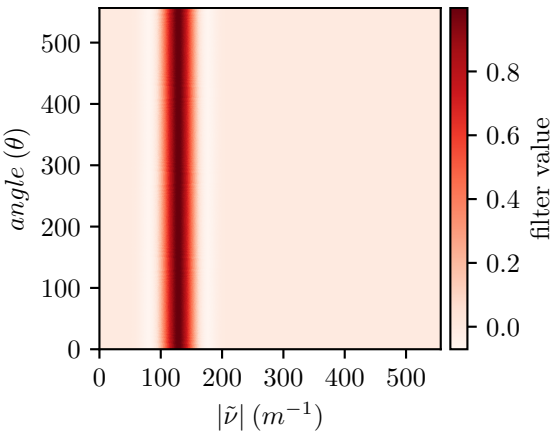

Figure 3.9: Wave mode filter, $F_\omega(k,\theta)$ at 350kHz.

Initially filters were calculated in the Cartesian coordinate system but this proved to be significantly less time effective in term of computation time. The polar form filter, $F_\omega(k,\theta)$, can then be converted into Cartesian form, $F_\omega(k_x,k_y)$.

The shape of the filter as well as its bandpass width affects the accuracy of the results. For similar image filtering problems a Gaussian filter is a common choice. This has also been used by Flynn et al. in a similar context [12, 78]. The full mode filter is created using the steps given below for a given mode, thickness and material:

1. Select frequency value, ω_0, of first frequency bin in $U(k_x,k_y,\omega)$.

2. Using the Rayleigh-Lamb Equations calculate the wavenumber value, k, for the selected mode and thickness, d at ω_0.

3. Create a 2D window, $F_\omega(k, \theta)$, with a centre value of k, as described by Equation (3.6).

4. Convert from Polar form to Cartesian form, giving $F_\omega(k_x, k_y)$.

5. Move onto next frequency bin and repeat steps 1-4 and stack the 2D filter slices created to create a matrix, $F_k(\omega, k_x, k_y; d)$.

Figure 3.10 (a) shows a slice of a filter created for specimen 1 centred around 3mm in the wavenumber domain. Figure 3.10 (b) shows the same filter sliced in the wavenumber-frequency domain along with calculated A_0 and S_0 dispersion curves. The filter has a bandwidth of $\tilde{\nu} = 200m^{-1}$ and is the shape of a flat top filter window.

It is now possible to create a filter bank, $F_k(k_x, k_y, \omega; d)$ of mode filters calculated about different thicknesses d where $d = [d_1, d_2, d_3...d_n]$. The dispersive nature of Lamb waves means that for a frequency the relationship between plate thickness and wave number change is non-linear. The thicknesses, d, of a filter bank should be chosen so that a maximum overlap between filters in the wavenumber domain is not exceeded.

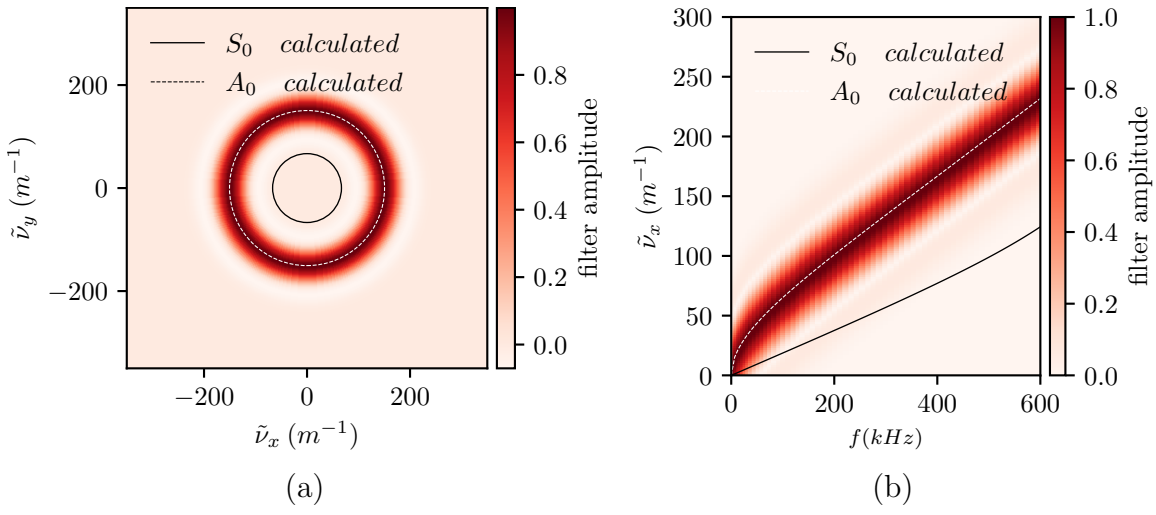

Figure 3.10: Frequency wavenumber filter, $f_k(k_x, k_y, f)$, sliced at (a) $f = 350kHz$ and (b) $k_y = 0$ and Rayleigh-Lamb equation solutions.

Figure 3.11 shows the relationship between wavenumber and thickness at a given frequency. This also demonstrates the reduction in thickness resolution at increasing thickness.

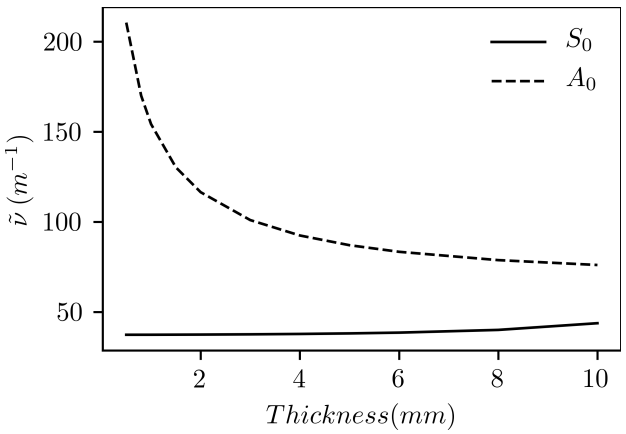

Figure 3.11: Thickness against wavenumber at $200kHz$.

3.3.4 Monogenic signal analysis

Once a wavefield has been filtered by the filter bank in the frequency-wavenumber domain an IFFT can be used to return the data to the temporal and spatial domain. The average of the absolute amplitude of the filtered wavefield at each time interval gives a measure of the amount of energy remaining after each filter has been applied.

In a one dimensional problem this would be completed using the Hilbert transform with which the complex analytic signal can be found and the envelope of a signal calculated. The Riesz transform is an extension of this same principle to higher dimensions [83]. The monogenic signal being the higher dimensional equivalent of the analytic signal. The monogenic signal is described in Equations 2.29, 2.27, 2.28. The monogenic signal is found in the spatial domain at each temporal sample to give the instantaneous local energy as used by Langley et al. [56] and Flynn et al. [78].

As with a 1D signal a large variety of scale in the signal causes inaccurate results [84]. Multi-frequency excitation means there are multiple wavelengths present but even at relatively large frequency ranges the range in wavelength is small enough to consider the signal as band limited after it has been mode filtered. No improvement in results were observed when using a scale space Reize transform where the signal is first bandpass filtered in the frequency domain [57]. For this work the python implementation of the monogenic signal was adapted from the work of Hidalgo-Gato and Barbosa [85].

3.3.5 Mode filter application

Once the filter bank, $F_k(k_x, k_y, \omega; d)$, has been calculated each filter at thickness d can be multiplied with the measurement matrix, $U(k_x, k_y, \omega)$ in the frequency

domain, before being returned to the temporal spatial domain with an inverse 3D Fourier transform, $\mathcal{F}_{3D}^{-1}$, as in Equation (3.6).

$$u(x, y, t; d) = \mathcal{F}_{3d}^{-1}[F_k(k_x, k_y, \omega; d)U(k_x, k_y, \omega)] \tag{3.6}$$

The local energy of each filtered response at thickness d can then be calculated using Equation (2.30) at each time step, giving $A(x, y, t, d)$. This is then be averaged in the time domain using Equation (3.7).

$$A_t(x, y, d) = \sum_t A(x, y, t, d) \tag{3.7}$$

Figure 3.12 shows results $A_t(x, y, d)$ for $d = 3mm$ and $d = 1.5mm$ for specimen 1.

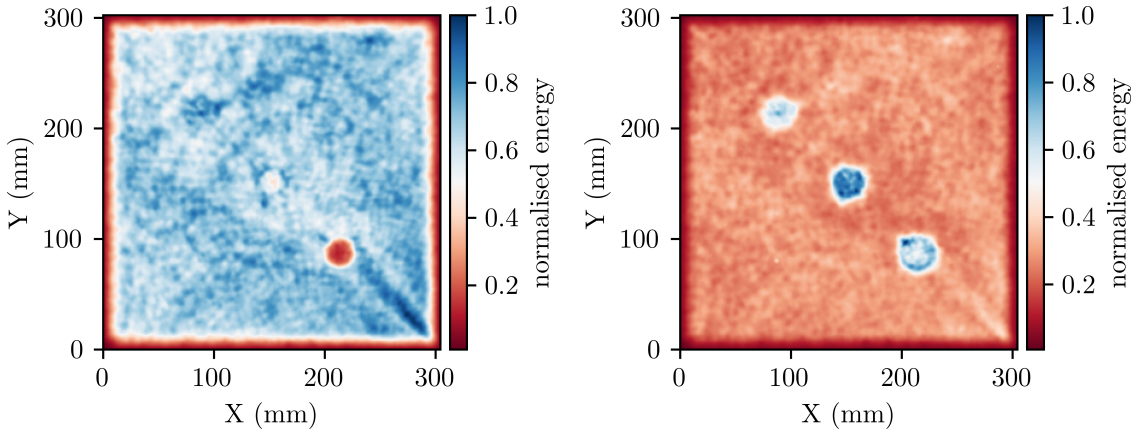

Figure 3.12: Specimen 1 energy after mode filtering, $A_t(x, y, d)$ (a) $d = 3mm$ (b) $d = 1.5$.

It is clear that when filtered to $d = 3mm$ the amplitude is greater in the bulk of the plate surface where the true thickness is 3mm. The area of least amplitude is at the greatest thickness reduction where the material thickness is 1mm. Likewise for the filter of $d = 1.5mm$ the central thinning displays the highest energy. The two other thinnings of similar thicknesses follow closely.

The filter thickness, d_n, of the filter which maximises the energy at sample point (x, y) is then assigned to that point creating a thickness map $d(x, y)$ as given by Equation (3.8).

$$d(x, y) = \max_d A(x, y, d) \tag{3.8}$$

Specimen 1 measurements were filtered using a flattop shaped mode filter and a bandpass width of $\tilde{\nu} = 200m^{-1}$. The thickness to which the mode filters were calculated were chosen so that they would have a minimum separation of 0.25mm or

a minimum separation of $\tilde{\nu} = 3m^{-1}$, whichever was smaller. A value of $\tilde{\nu} = 3m^{-1}$ was chosen as this was approximately the width of each frequency bin in the wavenumber domain. This gives a large overlap between filters leading to an over-complete interpretation which helped give consistent and repeatable results.

The thickness map calculated for specimen 1 is shown in Figure 3.13(a) and the error, which is given by subtracting true thickness from the measured results, is shown in Figure 3.13(b). A low thickness error is shown across the specimen with higher error around the edges of the thickness changes. This is likely due to the limited spatial sampling frequency, with over 1mm between spatial sample points as well as the fact that the wavelengths of generated Lamb waves range from approximately $17mm$ to $6mm$. This will result in a small region where a change in wavelength cannot be identified.

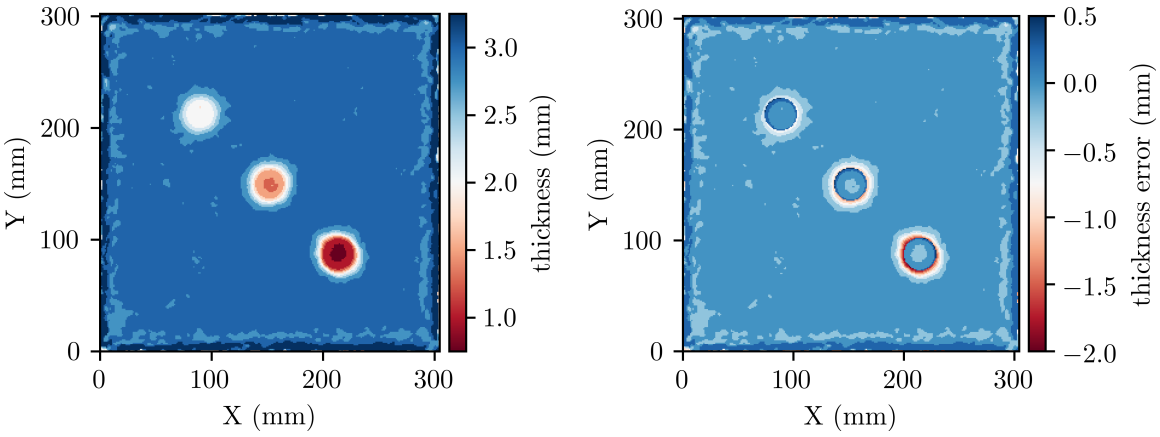

Figure 3.13: Specimen 1 (a) Specimen 1 resulting thickness map (b) thickness error.

3.3.6 Mode filter optimisation

In previous papers that use wavenumber domain filtering, Gaussian filters were used at a single bandwidth [12, 78]. This is a common choice in similar image processing applications. Work by Felsburg et al. [84] shows the importance of filter shape selection when applying a scale space before calculating the monogenic signal. Seeing as this work essentially replaces the application of a scale space with the application of the mode filter its shape is of equal importance.

To further investigate the selection of filter bandwidth the ideal thickness maps, $I(x, y)$, shown in Figure 3.1 were used to calculate a Mean Percentage Error (MPE). Using Equation (3.9) the MPE was calculated for each matrix of results, $d(x, y)$, where n is the number of spatial sampling points.

$$MPE = \frac{100}{n} * \sum_{t=1}^{n} \frac{I(x,y) - d(x,y)}{I(x,y)} \tag{3.9}$$

While attempts where made to align the specimen so that it aligned with measured results, the low spatial sampling frequency means that an offset of just 2 pixels results in a 2mm spatial error. As such it is best to think of the MPE scale not as absolute but rather a comparative index.

3.4 Results and discussion

Results were calculated using a Gaussian filter with a standard deviation of $\sigma = 15$ and a Flat top filter over a range of widths from $\tilde{\nu} = 50m^{-1}$ to $\tilde{\nu} = 500m^{-1}$. A value of $\sigma = 15$ was chosen as it gave a zero value at the filter edge for all filter widths considered and has been shown to useful in similar contexts [86]. Figure 3.14 shows the MPE as given by Equation (3.9) over a range of bandpass widths and both filter shapes. These values were calculated for specimen 2 excited using the 75kHz to 400kHz FM excitation in conjunction with the Vallen driving transducer.

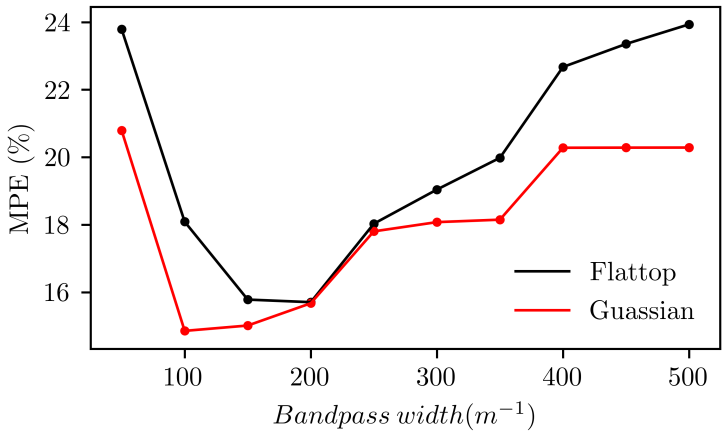

Figure 3.14: MPE with different window sizes and shapes.

3.4.1 Single frequency results

Resulting single frequency thickness maps calculated using a flat top shaped filter of width $k_{pass} = 200m^{-1}$ are shown in Figure 3.15. The same data were processed using a Gaussian filter window with a sigma value of $\sigma = 15$ and $k_{pass} = 100m^{-1}$. These results are shown in Figure 3.16. While a full mode filter was applied over the entire frequency range a single frequency slice was clearly dominant making it comparable to a single frequency slice being passed through a simple wavenumber filter bank, as done in previous work [12, 40, 64, 78]. Unlike most of the previous work the wavenumber here is related back to thickness using the Rayleigh-Lamb equations.

The 1mm to 3mm thick areas of the specimen are generally well resolved in all single frequency results shown in Figure 3.15 and 3.16. Thickness changes of 0.5mm at 1mm are visible down to a diameter of 10mm. At the higher frequencies of 300 kHz and 400 kHz the 4mm diameter thickness change is also visible. At the spatial sampling frequency, 4mm represents about three samples (or pixels). The 0.1mm thickness change at 1mm plate thickness is not well resolved with some being visible at lower frequencies but without clear edges. As the frequency increases the maximum resolvable depth appears to reduce.

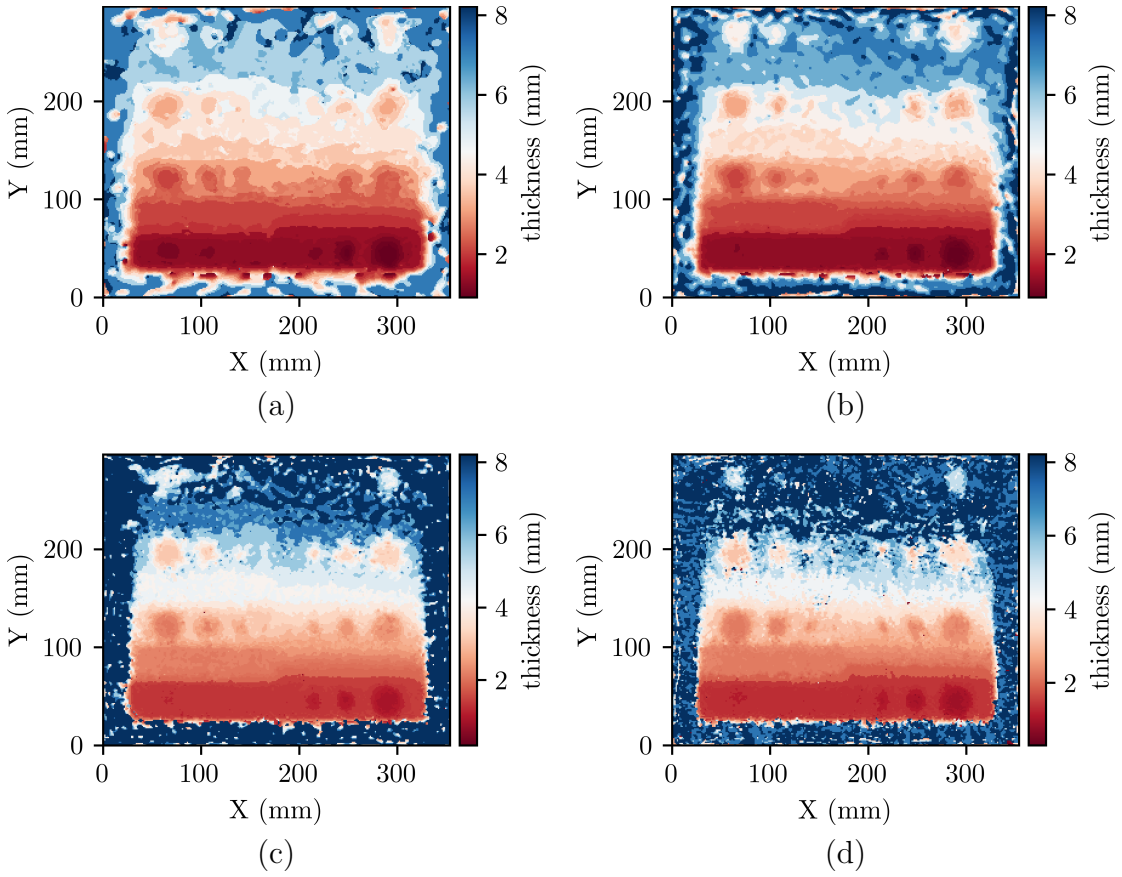

Figure 3.15: Single frequency Vallen transducer excitation and a flat top filter $k_{pass} = 200m^{-1}$ (a) 75 kHz (b) 150 kHz (c) 300 kHz (d) 400 kHz.

At the lower excitation frequencies of 75kHz and 150kHz the regions of 7mm and 6mm are approximated to that thickness. At the higher frequencies of of 300kHz and 400kHz thicknesses larger than 6mm are increasingly estimated to be the maximum thickness of 8mm. The two different filter shapes do not generate markedly different results. The Gaussian filter does however produce results with the lowest MPE.

3.4.2 FM results

In Figure 3.17 the resulting thickness maps are shown for FM excitation processed using the same flat top and Gaussian shaped filter banks as applied to the single

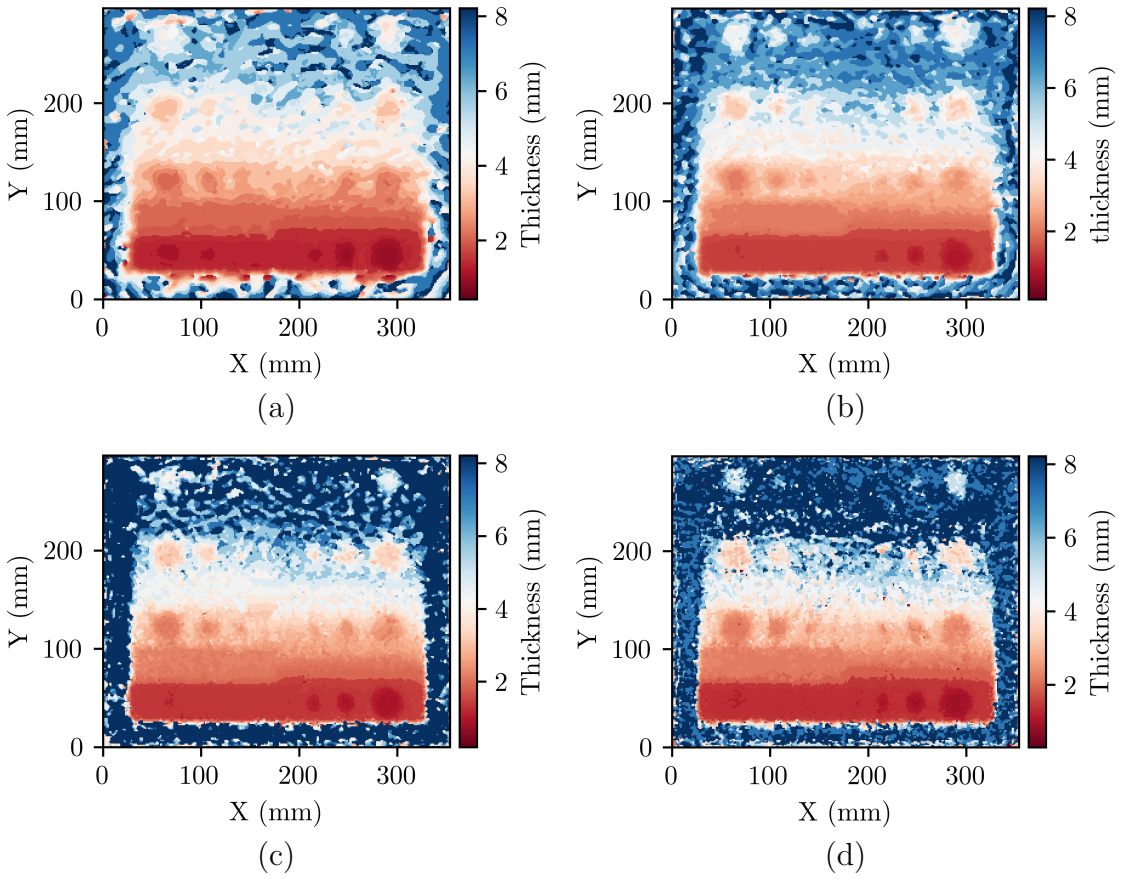

Figure 3.16: Single frequency Vallen transducer excitation and a Gaussian filter $k_{pass} = 100m^{-1}$ (a) 75 kHz (b) 150 kHz (c) 300 kHz (d) 400 kHz.

frequency results. In Figures 3.17 and 3.18 both a Vallen and Pico-Z transducers were used separately to excite specimen 2.

Likewise Figure 3.18 shows the thickness maps for FM excitation using the Gaussian shaped filter.

While the Vallen transducer was able to generate much larger amplitude, and therefore better signal to noise ratios, the results are very similar. A comparison of the out-of-plane velocity for a sample point is shown in Figure 3.19.

The Pico-Z and Vallen transducers also have different resonances, resulting in different frequencies being excited to different levels in the structure. Figure 3.20 shows the mean frequency response of all points for the two excitation methods. The frequency data were normalised to give a better relative comparison. Despite the differences in excitation the comparative nature of the filtering technique gives highly consistent results.

FM excitation results show greater feature clarity across the plate with a smoother thickness map giving a better representation of true thickness with substantially less noise in the thickness estimates. The multi-frequency excitation means there is more information present in the frequency-wavenumber domain. As an example with the temporal sampling frequencies used here the FM excitation

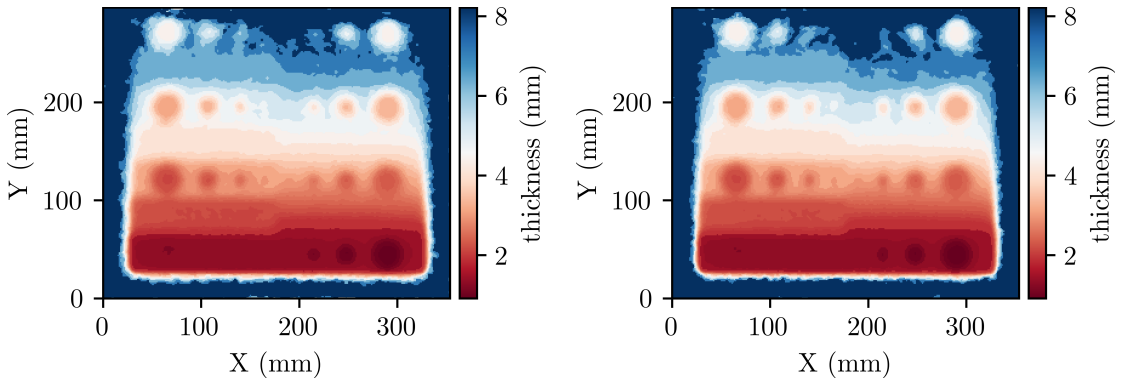

Figure 3.17: 75kHz to 400kHz FM excitation signal and flat top filter $k_{pass} = 200m^{-1}$ (a) Vallen transducer (b) Pico-Z transducer.

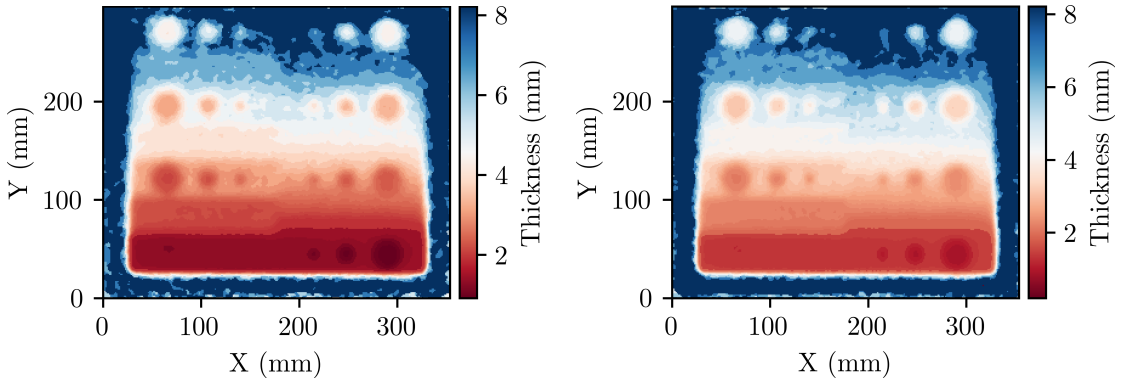

Figure 3.18: 75kHz to 400kHz FM excitation signal and a Gaussian filter $k_{pass} = 100m^{-1}$ (a) Vallen transducer (b) Pico-Z transducer.

covered over 130 frequency slices in the frequency domain, compared with one to two frequency slices excited by single frequency excitation. This greater quantity of information that is able to be gathered is likely one of the reasons edges and features are resolved with less noise in the FM results.

For all single frequency excitation at thickness larger than 4mm clarity becomes limited and the 30mm diameter thickness changes become distorted and difficult to identify at 7mm plate thickness. The results shown in Figure 3.17 and 3.18 on the other hand show good clarity down to a defect size of 17.5mm diameter even at a thickness of 7mm. The noise in thickness estimate present in single frequency results is on a scale of the wavelength of the excitation frequency. While at low frequency larger thicknesses are better resolved, as in Figure 3.15 (a), at the highest frequency of 400 kHz the maximum thickness value is assigned to most points thicker than 5mm.

With FM excitation the noise is at very low levels with consistent thickness readings across areas of uniform thickness. At thicknesses larger then 6mm the depth

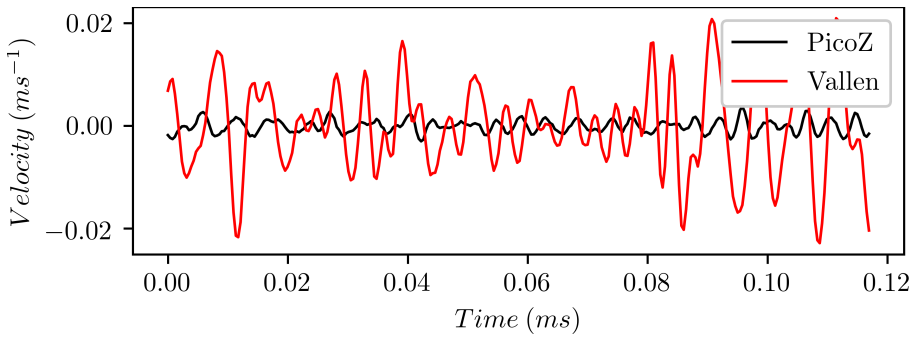

Figure 3.19: Velocity profile of out of plane displacement at $X = 247mm$ and $Y = 247mm$.

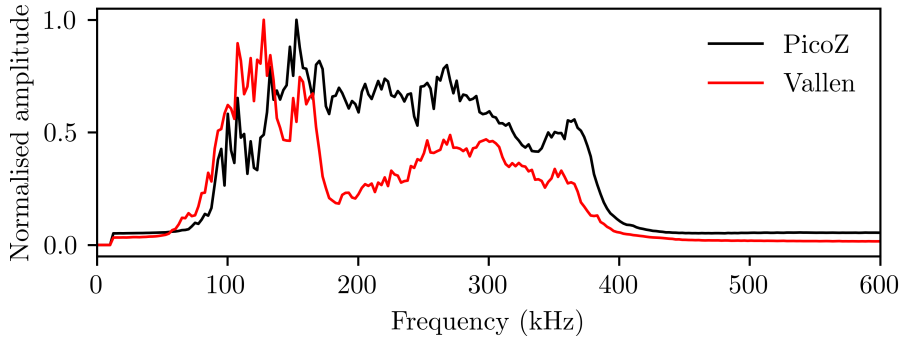

Figure 3.20: Mean normalised frequency response with Vallen and Pico-Z.

resolution drops off and the thickness map begins to lose accuracy. It is important to note that at the larger thickness of 7mm a wavenumber change of $\tilde{\nu} = 3m^{-1}$ corresponds to a thickness change of over a millimeter leading to quantisation in the thicknesses.

For a given material and thickness Lamb wave modes will attenuate at different rates for different thicknesses and frequencies [75]. As such any single frequency may not be ideal for propagation in a structure with a large thickness range. FM excitation requires little prior knowledge of the part being inspected as excitation frequencies do not have to be chosen for a particular thickness range. Figure 3.21 shows a map of the dominant frequency in the time domain at each spatial point. This was achieved by performing a FFT in the time domain at each spatial sample and taking the frequency of the maximum peak for a given spatial point.

While no clear trend can be drawn from this, as the resonant behaviour of the driving transducer appears to be the dominant factor, it does show some change in dominant frequency between the 8mm thick surrounding of the plate and thinner central parts.

Table 3.1 shows the wavelengths of the A_0 mode at different frequencies over a range of plate thicknesses. Lamb waves will only interact with defects on the scale of, or larger, than their wavelength [14]. Furthermore the wavelength of a Lamb wave is greater than the thickness of the material [87].

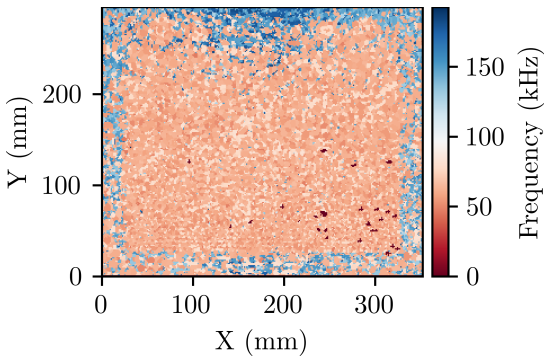

Figure 3.21: Map of dominant frequency for FM excitation in specimen 2.

Table 3.1: A_0 mode wavelength at different frequency and plate thickness.

A_0 wavelength (mm)	Plate thickness		
Frequency (kHz)	1mm	4mm	8mm
25kHz	19.54	38.00	51.92
75kHz	11.07	20.48	26.41
400kHz	4.29	6.35	6.90
550kHz	3.50	4.84	5.11

These results verify the behaviour observed in the single frequency excitation results for specimen 2. The higher frequency excitation of 400kHz, with shorter wavelength, interacted with smaller defects and gave better spatial resolution. At a plate thickness of 8mm the wavelength was too short to form Lamb waves resulting in poor thickness approximation. This is the likely explanation for sudden drop off in depth resolution seen at high frequency single frequency excitation. At the lowest single frequency excitation of 75kHz the wavelength is long enough to generate Lamb waves in the whole range of plate thickness. With a wavelength of 11mm in 1mm plate thickness spatial resolution is however limited. At a plate thickness of 8mm the wavelength grows to 26mm further reducing spatial resolution.

Figure 3.22 shows the gradient of the wavenumber for the A_0 mode over a range of thickness for both highest and lowest frequency in the FM excitation range. As the gradient reduces so does the ability to identify changes in thickness.

The lower frequency has greater change in wavelength improving depth resolution. This demonstrates the trade off between depth and spatial resolution.

While FM excitation outperformed single frequency excitation it is important to note that FM excitation spreads energy over a large frequency range leading to a trade-off between signal-to-noise ratio and the bandwidth of the FM excitation. It is noted that the edges of the plate suffer from edge effects due to the spatial windowing applied. If completing larger scans this would simply require a small overlap between scan areas to resolve.

Despite the same frequencies being covered with FM excitation none of the single

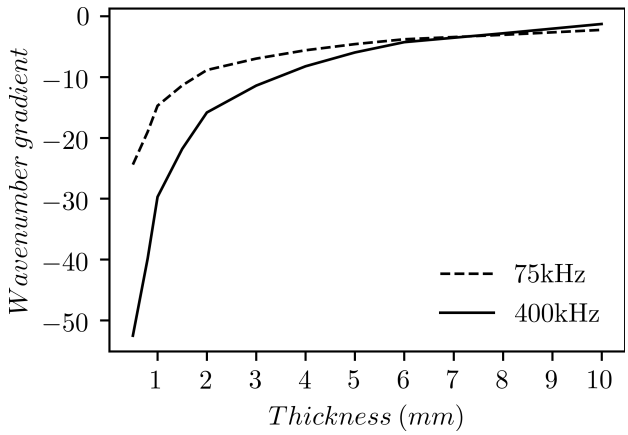

Figure 3.22: A_0 gradient over thickness range.

frequency results are able to give the same accuracy at the larger thicknesses. This shows that it is not simply a matter of the excitation frequency being appropriate for a given thickness but that mode based filtering is able to exclude information that does not conform to the behaviour of the A_0 Lamb mode in the wavenumber-frequency domain and therefore gives a better measure of the likely thickness.

Figure 3.23 shows thickness for slices in the Y direction of Specimen 2 at $X = 200mm$ along the ramp. Thickness is overestimated across all thickness maps with the 1mm thick area being estimated at 1.34mm. As shown in Figure 3.23 this error reduces as thickness increases but the tendency to overestimate remains. For the Gaussian window with $k_{pass} = 100m^{-1}$ slices along the x axis were taken to compare results. Lower frequencies shown in Figure 3.23 (a) match the FM results closely until around the 4mm thickness at which point the thickness of the single frequency excitation results begin to lose accuracy. At thicknesses greater then 5mm the FM excitation begins to outperform the single frequency excitation significantly with large spikes and dips in thickness estimates in single frequency measurements. The higher frequency single frequency excitations shown in Figure 3.23 (b) match actual thickness well until 3mm. At thicknesses larger than 5mm the thickness estimate of the high frequency single frequency excitation begins to break down. 400 kHz for example gives estimates ranging from below 4mm to over 8mm in a very small area with a true thickness of 6mm.

To give a better idea of the behaviour over the stepped thickness changes the same results are shown in Figure 3.24 at $x = 153mm$.

The stepped thickness changes are somewhat smoothed by all thickness estimates. As with the ramped thickness changes a constant offset for all frequencies is observed at the 1mm thickness.

The Lowest MPE of 14.86% is given by a Gaussian filter with a bandpass width of $\tilde{\nu} = 100m^{-1}$. While this filter gives the lowest mean percentage error it is not necessarily the best filter for resolving all the thicknesses present on specimen 2 as

percentage error of thin areas of the plate will have a larger effect on the MPE.

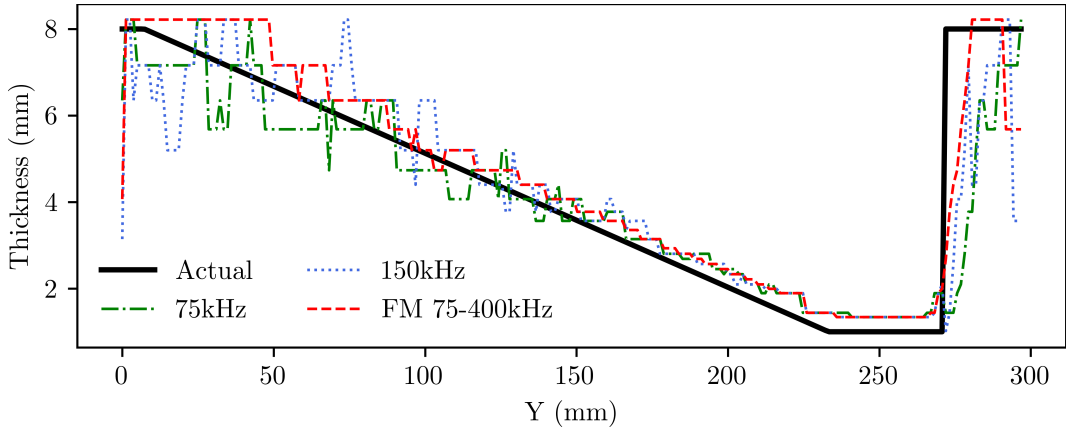

(a)

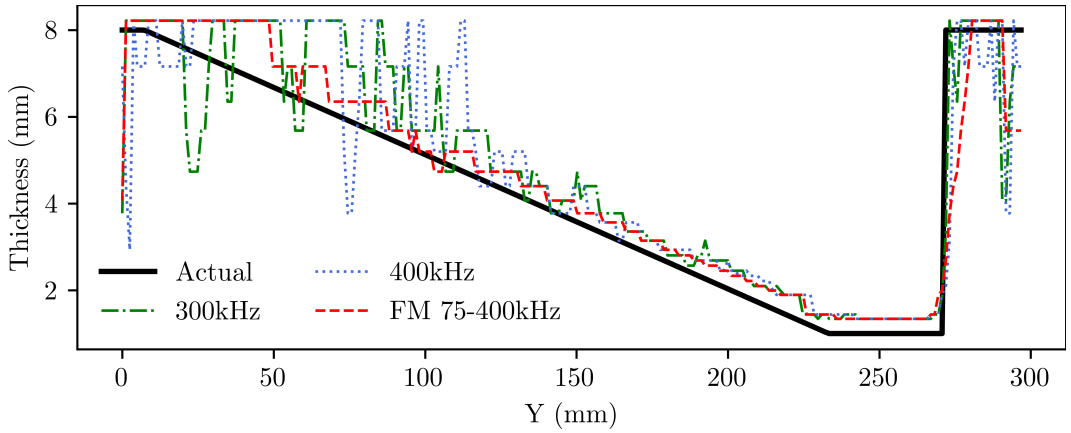

(b)

Figure 3.23: Horizontal slice at X=200mm (a) low frequencies (b) high frequencies.

MPE was also calculated for all four steady-state excitations as well as the FM excitation and is shown in Table 3.2. The values are calculated for the area of the plate were Y is larger then 150mm, the thick half of the plate, and the lower half where Y is less then 150mm, containing the thinner areas of the plate. Both area classifications still contain the 8mm thick border.

When considering the entire plate FM excitation outperforms all single frequency excitation with the 300 kHz single frequency excitation showing the best results of single frequency excitation. When examining the thicker area of the plate the FM excitation greatly outperforms any of the single frequency excitations. The 300 kHz single frequency excitation does however match FM excitation when only examining the thinner areas of the plate. The smaller thickness also means that any error due to quantisation will result in a larger percentage error. While MPE gives a measure of error it does not paint a complete picture of the clarity of the results. When looking at the resulting thickness maps shown in Figure 3.15 and 3.17 it is clear that the FM excitation offers clearer results with more defined features that closely

match the ideal thickness map. Without prior knowledge of a part or for parts spanning multiple thickness ranges the advantage of FM excitation in combination with WMS is clear.

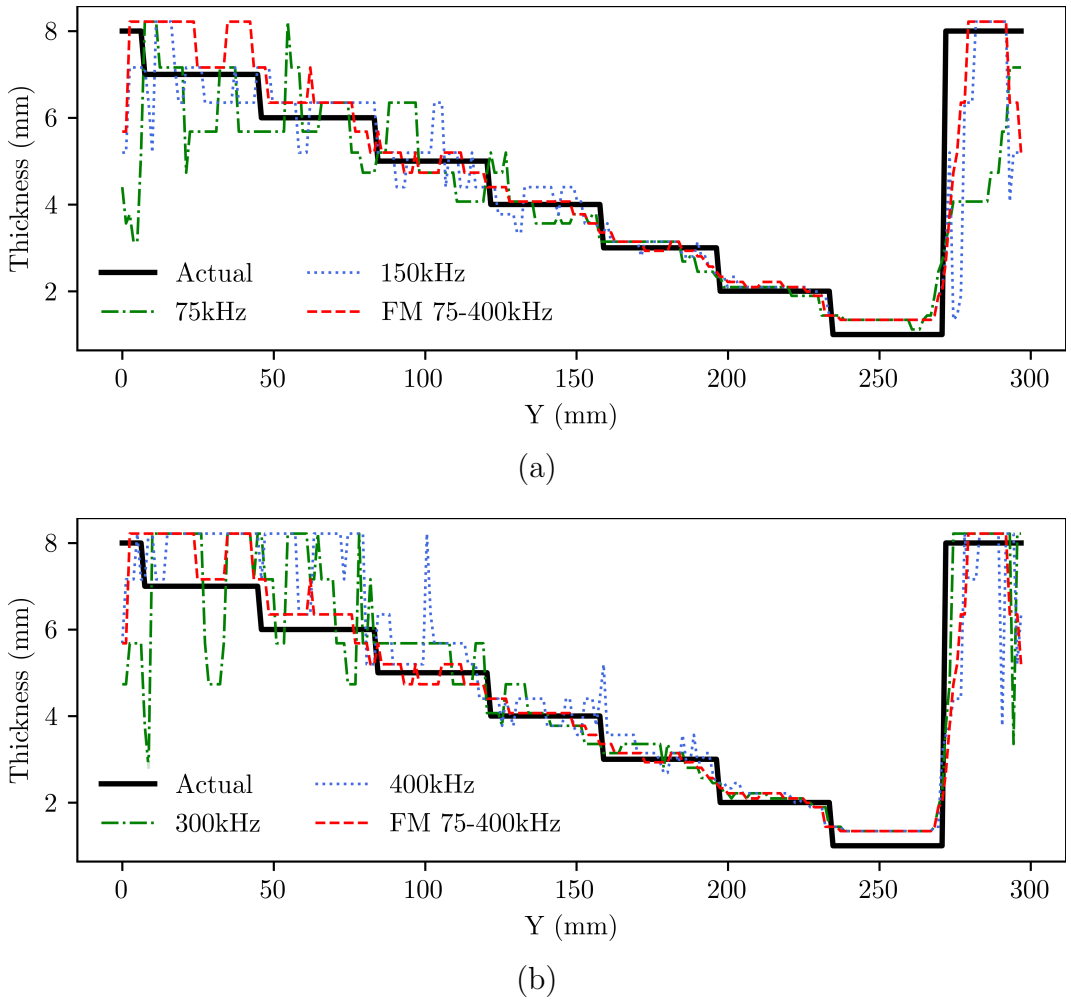

Figure 3.24: Horizontal slice at X=153mm (a) low frequencies (b) high frequencies.

3.4.3 Filter width

Further to the results given in Table 3.2, Figure 3.25 shows resulting thickness maps from different bandpass filter widths for flat top filters. While a Gaussian filter gave the lowest MPE, flattop filters offer a good shape for comparison of bandpass widths as they will always be zero at their edges. At the lowest filter width a general idea of thickness can be gauged but a very low spatial resolution is present. The narrow band filter applied in the frequency domain will generate 'ringing' features when returned to the spatial domain [88]. While the filter shape should not generate large artifacts the narrow nature of it will result in a bad approximation of the filter shape. With a bin size in the frequency domain of between $3m^{-1}$ and $4m^{-1}$ the filter is represented by only 16 bins in the filter.

Table 3.2: MPE at different areas.

Excitation	Transducer	Area	MPE
75kHz	Vallen	all	19.93%
150kHz	Vallen	all	18.68%
300kHz	Vallen	all	18.25%
400kHz	Vallen	all	20.21%
75kHz - 400kHz	Vallen	all	14.86%
75kHz - 400kHz	Pico-Z	all	14.79%
75kHz	Vallen	Y > 150mm	12.94%
150kHz	Vallen	Y > 150mm	12.42%
300kHz	Vallen	Y > 150mm	14.36 %
400kHz	Vallen	Y > 150mm	18.09%
75kHz - 400kHz	Vallen	Y > 150mm	8.32%
75kHz - 400kHz	Pico-Z	Y > 150mm	8.71 %
75kHz	Vallen	Y < 150mm	26.66 %
150kHz	Vallen	Y < 150mm	25.50%
300kHz	Vallen	Y < 150mm	24.30 %
400kHz	Vallen	Y < 150mm	23.68%
75kHz - 400kHz	Vallen	Y < 150mm	23.38%
75kHz - 400kHz	Pico-Z	Y < 150mm	22.94 %

As a higher filter width of $200m^{-1}$ is applied feature clarity is drastically improved. The 8mm thick region around the edge is however poorly resolved. With an even larger filter width of $350m^{-1}$ feature edge clarity is improved further and the 8mm thick bounding area is well resolved. Thickness steps in the left region of the plate are also clearly identified. Saturation is however reached at thicknesses greater than 6mm. At the maximum filter bandwidth of $500m^{-1}$ all areas of thickness greater than 5mm are estimated to be the maximum thickness of 8mm. Figure 3.26 shows a slice of the FM generated data in the frequency domain, $U(\tilde{\nu}_x, \tilde{\nu}_y, f)$, of specimen 2 at $\tilde{\nu}_y = 0$ and $f = 300kHz$. Also included on the figure are the slices of the 6mm mode filter with bandpass widths of $k_{pass} = 200m^{-1}$ and $k_{pass} = 400m^{-1}$

The wider filter is so wide that the filter is cut off at the zero wavenumber value for low k_{pass} values. As the k_{pass} value increases the filter will contain more energy regardless of material thickness changes. The comparative nature of the filter therefore will bias thickness estimates toward the mode filter centered around a greater thickness. For the narrower filters this same problem will still occur at low frequency thickness products. therefore an over estimate of thickness at lower true plate thicknesses is to be expected. The use of a filter such as a log-Gabor filter may help combat this issue as it will always have zero gain at $k = 0$. The change in bandwidth as the bandpass center approaches zero will however still bias the measurements in a particular direction.

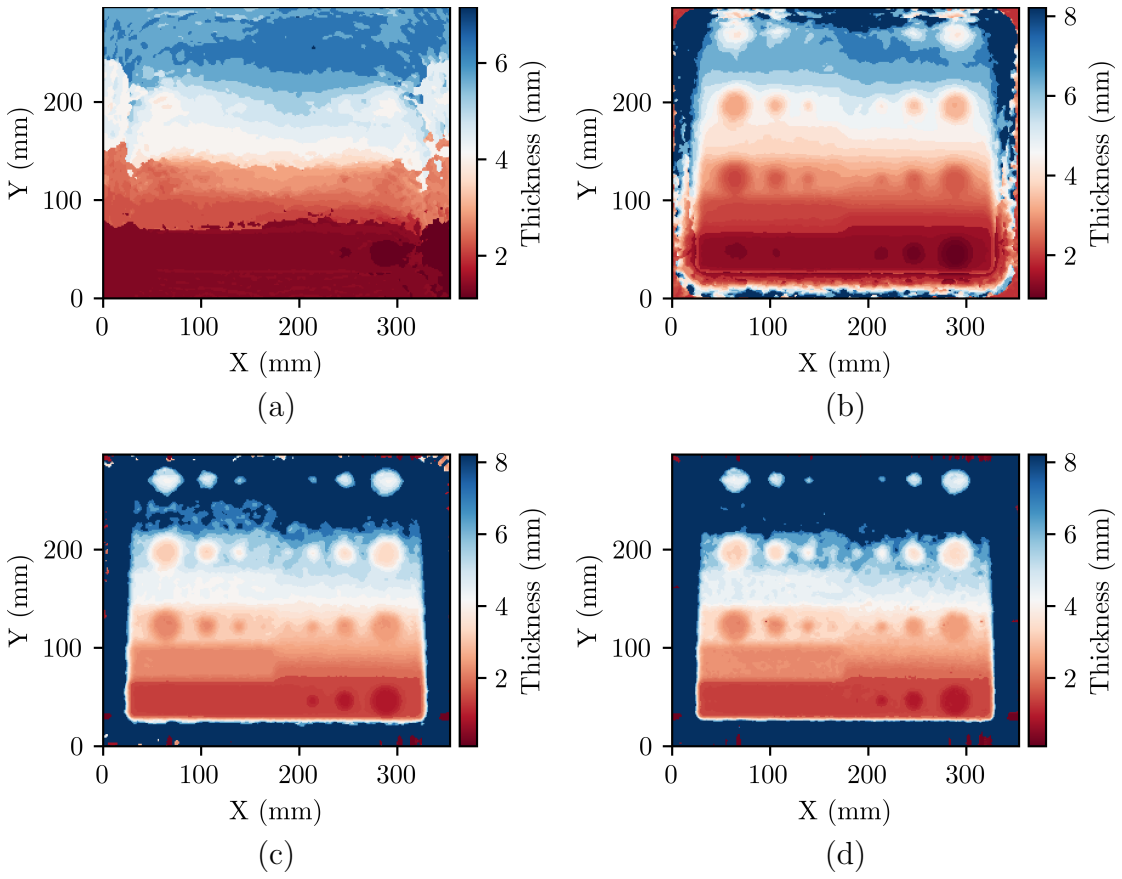

Figure 3.25: FM excitation results using Vallen transducer filter with a flat top k_{pass} of (a) $50m^{-1}$(b) $200m^{-1}$ (c) $350m^{-1}$ (d) $500m^{-1}$.

These results seem to indicate that a wider filter pass-band in the frequency domain improves spatial resolution by limiting ringing artifacts. Limits are however faced when a wider pass-band has a non zero gain at $k = 0$, which will result in a more complete filter representing a larger thickness returning higher comparative energy.

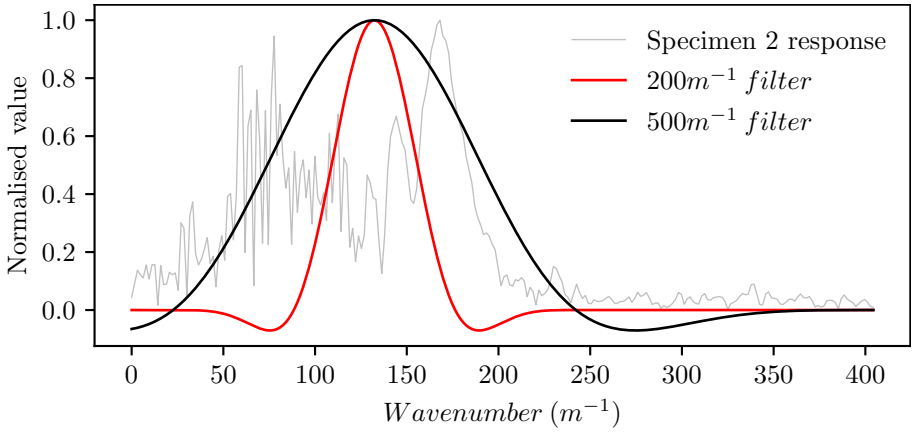

Figure 3.26: $U(\tilde{\nu}_x, \tilde{\nu}_y, f)$ at $f = 300kHz$ and $\tilde{\nu}_y = 0$ with mode filter centred around 6mm.

3.4.4 Steady-state mode generation

When using steady-state excitation it was observed that A_0, SH_0 and S_0 modes were being generated. This can be seen by the three distinct bands of energy in the wavenumber-wavenumber domain. These fundamental modes of S_0 and SH_0 are present at the same thickness frequency product used in this measurement. To further investigate this behaviour a transient measurement was taken on specimen 1. This investigating was performed on specimen 1 as the lower thickness variability made visualising modes in the frequency domain simpler. Specimen 1 was excited using a 300kHz, 10 pulse sine wave at 200Vpp. As specimen 1 is not large in size compared to the scan area it does not take long before reflections from the edges are generated. To simulate data taken on a larger plate the measurement time was reduced to $86\mu s$ as to only include the forward propagating wave. All other settings were kept the same as with steady-state excitation including transducer location and type. Figure 3.27 shows the frequency domain data for both excitation regimes at $f = 300kHz$. This frequency domain data includes both in-plane and out-of-plane displacement.

In Figure 3.27(a) the direction of the transient excitation is clearly visible. The wave travels at a 45° angle across the plate. Two bands of energy are clearly visible. Equation (3.4) gives further information on propagation angle. The outer larger band being the A_0 mode and the smaller central band the S_0 mode. The steady-state excitation in comparison has the same bands but propagates in all directions, therefore forming circles. As well as this notable difference Figure 3.27 contains a third band of energy. This aligns with the expected wavenumber value for the fundamental shear-horizontal mode, SH_0. The transducer used in this application is not expected to generate strong SH_0 mode waves due to its lack of in-plane motion. Therefore it is concluded that SH_0 mode is likely to have been generated by mode conversions occurring at the boundary of the plate as Lamb waves are reflected back [14]. While this causes no issue in the measurements used in this chapter where out-of-plane displacement was isolated, in-plane data may be harder to exclude when performing measurements on complex geometries. If wide filter bands were to be used in this scenario they would likely include other modes at this thickness frequency product. The same data as shown in Figure 3.13 (a) were reprocessed using the same flattop filter with a bandpass width of $k_{pass} = 200m^{-1}$. In-plane data were however included alongside the out-of-plane data. These results are shown in Figure 3.28 (a). Figure 3.28 (b) shows the same data as in (a) but processing using a narrower filter bandpass width of $k_{pass} = 140m^{-1}$.

When including in-plane data the results show much greater level of inaccuracy when estimating thickness. This is likely caused by the inclusion of the SH_0 mode.

As it is non-dispersive its wavenumber will change at a different rate with frequency compared to the A_0 mode and it will therefore distort the amount of energy in certain mode filters. Figure 3.28 (b) displays less inaccuracy in thickness estimates as the narrower filter bands will have little overlap with the SH_0 or S_0 mode.

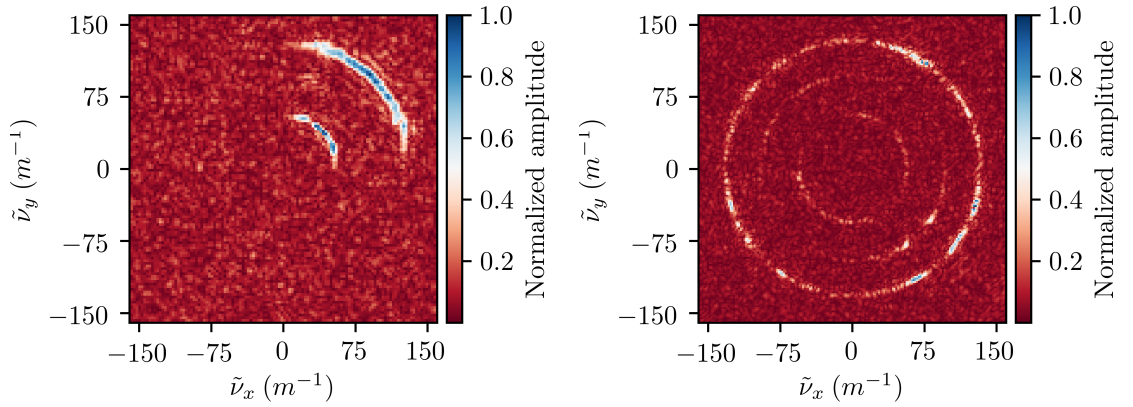

Figure 3.27: $U(\tilde{\nu}_x, \tilde{\nu}_y, f)$ of specimen 1 at $f = 300kHz$ with (a) transient excitation and (b) steady-state excitation.

The reduction bandpass width does however increase spatial error compared to the results shown in Figure 3.13 (a) which only include out-of-plane data.

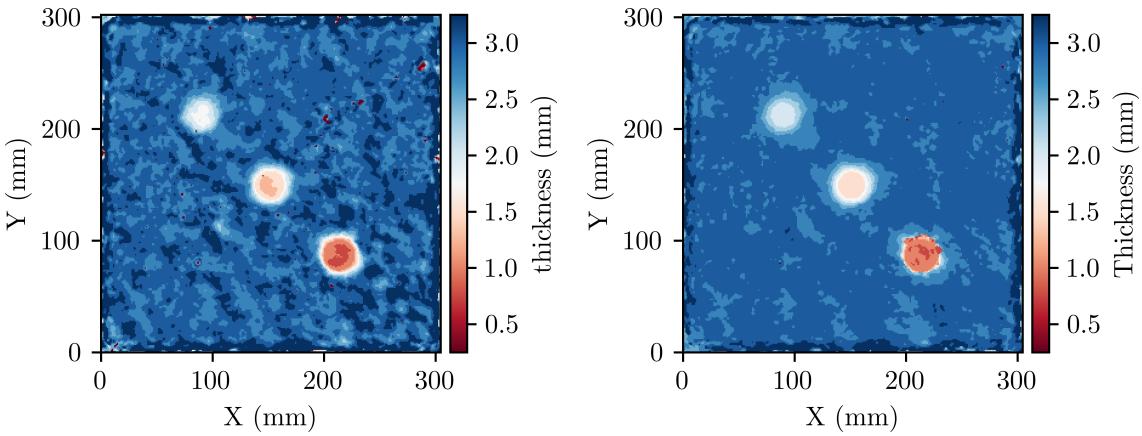

Figure 3.28: Specimen 1 data including in-plane and out-of-plane data filter with (a) $k_{pass} = 200m^{-1}$ and (b) $k_{pass} = 140m^{-1}$.

3.4.5 Local amplitude imaging

The implementation of monogenic signal analysis to allow the filter which removed the least amount of energy to be identified was also applied to the wavefield data before filtering. By applying Equation (2.30) before filtering it is therefore also possible to generate an amplitude map. This is analogous to imaging techniques

such as RMS imaging where the RMS of a wavefield is found to image defects. Figure 3.29 show the local amplitude map of specimen 2 at all single frequency excitations. These maps were determined by calculating the local amplitude of the wavefield at each time sample and then averaging them in the time domain.

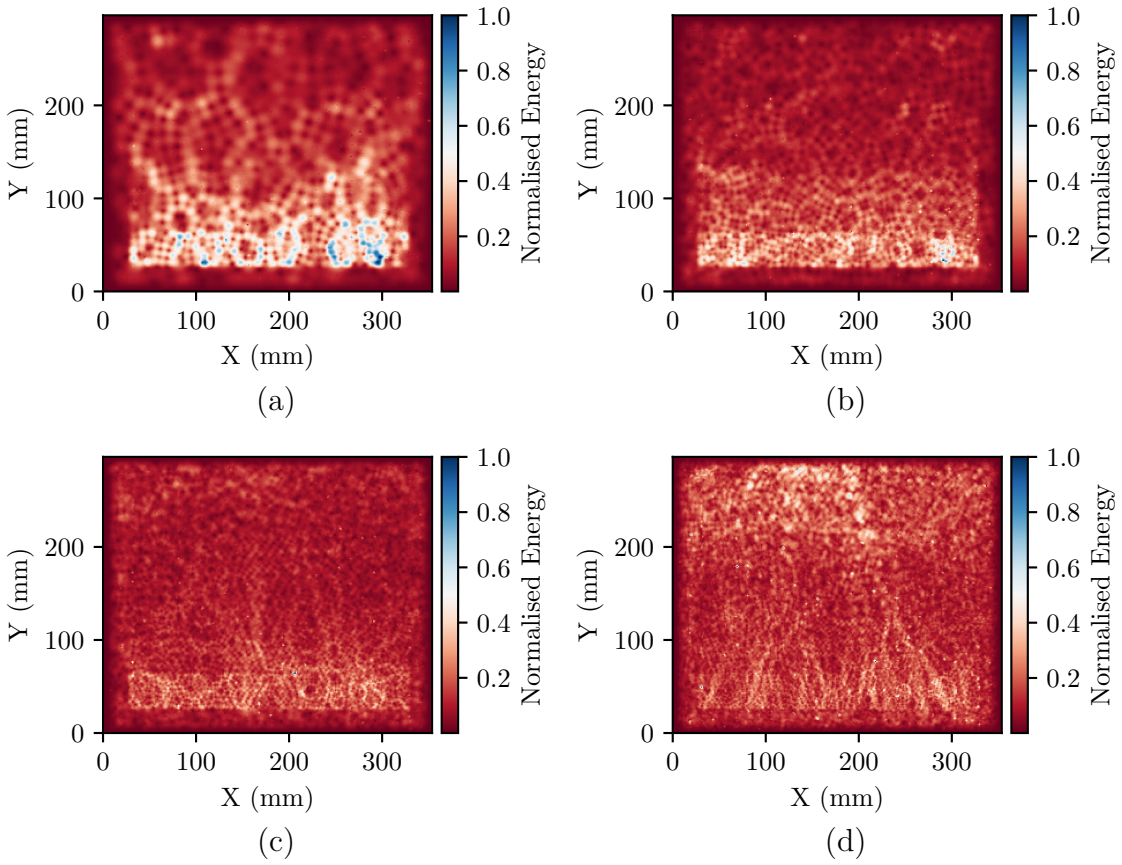

Figure 3.29: Specimen 2 local amplitude with single frequency steady-state excitation at (a) 75kHz, (b) 150kHz, (c) 300kHz and (d) 400kHz.

In areas of lower thickness higher amplitude is generally observed. In Figure 3.29 (d) this does not hold true and high levels of amplitude are shown around the transducer at $Y < 100mm$. As the higher frequency of $400kHz$ it is likely that a large amount of energy will attenuate close to the transducer resulting in this increased amplitude which does not relate to material thickness. It would not be possible to determine areas of damage or geometric part features using any of these excitation frequencies. The amplitude maps show amplitude features that are on the scale of the wavelength of the excitation signal. In all measurements, apart from the one shown in Figure 3.29 (d), it appears a good steady-state ultrasonic excitation was achieved. No clear areas of high amplitude are visible around the transducer. This allows some features to be identified. For example the step up to 8mm material thickness is visible around $Y = 280mm$. Figure 3.30 show the same results for specimen 2 using the $75kHz$ to $400kHz$ FM excitation. Results for both the Pancom and Pico-Z generated wavefields were determined.

When using FM excitation vastly different results are obtained. In both Figure 3.30 (a) and (b) a large proportion of geometric features are clearly identifiable. At a material thickness of $1mm$ thickness reductions down to $0.5mm$ are clearly resolvable. Even the thickness reduction with a $4mm$ diameter can be seen. At the same material thickness, thickness reductions of $0.1mm$ are however not at all resolvable. At greater material thickness all defects are visible but hard to identify. At $7mm$ material thickness all defects are barley visible and thickness steps are not identifiable at thicknesses greater than $4mm$. At low thicknesses this local amplitude approach clearly shows sharp stepped edges. For certain structures this clear definition of edges may be of use for identifying geometric features. As these results are easily obtained alongside WMS results local amplitude maps might offer additional useful information for damage detection purposes. The amplitude dependant nature of this technique does however limit it to materials in which a true steady state excitement can be generated. Furthermore only at low thicknesses were thickness changes clearly visible. The lack of quantitative data also limits the use of these results.

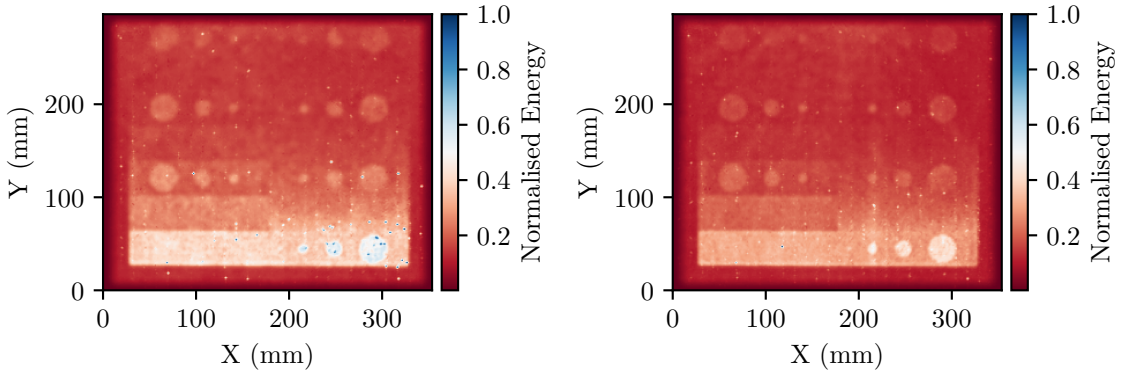

Figure 3.30: Specimen 2 amplitude with FM excitation generated by (a) Pancom and (b) Pico-Z transducers.

3.5 Conclusions

A new technique of WMS was proposed. This was achieved by calculating mode based filters and applying them to wave-field data generated with FM excitation. WMS to gain thickness maps was performed on two specimen plates with a large thickness range from 0.5mm to 8mm with single and FM excitation. Single frequency excitation was able to identify defects at low thicknesses but unable to cover the broad thickness range presented. Clarity of features and edges was further increased by using FM excitation along WMS. Multi-frequency data gained from FM excitation gave a thickness map with lower noise and ability to identify defects

across the whole thickness range with a single LDV measurement. The importance of filter bandpass size and shape was shown. Local amplitude mapping was also shown as being able to identify certain defects with high spatial resolution. While this technique has many limitations it might help to offer clear identification of certain features in thin structures. This work was completed on isotropic materials. The primary aim is to expand the technique to non-isotropic composite materials in the future. While theoretical methods of solving dispersion curves are available for composites their lack of accuracy and the detailed knowledge of layup required create further challenges to this expansion. While only demonstrated on a flat plate the application of a 3D scanning laser vibometer was successfully shown, giving the ability to also further this technique to more complex part geometries.

4. Composite dispersion characterisation

4.1 Introduction

To be able to expand WMS to composite materials a number of challenges must first be addressed. While it would be possible to expand the method described in Chapter 3.1 to composites by determining theoretical dispersion curves for composites this would not be a practical solution. Using methods such as TMM or GMM it is possible to determine the dispersion characteristics of a multi-layered composite [18, 89], but detailed knowledge of the material and layup must be known. Theoretical methods require a stiffness matrix of the entire composite layup, which would need to be determined experimentally for each layup. Alternatively composites can be modeled with a stiffness matrix for each layer. While this offers benefits in terms of being able to model composites with different layups and fibre orientation this quickly generates a large matrix that becomes challenging to solve [18].

Changes to characteristics such as fibre content percentage will affect the strength and stiffness of the composite, thereby changing the dispersion characteristics of a Lamb wave in the material. Variations like this are not only foreseeable but very likely in many composite manufacturing processes. Any other imperfections or variations during the manufacturing stage would have a similar effect. Furthermore, for composites in service it may be hard to obtain detailed information about the exact layup that was used in their construction. Even when detailed information is present over the lifetime of a composite structure everything ranging from repairs to reinforcement to different paint thickness could affect the dispersion characteristics. As such it can be seen that a NDT method that requires a deep understanding of the composite in a structure is not practical for most real world applications.

This chapter investigates the dispersion behaviour of Lamb waves in a range of carbon fibre composites. A particular interest is placed in the overlap and dispersion behaviour of modes. As the WMS concept relies on the ability to differentiate between different modes in the frequency domain, overlap of modes would prevent this from being completed effectively. A further consideration is the dispersive nature

of the mode. The fundamental S_0 and A_0 tend to be dispersive at lower frequency thickness products but do not show strong dispersive behaviour at higher frequency thickness products. A clear understanding of this relationship is needed to allow mode filters to be calculated. This understanding of the behaviour of composites will help towards the ultimate goal of developing a method whereby no prior knowledge of the composite is required and steady-state multi-frequency wavefield data can be utilised by mode filtering for damage detection.

4.2 Experimental setup

4.2.1 Test specimens

Three composite plates were manufactured from 12 plies of pre-impregnated carbon fibre. Details of the specimens are given in Table 4.1.

Table 4.1: Specimen details.

Specimen	Material	Layup	Thickness
3	UD carbon	$[0°]_{12}$	2.88m
4	UD carbon	$[[0°/90°]_3]_s$	2.74mm
5	2/2 Twill carbon	$[[0°/90°]_3]_s$	3mm

The specimen plates were $400mm$ by $400mm$ in size. The scan areas for all samples is 288mm by 315mm with a resolution of 234 samples by 256 samples. This gave a sampling frequency of $812m^{-1}$. All samples were excited using two Vallen System VS900-M PZT transducers. These were placed at $x = -20mm$ and $y = 150mm$ and $x = 150mm$ and $y = -20m$. The transducer location in relation to the measurement area is shown in 4.1.

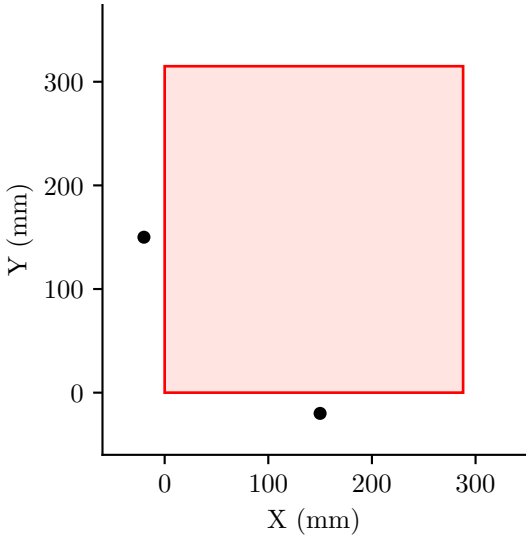

Figure 4.1: Specimen 3, 4 and 5, transducer location (black) and measurement area (red).

These placements were chosen to drive waves in both down the length of the specimen as well as across the specimen in the measurement area. The composite specimens considered in this chapter showed high attenuation of waves that were not traveling in the direction of the fibres in the specimen. This ensured there would be information about dispersion at least 0° to 90° propagation angles. The symmetry of the material means that no further angles of propagation were required. The transducers were driven with a continuous 200Vpp signal varying from 150kHz to 350kHz at a rate of 2.6kHz. The same driving circuit and 3D SLDV measurement setup as used in Chapter 3.1 was employed to capture in-plane and out-of-plane data.

4.3 Results and Discussion

The data taken from the 3D SLDV was interpolated in the two spatial axes using a cubic spline and a surface interpolation algorithm as described by Dierckx [81]. This was to ensure the even spacing of all spatial sample points. Both in-plane and out-of-plane velocity data were combined into a single wavefield by adding the velocity values in the spatial domain. The data were then windowed spatially using a Tukey window as given in Equation (3.1) with a shape value of $\alpha = 0.1$. The α value was chosen as it allowed for a minimum data loss while ensuring transient spikes at the edge of the measurement area were removed. In the temporal domain a 3^{rd} order Butterworth bandpass filter was applied between 100kHz and 600kHz to exclude any external noise [82]. The data were then zero buffered to a size of 512 samples in the spatial domain. Using a 3D FFT, as given in Equation (3.2),

the data were transformed from the spatial and temporal domain to the frequency domain.

Once the data had been transformed into the frequency domain in the form $U(\tilde{\nu}_x, \tilde{\nu}_y, f)$, it could be sliced in a number of axes to show the wavenumber-frequency relationship at different dispersion angles as well as the wavenumber-wavenumber relationship at different frequencies.

It is also possible to obtain slowness curves, showing the phase velocity, c_p, at different angles of propagation. A slice of $U(\tilde{\nu}_x, \tilde{\nu}_y, f)$ was taken and converted into polar form, $U_p(\theta, \tilde{\nu})$. The relationship between wavenumber components and dispersion angle is given in Equation (5.2). The phase velocity of each sample $U(\theta, \tilde{\nu}, f)$ was determined using Equation (2.16) and assigned the energy of that point. This converted the data to the form $U_s(\theta, c_p)$.

4.3.1 Specimen 3

For specimen 3 the 0° fibre direction was placed in the y direction. As such, waves traveling across the fibre direction corresponded to $\tilde{\nu}_x$. Figure 4.2 shows the wavenumber-wavenumber relationship of specimen 3 at a frequency of $250kHz$. To improve resolution of low amplitude features in the figure, all values that were greater than 50% of the maximum were taken to be 50% of the maximum. It was found throughout that this 'clipping' had no significant detail was lost at higher amplitude.

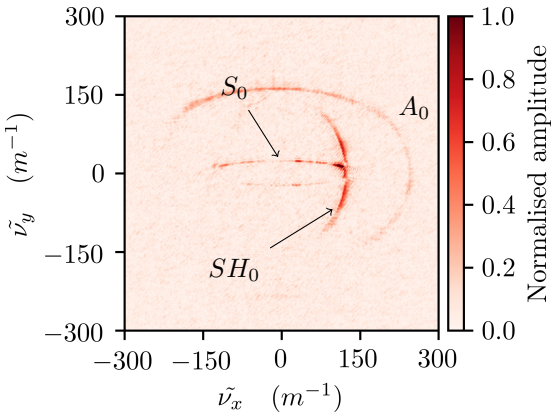

Figure 4.2: Specimen 3 $U(\tilde{\nu}_x, \tilde{\nu}_y, f)$ at $f = 250kHz$.

The three fundamental modes, S_0, A_0 and SH_0 are visible. The nature of the excitation means energy bands are clearest in the positive $\tilde{\nu}_x$ and $\tilde{\nu}_y$ region. The A_0 mode has the largest wavenumber showing slow propagation speed relative to the other modes. At $\tilde{\nu}_y = 0$ the A_0 mode is traveling at 90° to the fibre direction and has its largest wavenumber of $\tilde{\nu} = 245m^{-1}$. When traveling in the y direction the mode speeds up significantly with a wavenumber of $\tilde{\nu} = 162m^{-1}$. The SH_0

mode displays this same behaviour but to an even greater extent. In contrast to the A_0 and S_0 modes the particle motion of the SH_0 mode is perpendicular to the direction of propagation. As such the SH_0 mode travels faster in the x direction, perpendicular to the fibre direction. The wavenumber of the SH_0 mode varies from $\tilde{\nu} = 125m^{-1}$ to $\tilde{\nu} = 161m^{-1}$. This means that the SH_0 mode intersects with both the S_0 and the A_0 mode. The identification of the modes was based on work carried out by A. Gallina et al. and M. Kersemans et al. [89, 90]. Figure 4.3 shows the phase velocity, c_p, at the same frequency of $250kHz$.

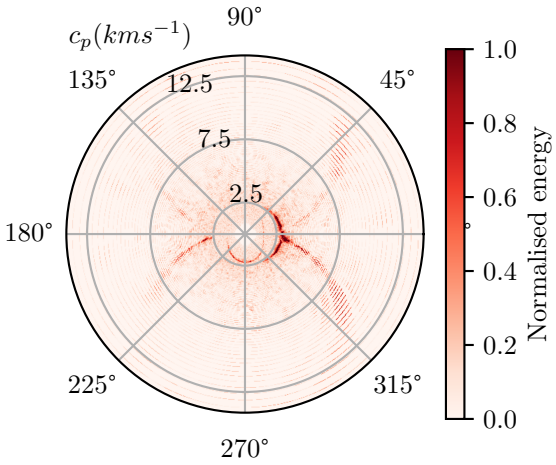

Figure 4.3: Specimen 3 $U(\theta, c_p)$ at $f = 250kHz$.

While the S_0 mode is challenging to identify with the high phase velocities the A_0 and SH_0 modes can be clearly identified at the lower velocities of $2.5kms^{-1}$. Figure 4.4 shows the wavenumber frequency relationship of the sample at three angles of propagation.

The values of these results were again clipped at half of the maximum value. A key feature that can be identified from the A_0 mode, which has the highest wavenumber values, is the fact that its wavenumber-frequency relationship is linear in this frequency thickness range. This does not hold true for the S_0 mode which shows its dispersive nature the most clearly in Figure 4.4 (c). The A_0 mode does not only have different wavenumber values in different propagation angles but these are shown to change over the frequency range. This can be identified by changes in the gradient of the A_0 modes wavenumber-frequency relationship. It is also worth noting the wavenumber of the SH_0 mode varies from overlapping with the S_0 mode at a 0° propagation angle to overlapping with the A_0 mode at a 90° propagation angle. If a filtering technique were to be implemented using in-plane data this may cause some challenges as S_0 and SH_0 modes are not separable at certain angles of propagation. While this is also true for the A_0 mode it presents less of a challenge as the dominant out-of-plane motion of the A_0 mode can be separated from the in-plane motion of the S_0 and SH_0 modes.

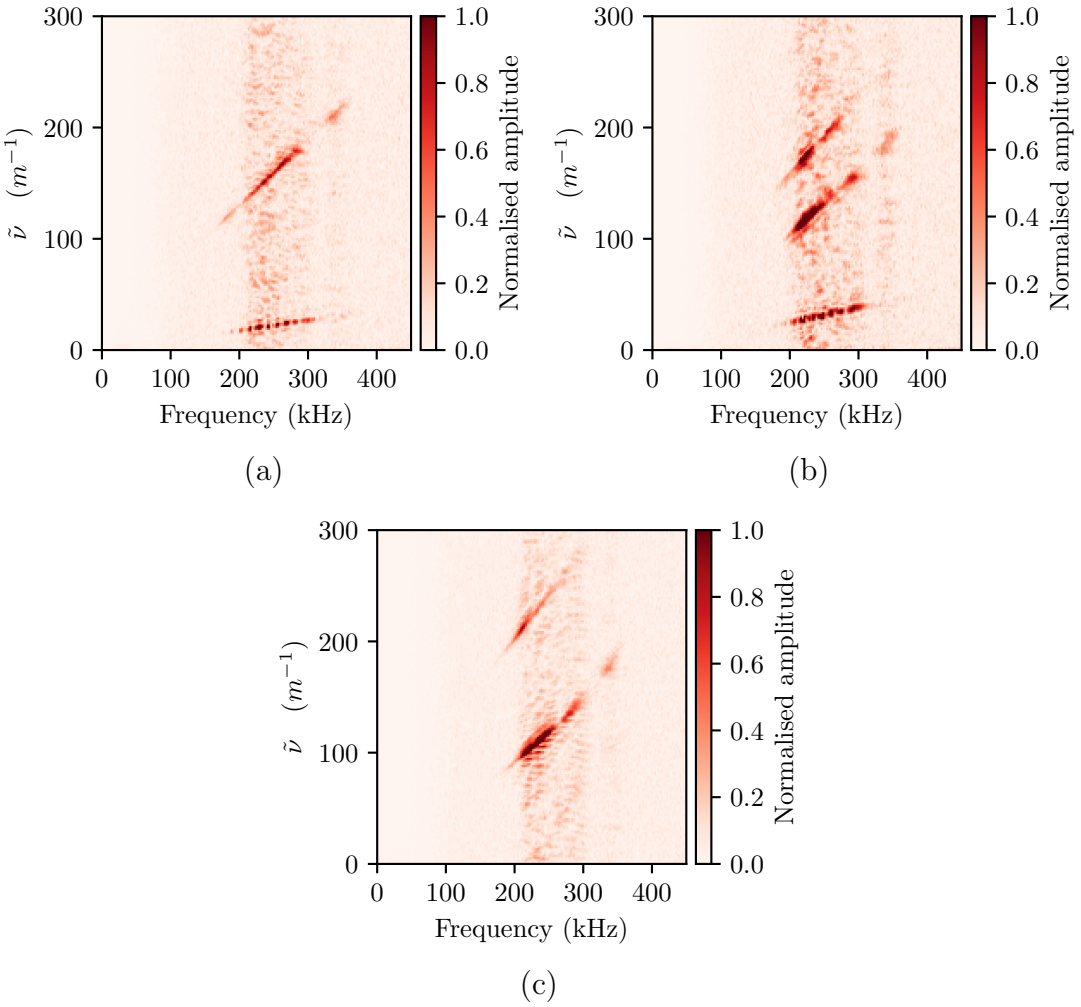

Figure 4.4: Specimen 3 $U(\tilde{\nu}, f)$ propagation angles of (a) 90°, (b) 45° and (a) 0°.

4.3.2 Specimen 4

Figure 4.5 shows the wavenumber-wavenumber relationship of specimen 4. Again the A_0 mode is the most easily identified but unlike in specimen 3 it is shown to maintain similar wavenumber values at all angels of propagation.

At a 45° angle of propagation the wavenumber is somewhat increased, indicating slightly reduced propagation speed when all fibres are being crossed at an angle by the wave. This is in line with the behaviour observed in specimen 3 where the mode had a much higher wavenumber value when traveling at right angles to the fibre direction. Despite the symmetry of the sample in the 0° and 90° angles the wavenumber of the A_0 mode is greater in the x direction than that of the y direction, decreasing form $\tilde{\nu} = 190m^{-1}$ to $\tilde{\nu} = 200m^{-1}$. Lamb wave velocity is related to the stiffness of the structure it is traveling in [18, 91].

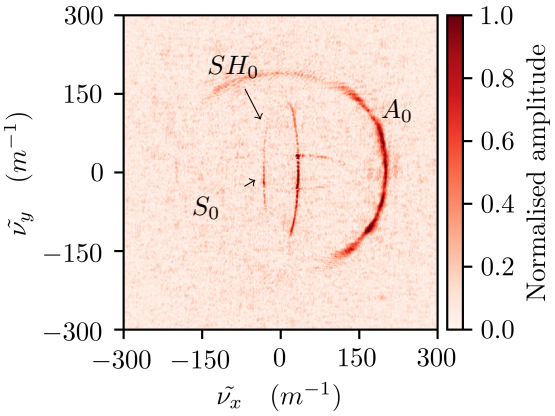

Figure 4.5: Specimen 4 $U(\tilde{\nu}_x, \tilde{\nu}_y,)$ at $f = 250kHz$.

Specimen 4 was constructed symmetrically with an even number of plies. As such the two internal plies are aligned in the same direction, as are the two outer most plies. The strong anisotropic mechanical properties of the UD plies result in a plate that is slightly greater bending stiffness in one axis then the other. This slight change in stiffness causes the measurable difference in wavenumber between the 0° and 90° propagation angles. The S_0 and SH_0 modes however are not affected and give the same behaviour in both the 0° and 90° propagation angles, which is expected for these modes [92]

The S_0 mode energy takes the form of a rectangle in the centre of Figure 4.5 ranging between wavenumber values of $\tilde{\nu} = 32m^{-1}$ and $\tilde{\nu} = 45m^{-1}$. Its wavenumber is the lowest at right angles where the wave is traveling along either the 0° or 90° direction. The SH_0 mode can also be identified and shows the greatest variability with relationship to propagation direction. Its wavenumber varies between that of the S_0 mode and the A_0 mode. Once again there is overlap between the S_0 and the SH_0 mode making it challenging to distinguish between the two separate modes.

This can also be seen when showing the same data in terms of phase velocity as in Figure 4.6. The mode shapes are in line with those identified by A. Nandyala et al. [91]. The SH_0 mode undergoes the largest changes in phase velocity, varying between $7.5kms^{-1}$ at 45° propagation to $2.5kms^{-1}$ at 0°.

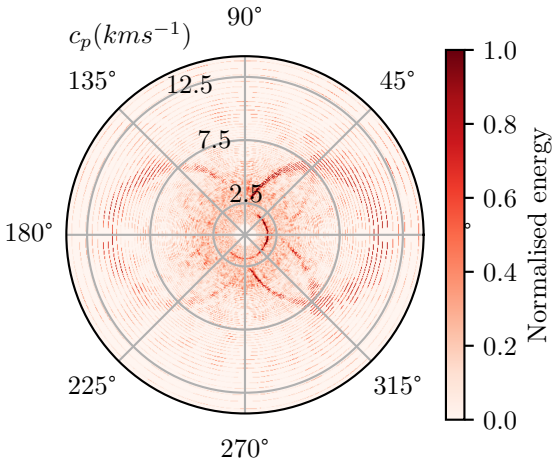

Figure 4.6: Specimen 4 $U(\theta, c_p)$ at $f = 250kHz$.

Figure 4.7 shows the wavenumber-frequency relationship of specimen 4 at three different propagation angles.

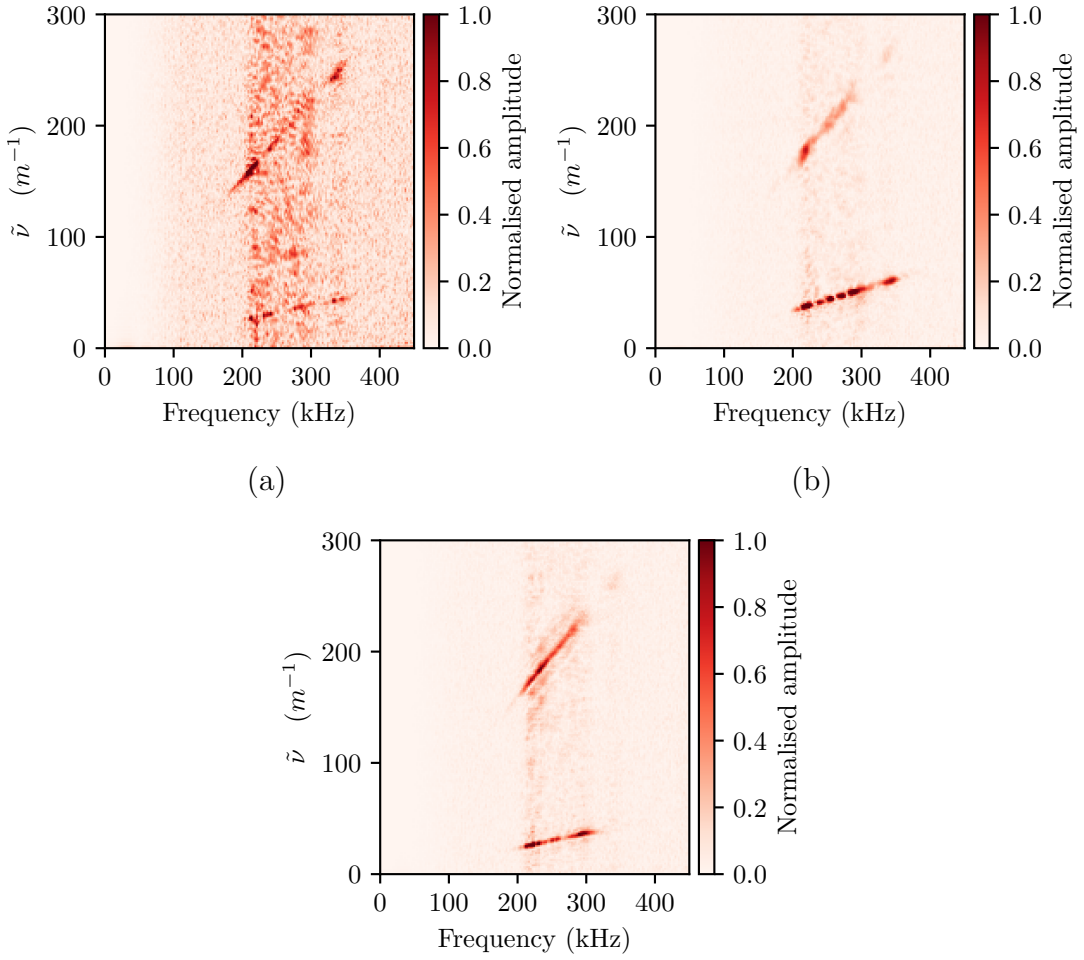

Figure 4.7: Specimen 4 $U(\tilde{\nu}), f$ propagation angles of (a) 90°, (b) 45° and (c) 0°.

While the A_0 mode appeared mostly quasi-isotropic in the wavenumber-

wavenumber domain a slight increase in wavenumber is visible at a propagation angle of 45°. The wavenumber-frequency relationship is again linear within this frequency thickness range. The gradient of the relationship also changes less over different angles in comparison to specimen 3.

4.3.3 Specimen 5

The wavenumber-wavenumber domain relationship at a frequency of $f = 250kHz$ is shown in Figure 4.8. The relationship appears very similar to that of the specimen 4. While specimen 5 consists of a twill weave and specimen 4 of Unidirectional (UD) material they both have approximately the same quantity of fibres running in each axis.

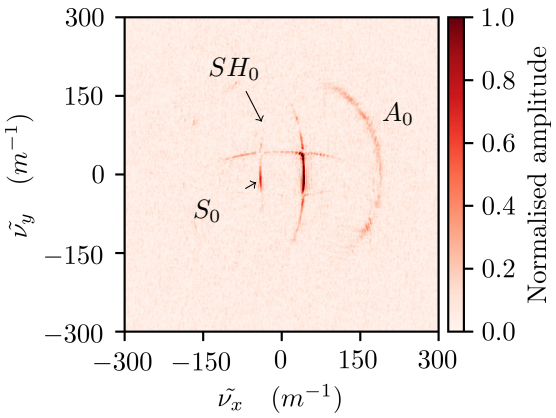

Figure 4.8: Specimen 5 $U(\tilde{\nu}_x, \tilde{\nu}_y, f)$ at (a) $f = 250kHz$.

The similarity is also given in the wavenumber values. At a propagation angle of 0° and 90° the wavelength of the A_0 mode is $\tilde{\nu} = 190m^{-1}$. This is the same value as specimen 4 had for the A_0 mode in the 90° direction. The S_0 mode is however slower with a larger wavenumber observed in specimen 3.

Figure 4.9 shows the phase velocity at the same frequency of $f = 250kHz$. As above these results are very similar to those of specimen 4. Notable differences are the reduction of maximum S_0 and SH_0 phase velocities. The maximum SH_0 velocity reduces from $10kms^{-1}$ to $8kms^{-1}$. The S_0 mode has its maximum velocity reduced from $7.5kms^{-1}$ to $6kms^{-1}$. The varying pattern of the SH_0 mode is more clearly visible. At an angle of 180° a band of energy can be seen around $c_p = 8kms^{-1}$, reducing to $c_p = 7kms^{-1}$ at 225°.

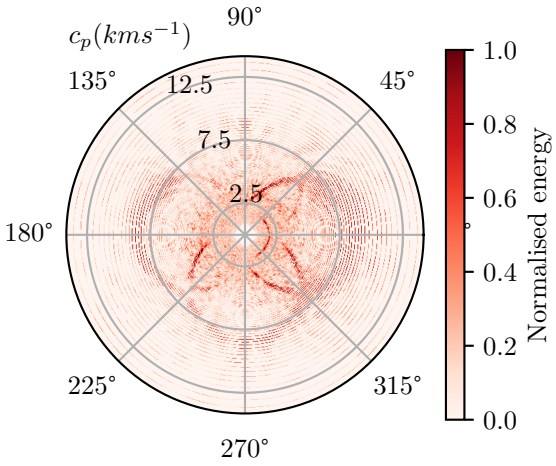

Figure 4.9: Specimen 5 $U(\tilde{\nu}_x, \tilde{\nu}_y, f)$ at (a) $f = 250kHz$.

The wavenumber-frequency relationship of specimen 5 is given at 0°, 45° and 90° proportion angles in Figure 4.10. At the 90° propagation angle the in-plane S_0 mode is the only visible mode. The low energy propagating in that direction gives high levels of noise preventing other modes from being identifiable. This is likely an artifact of poor sensor coupling of one of the sensors resulting in lower levels of energy being driven in the 90° direction. This measurement could not be repeated due to limited lab access during the Covid-19 pandemic. The material symmetry does however mean that the dispersion characteristics at the 90° angle should closely match those found at a 0° angle of propagation. At the propagation angle of 45° the S_0 mode coincides with the SH_0 mode. Despite clipping the amplitude values by half of the maximum, the high amplitude seen where the S_0 and SH_0 modes overlap results in only a faintly visible A_0 mode. High amplitude is also observed in the S_0 mode at a 0° propagation angle. Again the A_0 mode is visible at a wavenumber between $\tilde{\nu} = 150m^{-1}$ and $\tilde{\nu} = 200m^{-1}$. The high amplitude of S_0 mode is not in line with other measurements taken. It is likely to be the result of an error in the measurement taken by the SLDV. It is however possible to observe that the gradient of the A_0 mode does not undergo significant changes between the 45° and 0° propagation angles.

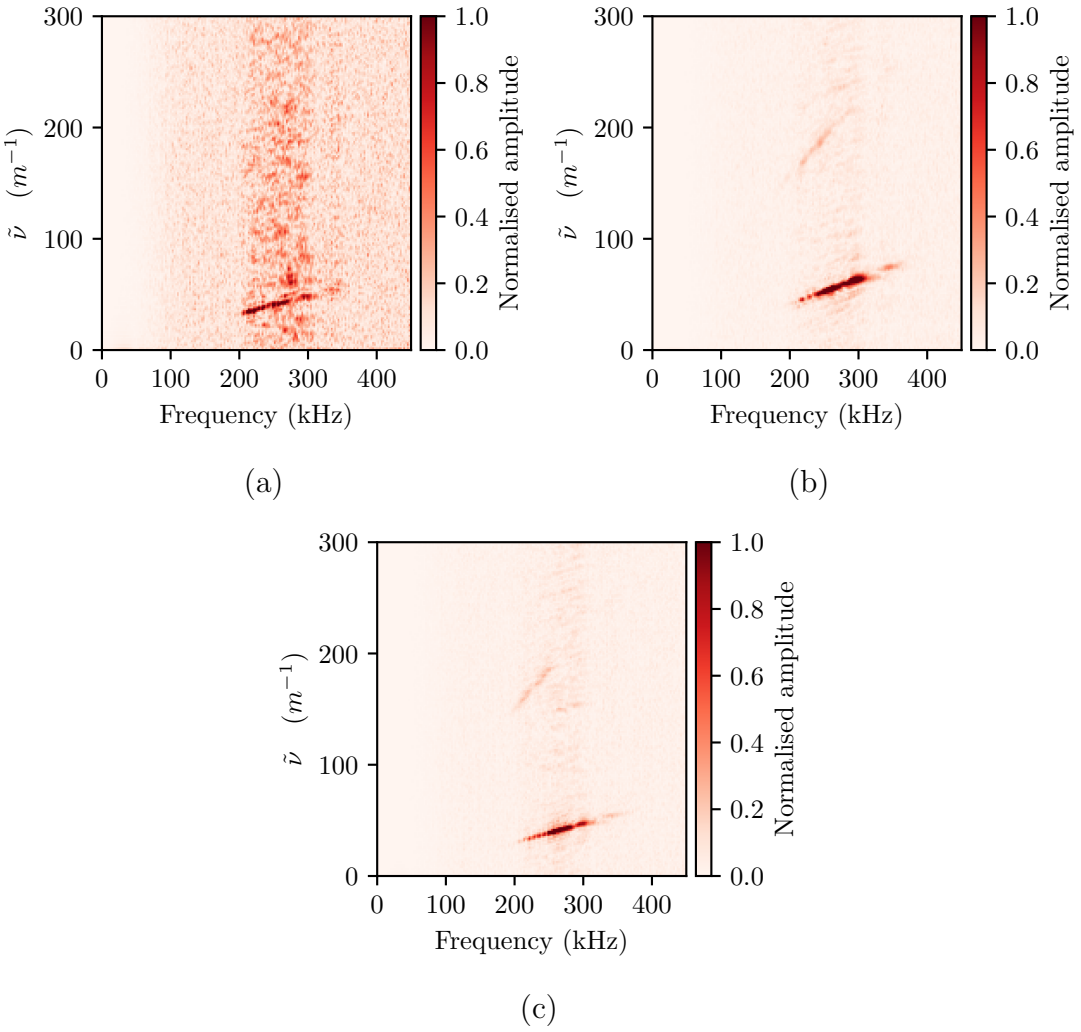

Figure 4.10: Specimen 5 $U(\tilde{\nu}, f)$ propagation angles of (a) 90°, (b) 45° and (c) 0°.

4.4 Conclusions

It was shown that the propagation and dispersion characteristics of Lamb waves in composites are highly dependant on the nature of the composite. Despite the high levels of variability the A_0 mode, which is of greatest interest, was least affected by changes in layup and fibre orientation.

Within the frequency thickness ranges investigated the A_0 mode showed overlap with the SH_0 mode. When considering only out-of-plane motion it would still be possible to minimise the energy of the SH_0 mode in the range of the A_0 mode, therefore allowing for effective mode separation. Challenges would however be faced if attempts were to be made to use the S_0 mode for wavenumber based defect identification in composites due to the overlap in the frequency domain between the S_0 and SH_0 modes. It was also clearly shown that assuming isotropic behaviour will cause serious errors when using wavenumber to detect damage. While the wavenumber of the A_0 mode does not vary greatly in composite weaves this is not the case in UD

materials. Even small changes in wavenumber for a given material thickness and frequency will cause errors, especially when considering the small changes observed in wavenumber with damage at larger material thicknesses. While the frequency wavenumber relationship was shown to vary between different angles of propagation the gradient of that relationship did not change by considerable amounts. This would allow this characteristic to be used for mode based filtering. Through this work a deeper understanding of the wavenumber-wavenumber and wavenumber-frequency relationship of different materials was gained. The clearer knowledge of this behaviour in representative composite samples will allow wavemode filtering to be developed further for application on composite structures.

5. Wave mode spectroscopy on non-isotropic materials

5.1 Introduction

This chapter proposes a method to expand WMS to non-isotropic materials. Dispersion characteristics were identified from frequency-wavenumber domain data. Using this information, non-symmetric mode filters were calculated allowing the identification of defects and geometric features in non-isotropic plate structures. No previous work has been undertaken to mitigate the the non-isotropic behaviour of composites when performing any form of fullfield wavenumber analysis. This technique requires no prior knowledge of a material or features that affect its dispersion such as a composites layup. The same algorithm can be applied to isotropic materials, such as aluminium, and anisotropic materials, including composites such as carbon fibre or even composites such as GLARE. This offers a significant advantage to this technique when considering real world application. Furthermore it will allow WMS to be applied to existing structures where records of the layup of the composite are not available. Even if details of the layup are known, extensive testing would be required to fully determine the dispersion characteristics. Characterisation of dispersion in the wavenumber-wavenumber domain as proposed in this section could also be applied to existing wavenumber filtering techniques such as AWS. This would allow methods such as those proposed by Flynn et al. [12, 65, 78] to improve their performance in anisotropic composites. For the measurement of an inspection area a fullfield, multi-frequency, steady-state response was captured using a 3D SLDV. This follows the same measurement process used in the previous chapters. In the WMS technique proposed in Chapter 3.1 information about wave dispersion was gathered from Rayleigh-Lamb equations. For WMS to be expanded to unknown materials and composites with complex dispersion behaviour, information about the dispersion of the material was found in the wavenumber-frequency domain. Mode filters were then calculated using this information to which the frequency domain data were filtered. While this does not give a thickness map it allows the utilisation of steady-state multi-frequency data to create "filter number maps" where each filter

number represents a thickness. While analogous to a wavenumber map this method allows the integration of multi-frequency data into one result, without any prior knowledge of the material even when the material displays strongly non-isotropic behaviour, a significant advancement in this technique. Without knowledge of the dispersion characteristics determined in this method it would not be possible to use multi-frequency results to give a single map showing damage. The use of multiple energy sources was also utilised to improve signal to noise ratios of the entire surfaces of the structure. This is of particular importance when large stiffeners or stringers are attached to the structure as these can greatly reduce the amplitude of Lamb waves. The use of multiple energy sources has not previously been used in conjunction with wavenumber filtering. The first part of this work describes this new technique and demonstrates it on a highly non-isotropic and a quasi-isotropic structure with damage and varying geometric features.

5.2 Experimental setup

While only out-of-plane motion was utilised in this chapter the use of a 3D system allows for this technique to be expanded to three dimensional parts in the future. Equally this work could be completed using a 1D system. The measurements were performed with a Polytec PSV-500-3D-M. Measurements were taken with a temporal sampling frequency of 2.56MHz and a sample length of 1024 samples.

While the density of sampling points varied slightly between specimens, sampling frequency ranged between $600m^{-1}$ and $800m^{-1}$. The specimens were excited using a linearly FM sinusoidal signal ranging from 30kHz to 350kHz, being modulated at a rate of 2.6kHz. Vallen System VS900-M transducers were used to excite the specimens and were driven at 200Vpp. Depending on the sample either single or multiple transducers were used.

A consideration when selecting a frequency range was the increase in attenuation with increase in Lamb wave frequency [75]. Composites also display higher attenuation compared to metallic structures such as aluminium [75]. Therefore steady-state excitation was used, which is to say the signal was continually driven into the specimen. Large single thickness structures will not introduce many reflections, meaning energy will be prominent in one direction which can make identifying dispersion relationships for different angles of propagation challenging. Reflections will also be minimised if the material attenuates the wave before it reaches edges of the material. To introduce more angles of propagation, multiple transducers in different locations outside of the measurement area were employed. Multi-transducer setups were demonstrated using Vallen System VS900-M transducers excited by the same signal.

An average of 100 measurements were taken at each spatial sample point on the specimen. These were averaged to give a better signal to noise ratio. While a lower number of averages would have been able to produce results of similar quality and would have reduced the measurement time no efforts were made during this stage of the work to optimise the measurement speed. Three specimens were examined in this work to investigate a broad range of materials that display a range of dispersion behaviours from highly anisotropic to quasi-isotropic.

Specimen 6 was constructed from UD glass with all fibres aligned in the Y-axis. While this is not a layup likely found in many real world applications it demonstrates an extreme, giving a highly anisotropic material. Specimen 6 was vacuum infused and cured at room temperature. Specimen 7 consisted of a 2/2 twill weave carbon fibre and was chosen to demonstrate the type of near quasi-isotropic materials common in a broad application of composite structures. It was constructed from pre-impregnated carbon and cured in an autoclave under vacuum. Specimen 7 was also damaged by a 20J impact in the centre causing a delamination but without causing large visible damage to the face of the plate.

Specimen 8, made of GLARE, was selected as a material that offers particular challenges for conventional NDT techniques [49]. This specimen is a Fibre Metal Laminate (FML) and represents a class of materials on which no form of wavenumber filtering has been performed to date. This specimen was a panel removed from the fuselage of an Airbus A380. The skin was 3.1mm thick and stiffeners and stringers were attached to the rear side. In the measurement area the stringers where bonded and the stiffeners were both bonded and riveted. The specimen had a slight curvature over the measurement face. This was however small enough to have a negligible effect on the estimation of wavelength allowing the specimen to be treated as a flat surface. The GLARE laminate was constructed of alternating layers of aluminum and Glass Fibre Reinforced Polymer (GFRP). A diagram of the cross section is shown in Figure 5.1. Details of the specimens are given in 5.1.

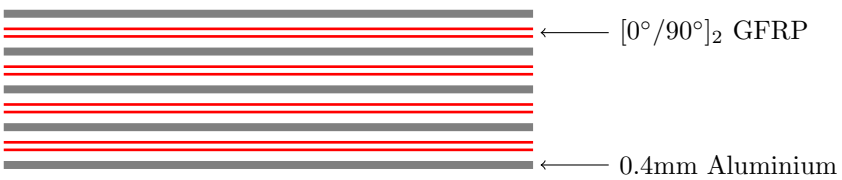

Figure 5.1: Specimen 7, GLARE, cross section.

The measurement area for specimen 6 was 372mm by 398mm. Specimen 6 was driven by two Vallen transducers placed at $X = -10mm$ and $Y = 410mm$ and $X = 350$ and $Y = 410mm$. Specimen 7 had a measurement area of 255mm by 255mm and was driven by three transducers. These were located at $X = 110mm$ $Y = 260mm$, $X = -10mm$ $Y = 260mm$ and $X = -10mm$ $Y = 130mm$. The

relationship between the measurement area and transducer location for specimen 6 and 7 is shown in Figure 5.2.

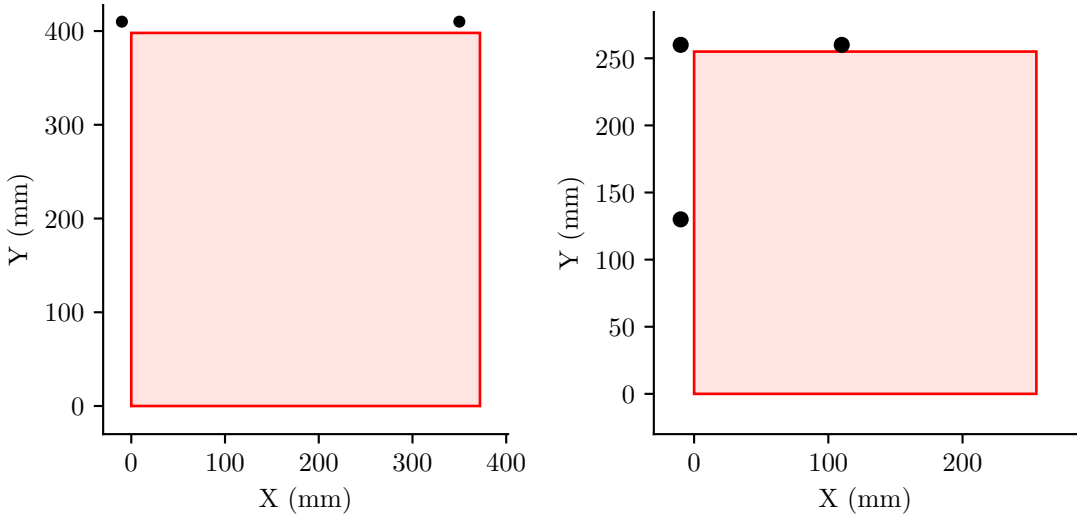

Figure 5.2: Specimen 6 (a) and 7 (b) measurement area (red) and transducer location (black).

Table 5.1: Specimen details.

Specimen	Material	Layup	Thickness
6	Fibre Glass UD	$[0°]_{14}$	2mm to 3.3mm
7	Carbon Fibre Twill	$[[0°/90°]_2]_s$	2.1mm
8	GLARE	4B	3.1mm

All transducers were clamped to the specimens using grease as a coupling agent. Both specimens 6 and 7 had overall dimensions of 400mm by 400mm.

Specimen 8 had a measurement area of 449mm by 380mm and was driven by a single Vallen transducer located at $X = 0mm$ and $Y = 400mm$. To further investigate the ability to detect defects specimen 8 had a number of pockets machined into its rear face. Post introduction of damage the measurement area of specimen 8 was $449mm$ by $408mm$ and shifted over the damage features. The transducer was located at $X = 50$ and $Y = 450$. Measurement area and transducer locations for pre and post damage setups of specimen 8 are shown in Figure 5.3

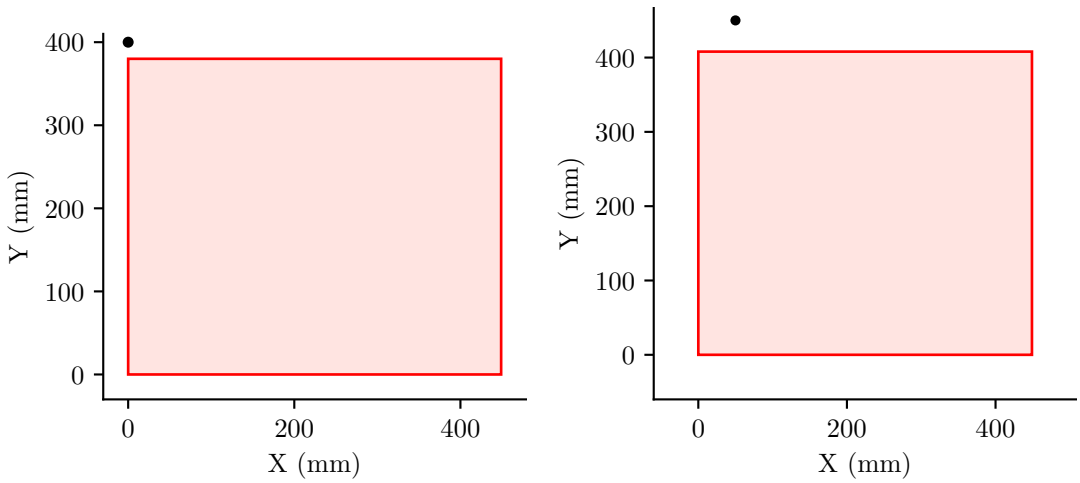

Figure 5.3: Specimen 8 measurement area (red) and transducer location (black) pre-damage (a) and post damage (b).

While an impact damage would be preferable, challenges surrounding verifying the depth and size of the damage make this a less practical option. As such small thickness reductions were machined into the rear face of the panel, allowing a clearer test of depth and spatial resolution. Figure 5.4 shows an image of the defects introduced to the rear face of the panel.

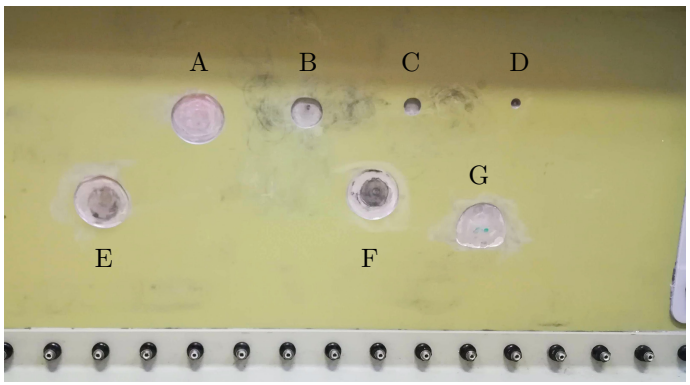

Figure 5.4: Rear face of specimen 8 showing thickness reductions.

Table 5.2 shows the dimensions of the thickness reductions.

5.3 Frequency domain mode filtering

To identify areas of different thicknesses the relationship between frequency, mode, and wavelength of Lamb waves is exploited. Using Rayleigh-Lamb equations theoretical dispersion curves can be calculated for a given material and thickness. Using

these results a theoretical mode filter can be determined in the temporal and spatial frequency domain for a given material thickness. The filter is then applied to measurement data obtained from multi-frequency excitation and used to determine the energy present at each material thickness.

Table 5.2: Dimensions of specimen 8 damage.

Defect	Maximum diameter	Depth
A	30mm	2.00mm
B	19mm	1.88mm
C	10mm	1.88mm
D	5mm	1.78mm
E	30mm	1.33mm
F	31mm	1.80mm
G	30mm	0.50mm

By repeating this process for a range of theoretical mode filters at different thicknesses it is possible to filter multi-frequency measurement data to a number of thicknesses, generating a thickness map. This technique is fully described in Chapter 3.1. For this technique dispersion characteristics of the material must be known.

This chapter focuses on extracting information of dispersion characteristics from the frequency domain data and creating mode filters accordingly, allowing this approach to be applied to non-isotropic materials with no prior knowledge of the material or its dispersion characteristics.

Spatial coordinates of each measurement point were used to re-sample the wavefield at each time point over an evenly spaced grid using a 2D cubic spline as in the analysis of Dierckx [81]. The velocity data from the vibrometer was placed into a 3D matrix with one temporal and two spatial axes, $u(x, y, t)$. Figure 5.5 shows the response, $u(x, y)$, of specimen 6 at time $t = 488.28ms$.

To identify dispersion characteristics of a material the multi-frequency measurement data were analysed in the wavenumber-frequency domain. A 3D FFT as given in Equation (3.2) was used to transform the measured velocity data, $u(x, y, t)$ into the wavenumber frequency domain, $U(k_x, k_y, \omega)$.

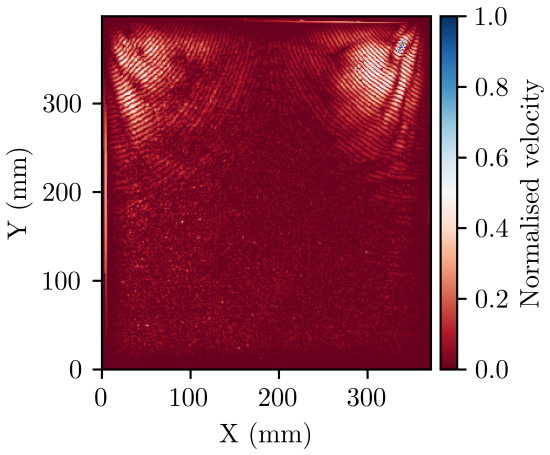

Figure 5.5: Specimen 6 normalised velocity , $u(x, y)$, at time $t = 488.28ms$ driven with two transducers.

5.3.1 Frequency-Wavenumber relationship

The dispersion characteristics of the material of the test specimens were identified in two distinct steps. The first was to identify the relationship between the temporal, ω, and spatial, k, frequency. In the frequency thickness ranges used in this work the fundamental anti-symmetric Lamb wave mode, A_0, can be assumed to have a linear wavenumber-frequency relationship [22, 89]. It is noted that this will not be true for all materials, material thicknesses or frequencies but can be used as a useful approximation for the common materials, frequencies and thicknesses used in this work. Figure 5.6 shows a theoretical dispersion curve calculated using DISPERSE [19] software. Dispersion curves were calculated for a 1mm thick fibre glass plate with all fibres aligned to 0°. Dispersion curves for the A_0 mode are shown for a 0° and 90° propagation direction. While there is a slight difference in slope of the linear region of the 90° curve compared with the 0° curve, this difference is low in comparison to the variability present when calculating this relationship from measured data where information is binned in the frequency domain. Figure 5.6 also serves to show the large variability in wavenumber for a material of uniform thickness, demonstrating the inability of wavenumber mapping or wavenumber spectroscopy to show areas of thinning in non-isotropic structures.

As such the relationship between frequency, ω, and wavenumber, k, can be described by a linear equation as shown in Equation (5.1) where m is the slope and c a constant for a given mode.

$$\omega = m * k_{pass} + c \tag{5.1}$$

To determine this relationship, the point of maximum energy in $U(k_x, k_y, \omega)$ was

located. The angle of propagation of that point was identified and the frequency-wavenumber relationship was extracted for that angle of propagation. Figure 5.7 shows the frequency-wavenumber data for specimen 6 at a 50° propagating angle.

The multi-frequency nature of the excitation means bands of energy corresponding to the fundamental symmetric, S_0, and anti-symmetric, A_0, Lamb wave modes can be identified. While in thin plate-like structures the band of energy will be a clear narrow band making it easy to identify the wavenumber frequency relation, in parts with larger thickness ranges this band of energy will be spread out due to the relationship between thickness, frequency and wavelength of a Lamb wave mode. This can be thought of as the result of many dispersion curves for a material at different thicknesses laid on top of each other. To reliably identify the relationship between frequency and wavenumber of the A_0 mode a Canny edge detection algorithm [93] with a standard deviation of $\sigma = 3$ was applied. While other algorithms would also be appropriate the Canny edge detection algorithm was chosen due to is success full application on similar image processing problems [93]. The σ value was chosen as it showed good sensitivity in this application.

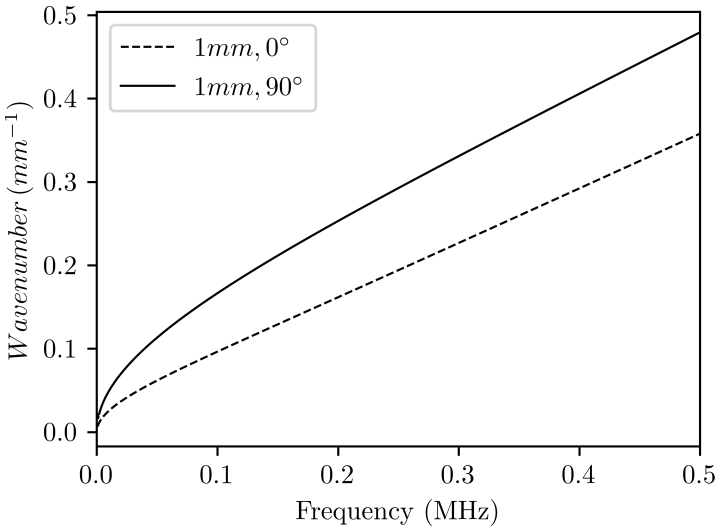

Figure 5.6: A_0 dispersion curve for 1mm thick UD fibre glass at 0° propagation along the fibre and 90° across the fibre.

As Canny edge detection is not amplitude dependant all values less than $\frac{1}{100}$ of the maximum value were assigned a value of 0 prior to performing edge detection. Once edges were detected a probabilistic Hough transform was used to find straight lines present in the detected edges as described by Matas et al. [94] and implemented with the OpenCV [95] software library. The results of the edge detection is shown in Figure 5.7 (a) along with the first five straight lines identified by the Hough transform. Criteria, such as minimum length can be tuned depending on factors such as the frequency range of the FM excitation used to improve reliability.

The dominant out-of-plane A_0 mode was reliably identified as the most prominent straight line. An equation was then found to describe the line giving a relationship between wavenumber and frequency. Figure 5.7 (b) shows the identified relationship in the form of a dashed line plotted on the original frequency domain data at a propagation angel of 50°.

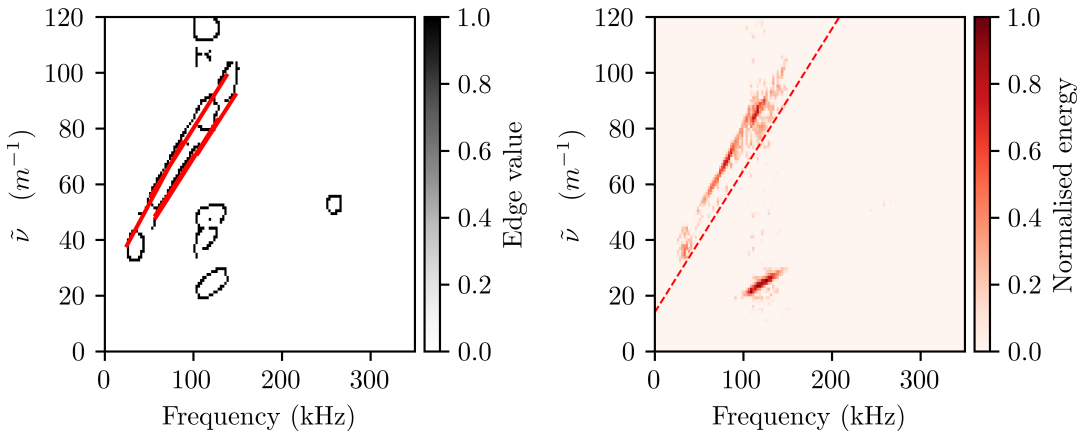

Figure 5.7: $U(\tilde{\nu}, f)$ at 50° propagation angle (a) detected edges and (b) detected frequency wavenumber relationship.

5.3.2 Wavenumber-Wavenumber relationship

A further complication with composite materials is that the group velocity of a Lamb wave varies depending on the direction of wave propagation in relation to fibre orientation for a given mode [21]. For example the A_0 mode will travel much slower perpendicular to the fibre direction compared to its velocity when traveling parallel to the fibre direction [21]. Figure 5.8 shows a slice of the frequency domain data at $f = 75kHz$ from specimen 6. Across the fibre, propagation is in the X direction, and along the fibre propagation is in the Y direction. Specimen 6 is highly non-isotropic with all fibers aligned in a single direction which corresponds to the Y axis. This difference in propagation velocities results in the wavenumber for the same thickness of plate being different depending on direction of propagation as is shown in Figure 5.8 (a). The angle of propagation, θ is given by Equation (5.2).

$$\theta = tan^{-1}\left(\frac{k_y}{k_x}\right) \tag{5.2}$$

As such a circular filter in the wavenumber-wavenumber domain will show changes in energy depending on dominant direction of wave propagation. Approximating composites with fairly even fibre distribution, such as specimen 7, to be isotropic can give good results. For non-isotropic material this distortion will

greatly limit depth resolution and distortion will be present and dependant on the positioning of the exciting transducer as well as wave reflections of geometric features.

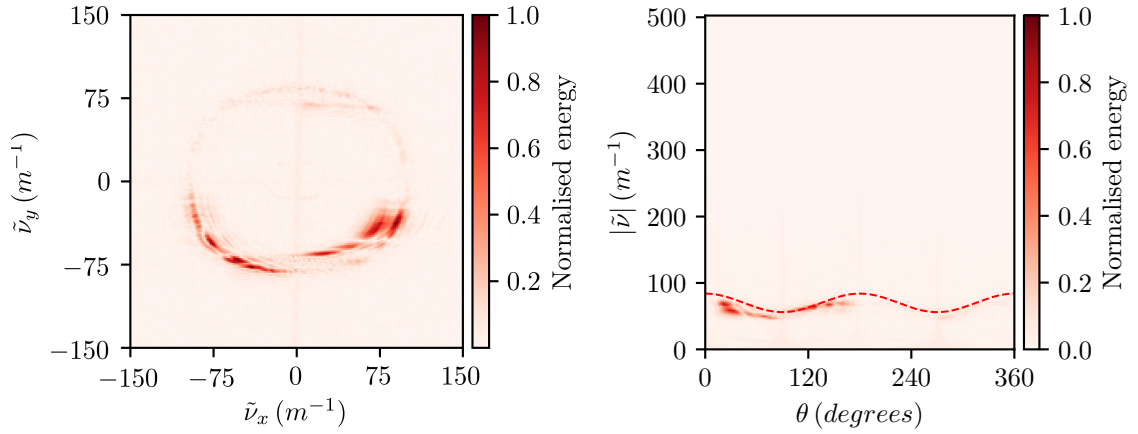

(a) (b)

Figure 5.8: $U(\tilde{\nu}_x, \tilde{\nu}_y, f)$ at $f = 75kHz$ (a) Cartesian form and (b) Polar form $U(\tilde{\nu}, \theta)$.

To account for this the wavenumber filter was calculated to be non-circular in the wavenumber-wavenumber domain, but a shape that best matches the shape of the wavenumber-wavenumber relationship at the dominant frequency. This relationship was described in terms of a sinusoidal waveform that matched the shape of dispersion at the dominant frequency in polar form as shown for specimen 6 in Figure 5.8(b). Equation (5.3) describes a sine wave with a number of parameters that can be adjusted to best match the data.

$$z(\theta) = -a * sin(q * \theta + \phi) + a \tag{5.3}$$

Where a is the amplitude, q is the wavenumber which was taken to be either 2 or 4 and the angle of propagation is θ, which ranged from 0 to 2π. The phase, ϕ, was taken to be either 0 or π allowing the peaks to either align with $0°/90°$ fibre direction or the $45°/-45°$ fibre direction. For more complex fibre orientations this may need to be extended. Two sets of shifting values, $z(\theta)$, were used to approximate the shape of the dispersion as given by Equation (5.4).

$$z_n(\theta) = z_1(\theta) + z_2(\theta) \tag{5.4}$$

For simplicity some general variables were defined as shown in Equation (5.5).

$$z_n(\theta) = [-a_1 * sin(q * \theta + \frac{\pi}{2}) + a_1] + [-a_2 * sin(q * \theta + \frac{\pi}{2}) + a_2] \tag{5.5}$$

Figure 5.8 (b) shows the polar form data along with the function $z(\theta)$ overlaid.

This value is then simply added to the bandpass centre, k_{pass}. The bandpass centre is dependant on the angle θ and is given by $z_n(\theta) + k_{pass}$.

5.3.3 Thickness mode filter calculation

The mode filter was calculated in the frequency domain and in the form $F(k_x, k_y, \omega)$. To calculate a mode filter for a thickness, represented by the c value in Equation (5.1), a frequency, ω, was first selected. The wave mode filter can be thought of as a stack of wavenumber-wavenumber domain filters. Using the relationship established in Equation (5.1) a value for wavenumber, k_{pass} was determined at a frequency. The wavenumber domain slice of the mode filter was calculated in polar form, $F_\omega(k, \theta)$, where the value k is given by Equation (3.3) and θ is the angle ranging from 0 to 2π.

For this work a flattop window was chosen but any windowing function, $w(n)$, can be applied. Equation (5.6) gives the bandpass centre for the polar form filter.

$$k(\theta) = k_{pass} + z_n(\theta) \tag{5.6}$$

As such a bandpass wavenumber filter was calculated using Equation (3.5). Figure 5.9 shows a slice of an example filter used for specimen 6 in both Cartesian, $F_\omega(k_x, k_y)$, and polar form, $F_\omega(k, \theta)$. For z_n, $q = 2$, $a_1 = 10$ and $a_2 = 2$. This process is then repeated for all values of ω to create a mode filter, $F(k_x, k_y, \omega)$.

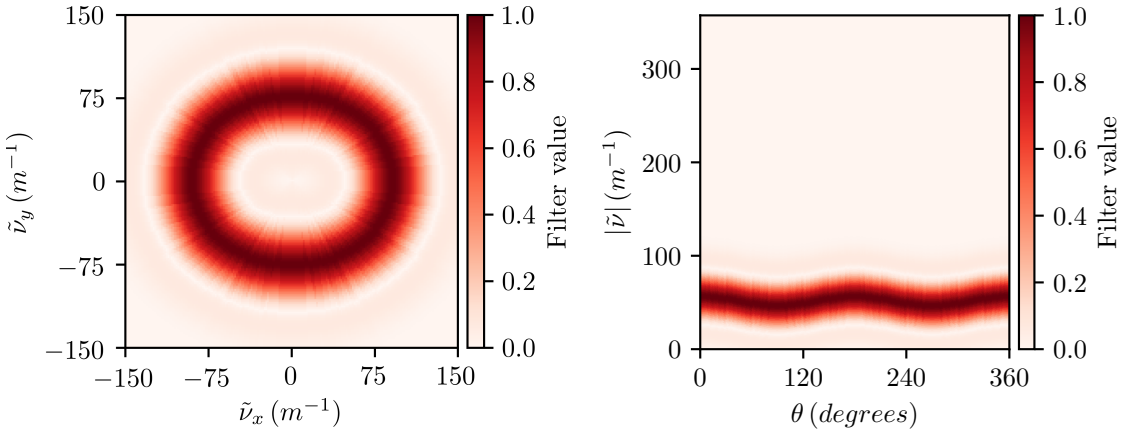

(a) (b)

Figure 5.9: $U(\tilde{\nu}_x, \tilde{\nu}_y, f)$ at $f = 75kHz$ (a) Cartesian form and (b) Polar form $U(\tilde{\nu}, \theta)$.

The changes in wavenumber for a given thickness change, at different angles of propagation are not constant for highly non-isotropic materials. Figure 5.10 shows the dispersion curves of the A_0 mode for 1mm and 1.2mm thick fibreglass plates as given by DISPERSE software. As an extreme example and to demonstrate highly anisotropic materials a [0°/0°] UD arrangement was chosen.

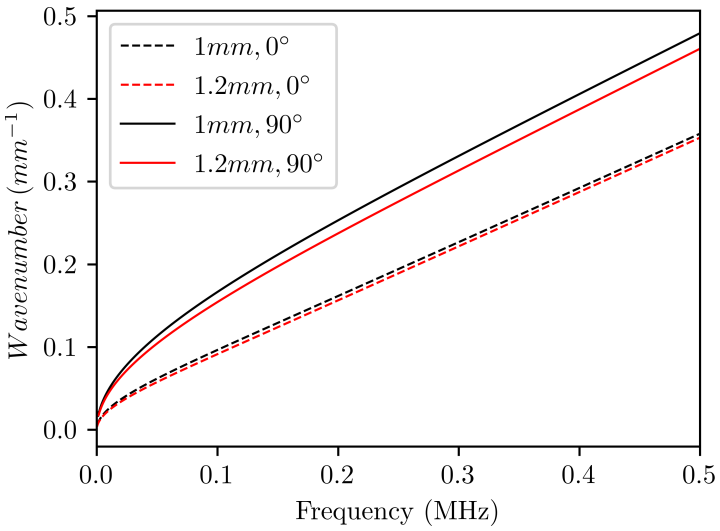

Figure 5.10: Dispersion curves for 1mm and 1.2mm thick UD fibre glass.

All fibres run in line with the 0° degree direction. While it is clear that the change in wavenumber due to a thickness change is not constant at different directions of propagation the error does not cause great issues. For this example a material thickness change of 0.2mm at a frequency of 100kHz causes a wavenumber change of $\tilde{\nu} = 14m^{-1}$ when propagating across the fibre and a change of $\tilde{\nu} = 4m^{-1}$ propagating along the fibre direction. This wavenumber difference of $\tilde{\nu} = 10m^{-1}$ represents approximately three frequency bins at a representative sampling frequency. It is also important to note that, had isotropic filters been used, there would have been a wavenumber difference of approximately $\tilde{\nu} = 59m^{-1}$ for the same frequency thickness at different dispersion angles making small thickness change impossible to resolve.

5.3.4 Mode filter application

Using different values of c in Equation (5.1) mode filters centred around different thickness were calculated. Initially a large range of values were used for c. An iterative process was then applied to give 15 values of c that covered the range of wavenumber-frequency values present in the measurement. The final 15 mode filters were multiplied with the frequency domain data and returned to the spatial domain as shown in Equation (5.7).

$$u_c(x, y, t; c) = \mathcal{F}_{3d}^{-1}[T(k_x, k_y, \omega; c)U(k_x, k_y, \omega)] \tag{5.7}$$

The Riesz transform [56], which is a higher dimensional extension of the Hilbert transform was used to find the monogenic signal after a mode filter had been applied. From the monogenic signal the local amplitude, A, at each time step can be found from the filtered spatial domain data giving $A(x, y, t, c)$. To determine the energy

that remains after a particular mode filter had been applied the amplitude data were summed in the time domain, t , as shown in Equation (5.8).

$$A(x, y, c) = \sum_{t} A(x, y, t, c) \tag{5.8}$$

Each spatial location (x, y) was then assigned the value of c which maximised A, thereby finding the mode filter that removed the least energy and best described the behaviour of the A_0 mode of the lamb wave at that point. As the values of c hold no inherent meaning they were substituted with integers ranging from 1 to 15, representing the filter number.

5.4 Results and Discussion

5.4.1 Specimen 6 results

Figure 5.11 shows the resulting filter number maps for specimen 6. Figure 5.11 (a) shows the results using an isotropic filter that is circular is the wavenumber-wavenumber domain. The wavenumber frequency relationship however follows that given in Section 5.3.1. In Figure 5.11 (b) the filters were distorted using values $q = 2, a_1 = 10$ and $a_2 = 2$.

While the filter number map does not give a unit of thickness it relates directly to it, noting this relationship is not linear. As such an area can only be identified as being thicker or thinner then another area. This relationship is inverse, so a larger number relates to a lower thickness. Using prior knowledge of the geometry it would then be possible to identify defective areas using this information.

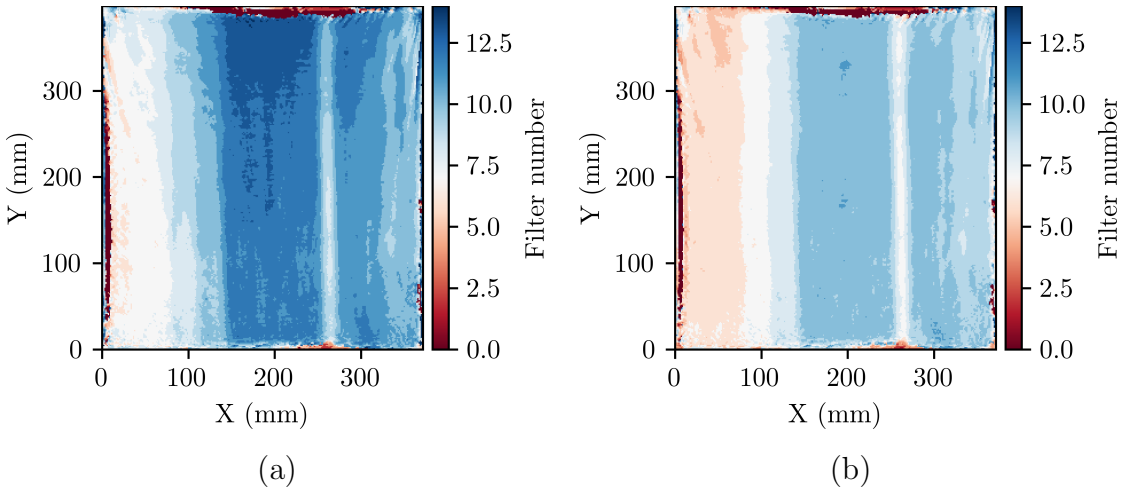

Figure 5.11: Specimen 6 filter number map (a) assuming isotropic and (b) with dispersion correction.

To further analyse these results Figure 5.12 shows the same results but with

known areas of differing ply numbers marked.

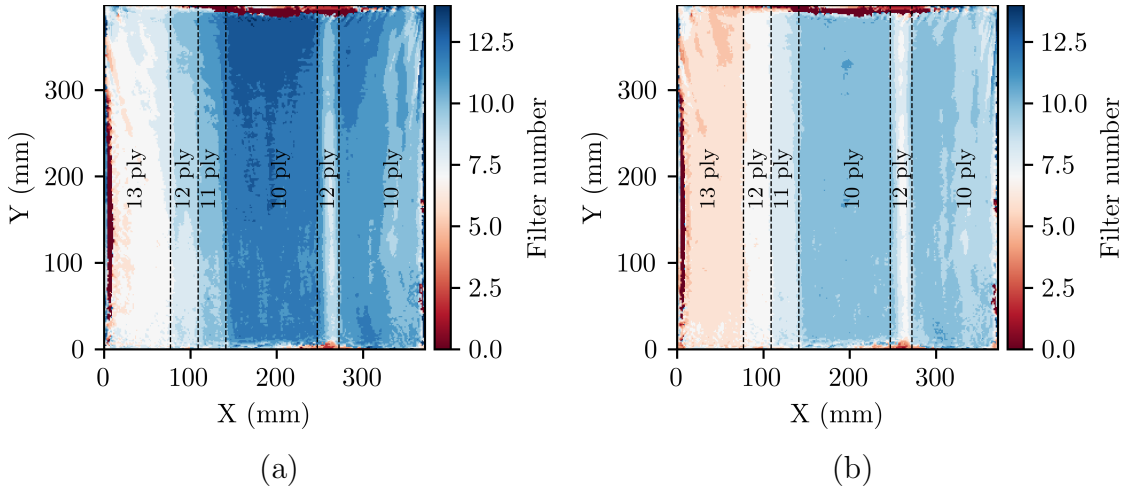

Figure 5.12: Specimen 7 annotated filter number map (a) assuming isotropic and (b) with dispersion correction.

Using the corrected wavenumber, filters areas containing the same number of plies are generally identified as being the same thickness. Single ply changes are clearly visible with defined edges. At $X = 280mm$ a fold was placed in one of the plies, thereby adding a thickness of two plies. This makes the area 12 plies thick and gives the same filter number as the area around $X = 100mm$ which is also 12 plies thick. In the region of $X > 300mm$ the thickness appears to increase despite there being no changes in ply thickness. While this may well be a measurement error it is also possible that it is a true geometric feature of the specimen. Through the vacuum infusion process it was noted that the specimen included imperfections such as indents where the infusion lines where pushed into the the dry cloth. A further investigation into thickness variation of the specimen was not possible due to restricted lab access during the Covid-19 Pandemic. A wide angle lens was used on the optics system of the 3D SLDV, causing barrel distortion. Sample points were placed in straight lines with this distortion resulting in pincushion distortion when measurement points were placed at their spatial position as determined by the 3D SLDV. This accounts for the lack of points on the edges which are assigned values of 0.

Assuming isotropic dispersion behaviour gave results with much greater distortion. The boundaries between ply thicknesses are not clearly defined. It is possible to generally identify thickness trends and features such as the fold and thickness increase. It would however not be possible to clearly identify delamination of lower plies which would cause small effective thickness changes. The large areas of the 12 ply and 13 ply thickness were assigned the same value. In the region of $Y = 250mm$ to $Y = 400mm$ this distortion is the most noticeable. The highest level of distortion would be expected where the dominant propagation angle differs to the rest of the

measurement area. Using monogenic signal analysis it is possible to map propagation direction as well as local amplitude. Using Equations (2.29), (2.27) and (2.28) the monogenic signal was found. Using Equation (2.30), where $l(x, y)$ is the IFFT of $L(k_x, k_y)$ it was then possible to map the signal envelope, or local amplitude, at each time sample t of the measurement matrix $u(x, y, t)$. The resulting amplitude matrix $a(x, y, t)$ was then averaged in the time domain to give the average amplitude matrix $a(x, y)$ which is shown in Figure 5.13 (a). Likewise the orientation of a multi-dimensional signal can be found from the monogenic signal using Equation (5.9) [83].

$$\theta(x, y) = arctan\left(\frac{l_{oy}(k_x, k_y)}{l_{ox}(k_x, k_y)}\right) \tag{5.9}$$

The values of l_{oy} and l_{ox} are the temporal domain representations of L_{oy} and L_{ox} given in Equation (2.27) and (2.28) As before the orientation was found at each time sample giving $\theta(x, y, t)$ and was then averaged in the time domain to leave $\theta(x, y)$ which is shown in Figure 5.13 (b).

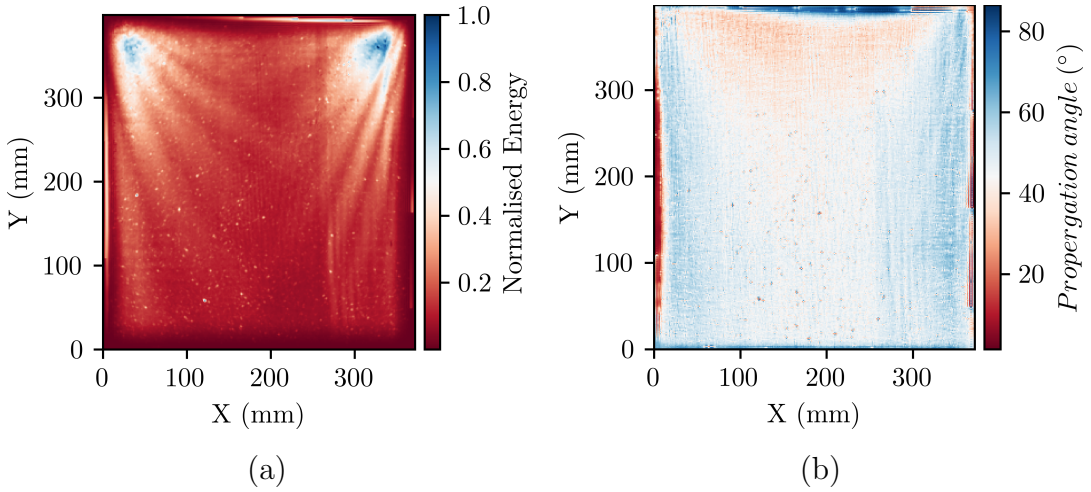

Figure 5.13: Specimen 6 (a) amplitude map $a(x, y)$ and (b) propagation angle map $\theta(x, y)$.

Propagation at 90° runs along the fibre in the Y direction. Due to the transducer location the angle of propagation is generally between 55° and 40°. The area with the greatest distortion in the results assuming isotropic propagation aligned with a region with a dominant proportion angle of 30° at $Y > 300mm$. As the wavenumber will be different for a given thickness and frequency at different angles it is likely that this high level of distortion was caused by the decrease in propagation angle. This underlines the need for for non-isotropic wavenumber filters when considering materials such as these under steady-state excitation. It also serves to show that the distortion would change depending on the location of the excitation sources. As steady-state excitation was used, reflections will be generated from edges, defects

and geometric features. As such it is important to note that Figure 5.13 (b) only gives the dominant propagation angle of the Lamb wave. Another features of interest is the increased angle of propagation visible in the fold at $X = 280mm$. It appears to show an increase in Lamb waves traveling down the fibre length in this section. The thickness decrease either side of the fold is likely to have internally reflected the Lamb wave.

Figure 5.13 (a), which shows the mean local amplitude, acts to demonstrate the increased attenuation experienced by Lamb waves in composite materials [75]. The ultrasonic energy is not spread evenly, but rather shows a number of more intense beams. The likely reason for this is the differing attenuation observed with fibre direction as described by Ono et. al. [75]. It may also in part be due to interference fringes generated when two wave sources are close to one another. The driving transducers were close to the edge of the specimen resulting in reflections off those surfaces. These could act as secondary sources causing constructive and destructive interference. The spread out nature of these sources and the high attenuation of the composite plate does make this less likely to be the dominant factor. While negative interference is not a desirable characteristic, difference in amplitude has been shown not to impact results in the previous chapter.

5.4.2 Specimen 7 results

Specimen 7, constructed from a carbon twill weave, demonstrated a sample with near quasi-isotropic dispersion behaviour. Figure 5.14 shows a snapshot at time $t = 156\mu s$ of the velocity in the specimen.

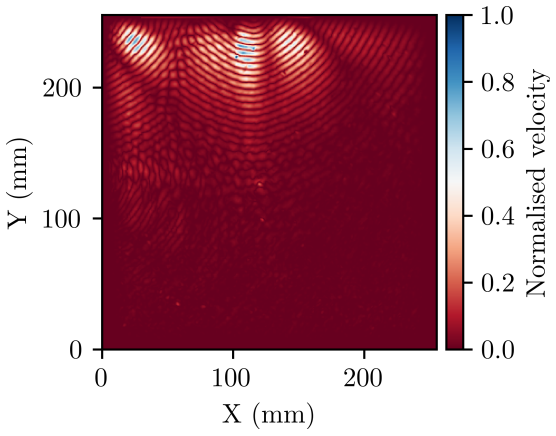

Figure 5.14: Specimen 7 normalised velocity , $u(x, y)$, at time $t = 156\mu s$ driven with two transducers.

All three transducers were being driven with the same signal, voltage and were of the the same type. Despite this the third transducer at $X = -10mm$ and $Y = 130mm$ produced lower amplitude. This could be due to a number of factors

but is likely due to variation in the transducer build or poor coupling with the specimen. As in all previous setups the transmitting transducers were clamped to the specimen with a thin layer of grease between the transducer face and specimen.

The near quasi-isotropic behaviour of this plate can be identified by the circular nature of the A_0 band in the wavenumber-wavenumber domain as shown in Figure 5.15 (a). In Figure 5.15 (b) the filter at the same frequency is shown. An optimal distortion was determined as follows: $q = 4, a_1 = -2$ and $a_2 = 2$.

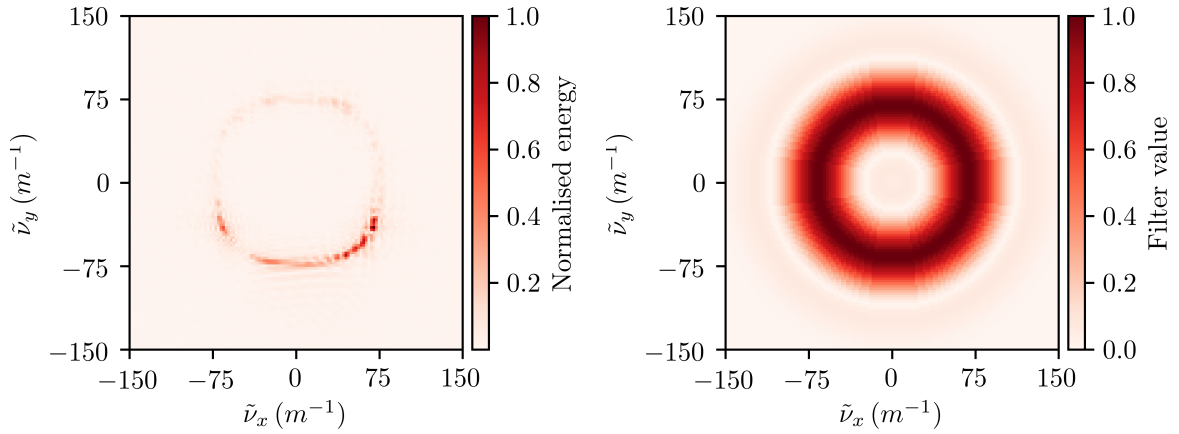

Figure 5.15: Specimen 7 (a) response $U(\tilde{\nu}_x, \tilde{\nu}_y, f)$ at $f = 75kHz$ b) filter $F(\tilde{\nu}_x, \tilde{\nu}_y, f)$ at $f = 75kHz$.

The results were found using both assuming isotropic dispersion as well as correct filters and are shown in Figure 5.16.

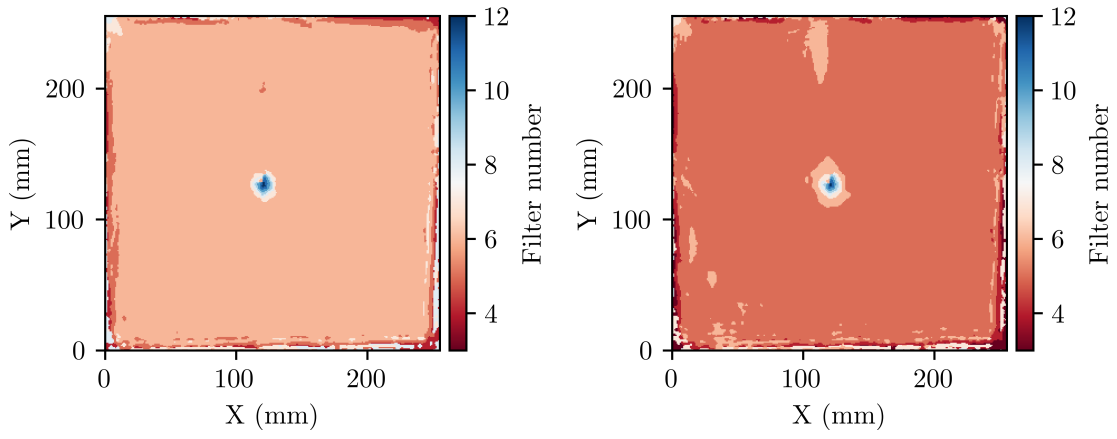

Figure 5.16: Specimen 7 filter number map (a) assuming isotropic and (b) with dispersion correction.

Both filters give similar results. This is to be expected with distortion correction values in $z(\theta)$ on the scale of two frequency bins in the frequency domain. The bulk of the area differs by one filter number between the results. While there appears

to be a difference in the results it is simply an artefact of the shift in the bandpass centre with $z(\theta)$. The corrected results shown in Figure 5.16 (b) do include some changes in filter number over the undamaged area, most notably around $X = 100mm$ and $Y = 220mm$. These are likely artefact of the quantisation of the filters and the increase in k_{pass} introduces by the correction in the wavenumber-wavenumber domain. Without further testing it is not possible to easily determine which filter gave more accurate results. It is however clear that when testing quasi-isotropic materials the difference in dispersion depending on propagation direction is minimal.

As before a map of local amplitude and dominant local orientation was calculated using Equation (2.30) and (5.9). The results are shown in Figure 5.17.

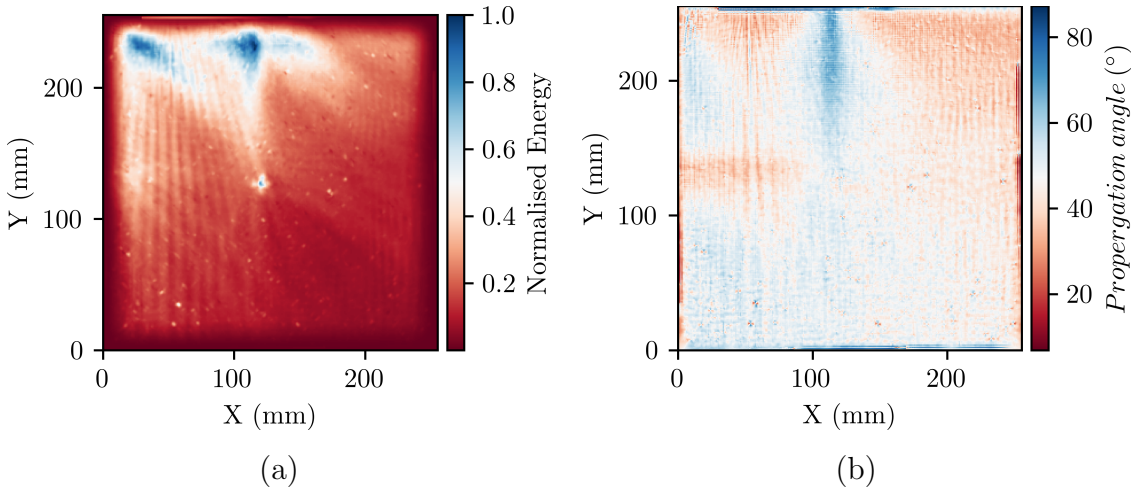

Figure 5.17: Specimen 7 (a) amplitude map $a(x, y)$ and (b) propagation angle map $\theta(x, y)$.

As was seen in Figure 5.14 the third transducer drove very little energy into the specimen. As the local orientation is amplitude independent, the signal being driven in by the third transducer is identifiable from a band of energy propagating in the 0° direction along the X axis.

While changes to the filter shape in the wavenumber-wavenumber domain did not have a great effect on the quality of the result the use of multi-frequency excitation enables the utilisation of the steady-state multi-frequency data. Without knowing the dispersion characteristics of the material this was not previously achievable. As a comparison the results were processed using wavenumber filtering for a single frequency taken from the multi-frequency excitation data. These results are analogous in their natures to those of previous work using AWS [64, 69, 78]. Figure 5.18 shows the single frequency results of four frequencies contained within the excitation range. These results were processed by applying the same filter stack to only one temporal frequency slice. As there is no other information outside of the frequency slice this is the same as wavenumber filtering rather than mode filter.

The best performing single frequency responses were at the lower frequencies of 60kHz and 120kHz. While the central delamination is still visible at 120kHz its prominence is reduced. At the two higher frequencies of 180kHz and 240kHz the defect is not clearly identifiable and is on the scale of noise furthest from the transducers. At these higher frequencies attenuation will be much higher resulting in lower signal to noise ratio. This is particularly visible in the lower parts of the plate in the region of $Y < 100mm$. This lack of energy caused noise in the measurements at the higher frequencies of 180kHz and 240kHz.

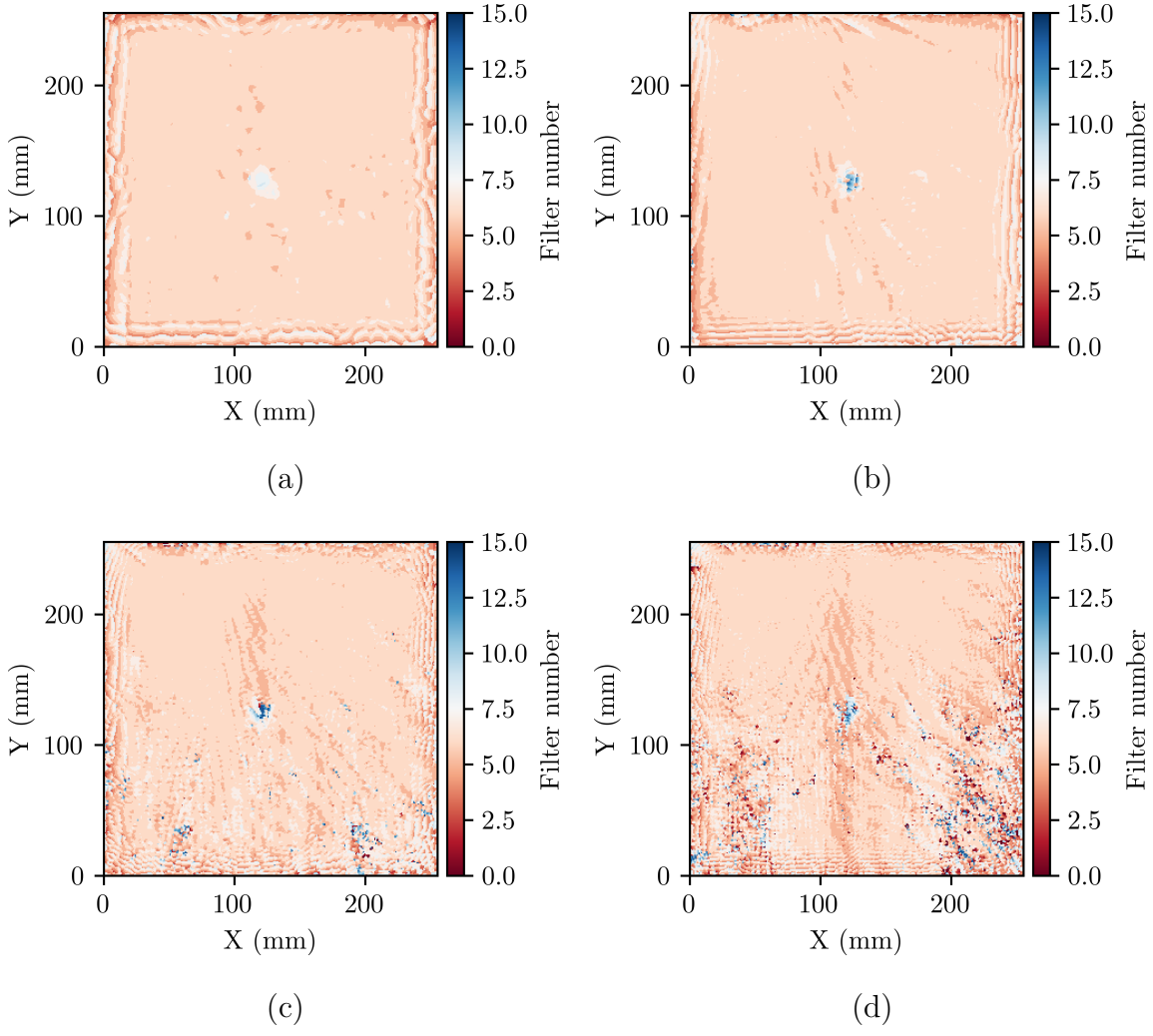

Figure 5.18: Specimen 7 single frequency results (a) 60kHz, (b) 120kHz, (c) 180kHz (d) 240kHz.

Figure 5.19 shows the mean frequency response for the area closer to the driving transducers, $Y > 225mm$, and the same area on the opposite side of the specimen at $Y < 30mm$. The frequency values were normalised to their peak to give a relative scale of attenuation of different frequencies in this setup.

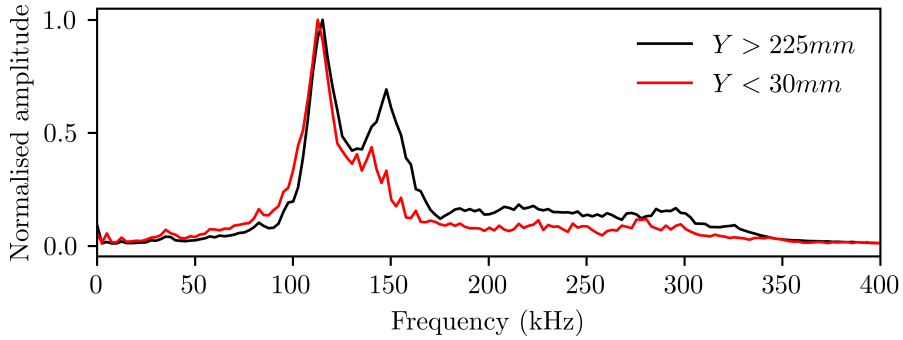

Figure 5.19: Mean frequency response.

The area further from the excitation source in the region of $Y < 30mm$ clearly shows less energy at higher frequencies. This is in line with what was observed in Figure 5.18. Furthermore the resonant behaviour of the transducer means there is relatively little energy at the lower frequency of 30kHz to 75kHz. The results at 60kHz, shown in Figure 5.18, gave a clearer view of the delamination than the result at 240kHz despite both frequencies having similarly low energy. Another key factor is the increase in wavelength compared to materials such as aluminum. Table 5.3 shows the wavelength of the A_0 mode at each single frequency as determined from the frequency domain data.

Table 5.3: Specimen 7 A_0 wavelength.

Frequency	Wavelength
60kHz	35.7mm
120kHz	21.7mm
180kHz	15.6mm
240kHz	12.2mm

A Lamb wave will interact more strongly with a defect that has a size on a similar scale to the wavelength of the Lamb wave. At $60kHz$ the wavelength is substantially longer than the size of the 25mm diameter delamination defect. While the higher frequencies are subject to higher levels of attenuation their wavelengths allow them to interact more strongly with the defect. This serves once again to demonstrate the benefit of multi-frequency excitation.

5.4.3 Specimen 8 results

Unlike the first two specimens, specimen 8 was manufactured from GLARE, a composite made up of a mix of isotropic and non-isotropic materials. Figure 5.20 shows

the frequency domain data, $U(\tilde{\nu}_x, \tilde{\nu}_y, f)$, sliced in the spatial and temporal frequency axes.

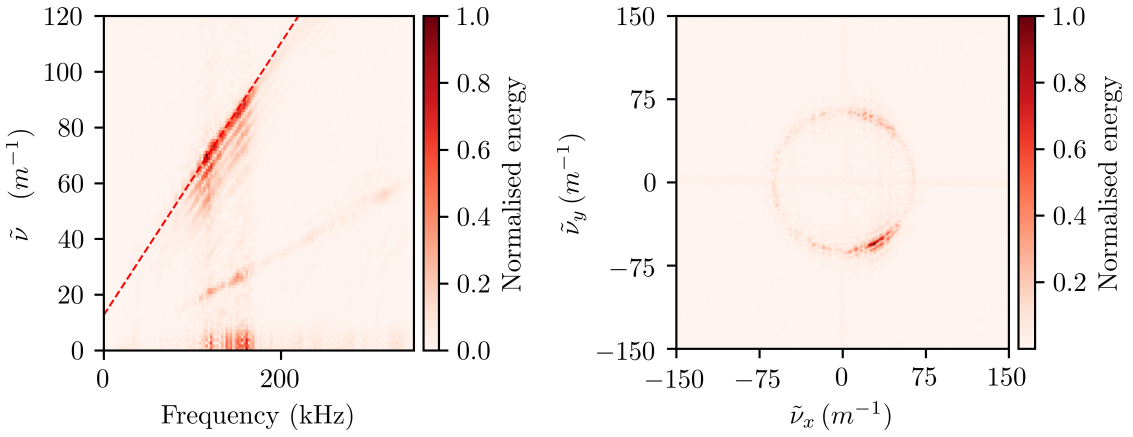

Figure 5.20: Specimen 8 frequency domain data $U(\tilde{\nu}_x, \tilde{\nu}_y, f)$ at (a) $\tilde{\nu}_y = 0$ and at (b) $f = 75kHz$.

The relationship shown in Figure 5.20 (b) shows the isotropic dispersion nature of the GLARE composite. As such no correction was undertaken in the wavenumber-wavenumber domain. The same process as previously was however applied to determine the wavenumber-frequency relationship. Once again this was completed without prior knowledge of the material. Figure 5.20 (a) shows the relationship overlaid with the frequency wavenumber data. The relationship is again confirmed as being very close to linear in this frequency thickness range. The fitted line also matches the gradient of the A_0 energy band very closely. Unlike the other specimens in this section, the A_0 energy band appears to have regular parallel bands despite the specimen mostly being a single thickness. Figure 5.21 shows a closer view of this area of the frequency domain data.

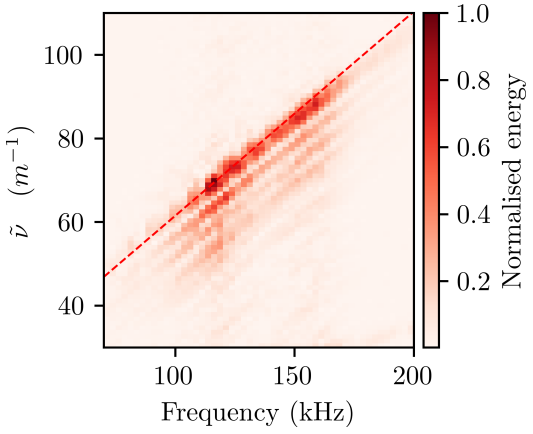

Figure 5.21: Specimen 8 frequency domain data $U(\tilde{\nu}_x, \tilde{\nu}_y, f)$.

Four energy bands are visible in Figure 5.21. The top band at the larger

wavenumber corresponds to the thicker part of the material and contains the most energy, suggesting it relates to 3.1mm thick sheet of GLARE which makes up the bulk of the surface area. While the areas with stringers and stiffeners attached give a greater effective thickness they also contain very little energy as is shown in Figure 5.25 (a). The other bands have a lower wavenumber, with each band shifted downwards by approximately $6m^{-1}$. The lower wavenumber indicates a longer wavelength and for a given material and frequency relates to a thinner material. As this structure has no defects there are no parts thinner than the 3.1mm GLARE sheet. Therefore it is suggested that the energy bands at lower wavenumber correspond to Lamb waves present in a fraction of the laminate. This is also supported by the clear regularity and separation of the energy bands.

A filter number map was again determined using a filter bank of 15 filters with a width of $k_{pass} = 200m^{-1}$. An iterative process was used to ensure the 15 filters spanned all measured thicknesses of the specimen. A broad range of filter band path centres was first chosen and used the generate a result. The bandpass centre of the the maximum and minimum filter value in the result is then taken as the maximum and minimum bandpass centre for a new filter stack. This process is then repeated until both the maximum and minimum filter values apear in the results. The results are given in Figure 5.22.

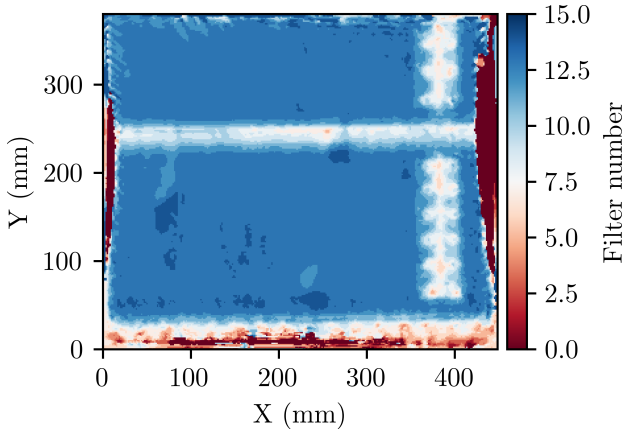

Figure 5.22: Specimen 8 (a) filter number map result and (b) riveted stiffener area.

As with specimen 6 the pincushion distortion was clearly visible along with some minor edge effects. The bulk of the surface was determined as being the same thickness with the stiffener and stringer clearly visible. The bonded stringer is at $Y = 250mm$ and runs the length of the specimen in the X axis. The bonded and riveted stiffener is centred at $X = 385mm$ and spans into the Y direction. A third stiffener that is bonded and riveted is visible at $Y < 30mm$. Figure 5.23 shows the same result but highlights the rivets.

The area directly between the two lines of rivets are identified as areas of thicker material. This stiffener was of a "T" configuration with a wide flange and a central

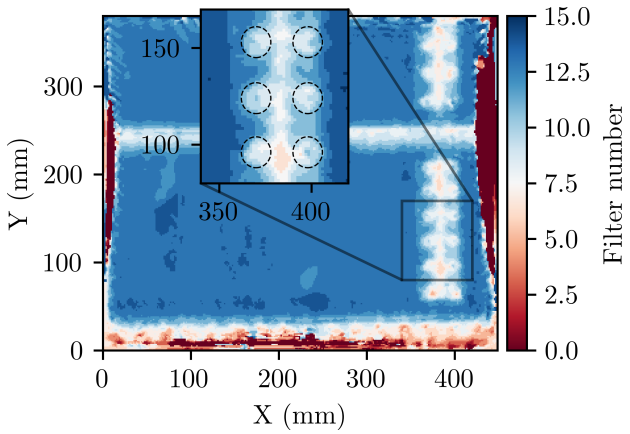

Figure 5.23: Specimen 8 riveted stiffener area.

beam. This central area was correctly identified as being thicker than the surrounding area. A single Vallen transducer was used to excite the structure as can be seen in Figure 5.24.

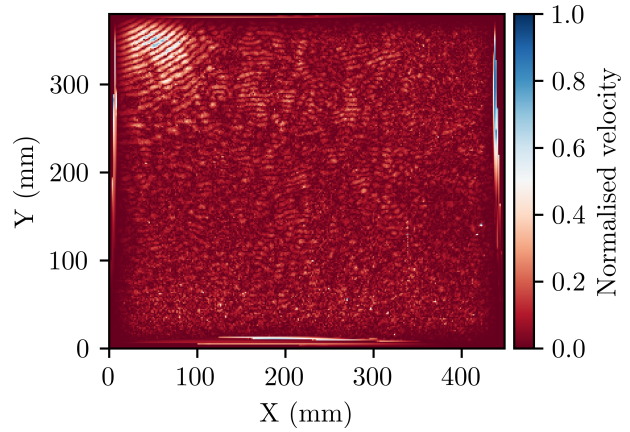

Figure 5.24: Specimen 8 normalised velocity , $u(x, y, t)$, at time $t = 156\mu s$.

The location of the transducer is visible in the top left corner and while Lamb waves appear to have been generated in all parts of the specimen there is a noticeable drop off at $X < 250mm$. This is at the location of the bonded stiffener. Figure 5.25 (a) shows the local amplitude. With further insight into the wave motion given by the local orientation shown in Figure 5.25 (b).

From Figure 5.25 (a) the reduction in normalised energy clearly shows that much of the amplitude of the steady-state excitation is lost post the stringer. The bonded stringer as well as the footprint of bonded and riveted stiffeners have the lowest wave amplitude. The large mass and high stiffness of these structures will have a significant damping effect. As stiffeners are a common features on plate-like structures the benefit of this technique being able to function with multiple sources is clear. The local orientation shown in Figure 5.25 (b) shows the changes in dominant propagation angle caused by reflections around features such as the stiffener and

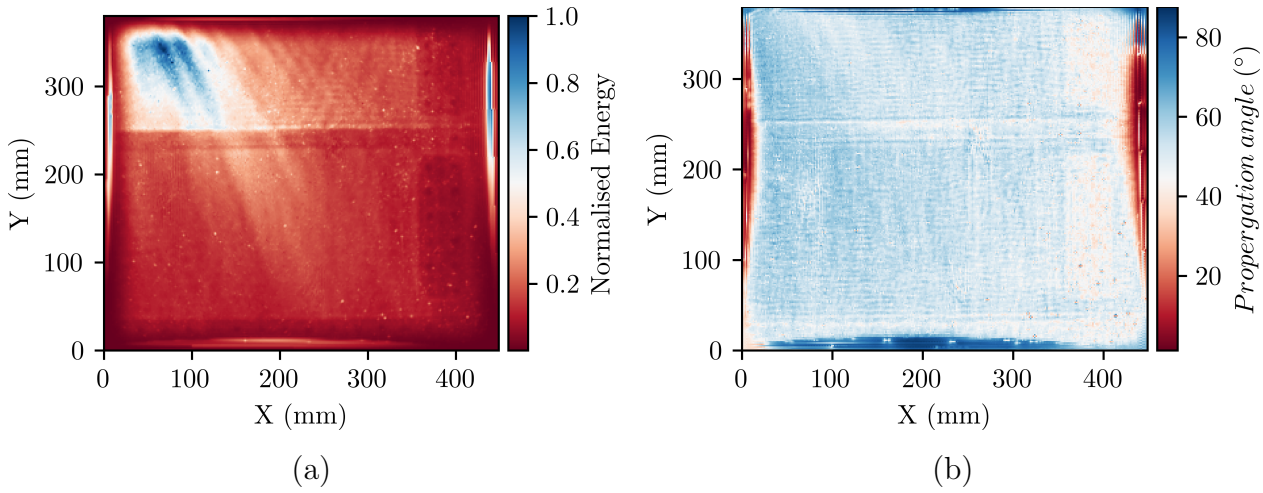

Figure 5.25: Specimen 8 (a) amplitude map $a(x, y)$ and (b) propagation angle map $\theta(x, y)$.

stringer.

Post damage

Using the same processing parameters as using pre-damage in the above section specimen 8 results were processed. Figure 5.26 show the resulting mode number map.

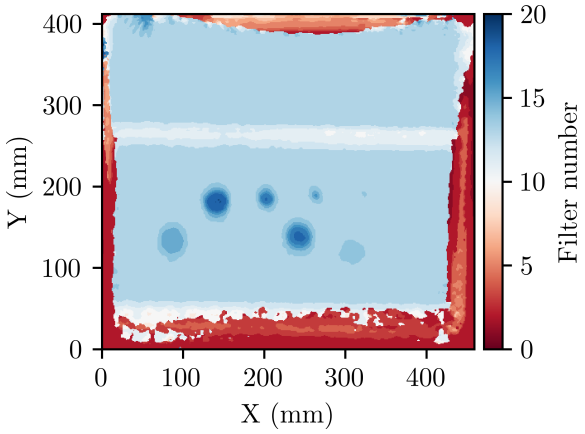

Figure 5.26: Specimen 8 post damage filter number map.

The areas of damage are clearly visible, including the 5mm diameter defect. For the 30mm diameter defects, A, E, F and G as shown in Figure 5.4, are also given correct depth values relative to one another. The depth of defects C and D are underestimated relative to the other defects. Defect C has a diameter of 10mm. From the frequency wavenumber relationship shown in Figure 5.20 it can be seen that at a frequency of $150kHz$, a wavelength of approximately 12.5mm would be expected for the A_0 mode in the bulk of the material.

Local amplitude and orientation maps were also recalculated for the damaged state and are shown in Figure 5.27.

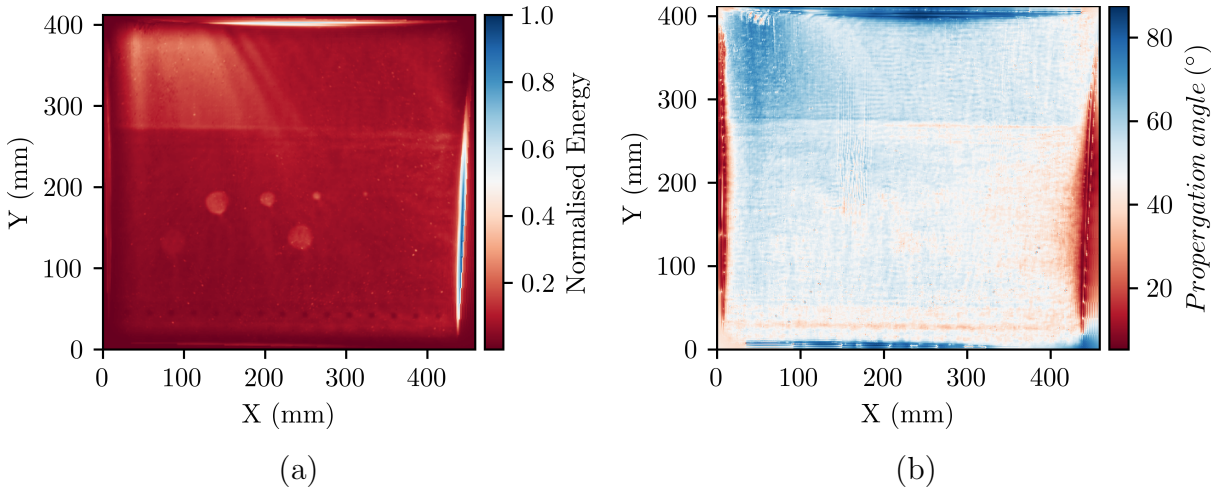

Figure 5.27: Specimen 8 damaged (a) amplitude map $a(x, y)$ and (b) propagation angle map $\theta(x, y)$.

Figure 5.27 (a) shows clear increases in local amplitude at the defects. While not utilised in this section the use of monogenic signal analysis to determine local amplitude could be used to increase accurate location of defect edges. Small changes in local orientation are also visible in Figure 5.27 (b).

5.4.4 Conclusions

An expansion of the Lamb wave WMS technique was demonstrated and was shown to function on a broad range of materials. It was able to identify defects using frequency wavenumber relationships gained from the measurement data. Strongly non-isotropic materials such as those used in specimen 6 were in particular shown to benefit from correction to the filter in the wavenumber-wavenumber domain. While results were very clear, identifying single ply thickness changes, it may be possible to further improve sensitivity by adapting the wavenumber frequency relationship over a range of dispersion angles as this relationship was shown to change. The technique was shown to work with no prior knowledge of the parts material, lay up or geometry. The use and benefit of multi-frequency excitation for composite structures was shown. This was done in conjunction with multiple excitation sources. The use of a Canny edge detection algorithm to identify the wavenumber-frequency relationship was applied for its simple physical interpretation and ease of application. It would however be expected that the application of a Convolutional Neural Networks (CNN) to detect the A_0 mode in in the frequency domain would give more repeatable and accurate results. Likewise a CNN could be applied to identify dispersion characteristics in the wavenumber-wavenumber domain. A CNN would be

a good candidate for these applications due to its success in similar applications in computer vision problems [96]. When applying this technique to a large number of the same part, information on these frequency domain relationships would not need to be recalculated for each measurement. With a number of measurements of a part of known thickness it would also be possible to directly relate a mode number to a true material thickness.

6. Complex surface geometries and feature detection

6.1 Introduction

All measurements in this work so far were completed on flat, plate like structures. This is in line with previous work that utilises wavenumber filtering of wavefields for damage detection. Some work has been completed on pipe structures or structures with a very large radius of curvature [10, 73, 97]. Geometries such as the cylinder of a pipe fall into the category of developable surfaces. A developable surface can be defined as any surface with a Gaussian curvature of zero, in other words any surface that can be flattened onto a 2D plane without any distortion [98]. It can be thought of as a surface shape that could be created by bending a piece of paper. When considering a wavefield this would allow it to be mapped onto a 2D plane without distortion of wavelength. In the cases of large radii of curvature, like those commonly found in structures such as aircraft wings, surfaces were assumed to be flat. This assumption has a negligible effect on the estimation of the wavelength, with A_0 mode wavelengths being on the scale of tens of millimeters for common material thicknesses and frequency ranges. Radii of curvature on the scale of tens of centimeters will therefore cause little error in estimation of the A_0 mode wavelength.

While some work has employed wavenumber related techniques on pipe structures, as 1D LDV or SLDV systems were being used, the pipes were being measured and periodically rotated [58, 73, 99]. As wavelength is being used to determine thickness this directly relates to the accuracy of this technique. It is also of particular importance in thicker parts, where small changes in wavenumber can relate to significant thickness changes.

Work by Spytek et. al. [100] aimed to further wavenumber mapping approaches to non-developable complex structures. In their work a SLDV was used. While this allows the laser to be driven over the surface of a structure it can not differentiate between in-plane and out-of-plane displacement. To complete the measurement of a complex surface they had to realign the specimen to the SLDV multiple times to allow the laser to measure the wavefield on different surfaces. To account for variable

geometry a nonuniform Fourier Transform (FT) was applied over each measurement area. As a SLDV system is used this requires prior knowledge of the specimen's geometry as well as known alignment between the specimen and the SLDV, further complicating the set up. While the use of a nonuniform FT allows for certain structures to be measured using wavenumber based techniques it does not account for distortion present when non-developable geometries are presented. The use of a 3D SLDV makes this step substantially simpler as a good estimate of the 3D spatial coordinates of each measurement point are known.

While developable surfaces can be mapped onto a 2D plane without distortion this is not an arbitrary task when considering parts that do not have the same level of symmetry or consistent curvature as that found in pipes. Consider for instance a surface that has curvature with both positive and negative radii and curvature of a variable radius. Correcting this distortion on a wavefield is a non arbitrary task.

For in-situ tests a set up is proposed where a 3D SLDV can be placed some distance from the area to be measured. Ultrasonic energy is then driven into the structure using either a contact transducer, air coupled transducer or pulsing laser ultrasound. The use of a 3D SLDV system allows for an estimate of the specimen's shape to be extracted using triangulation alongside the recording of the wavefield.

This chapter proposes the use of mapping algorithms to use the geometric information obtained by the 3D SLDV to map the wavefield of complex geometries onto a 2D plane so that WMS can be performed. This means no prior knowledge of the specimens geometry or its position relative to the 3D SLDV needs to be known, representing a significant step towards real world applications.

While non-developable surfaces only account for a small proportion of the surfaces found on structures such as aircraft or wind turbines they are also considered. By definition distortion will be present when mapping these surfaces onto a 2D plane. An algorithm is chosen to minimise distortion and give the most accurate estimate of wavelength.

While WMS has been shown to give accurate thickness maps with high spatial and depth resolution the clear definition of some edge features can still be challenging. This has been the case for a broad range of wavenumber based techniques [0, 62, 78, 101]. As such the use of monogenic signal analysis is proposed to generate a local amplitude map from which edge features are extracted using Canny edge detection [93]. The detected features can then be shown along side thickness estimates to help visualise structural features and potential damage. A novel and robust complete imaging approach is presented in this work representing a significant step towards practical real world applications of WMS.

6.1.1 Mesh Parameterization

This section presents a method of spatial parameterisation that allows an accurate representation of the spatial wavelength to be gained in a structure with a non-developable geometry. As such this technique will allow a single algorithm to be applied to any geometrical shape. The main limitation is that the maximum angle of incidence between the surface of the specimen and the SLDV can not be too great. At large angles it will not be possible to have the surface visible to all three laser heads preventing measurement. An increased angle of incidence between the laser and the sample will reduce spatial resolution and the signal to noise ratio. A 45° angle of incidence to the specimen has been shown to cause significant distortion [40]. For highly complex structures the specimen or the 3D SLDV would have to be re-positioned and multiple measurements would have to be combined. Combining the vision system present on the a 3D SLDV and fiducials on the structure would make this possible.

There are a large number of techniques that map the surface of a 3D structure to a 2D plane or vice versa. These have had applications in areas such as computer vision or texture mapping [102]. Different processes have been designed for different purposes and as such offer a number of trade-offs. Authalic mapping aims to preserve the area of each mesh element, whereas conformal mapping aims to preserve the angle between nodes and isometric mapping preserves length features [102]. Most mapping algorithms are not solely based on a single principle but a combination of them. This chapter will use As-Rigid-As-Possible (ARAP) as described by Liu et al. [102]. This algorithm can be found in libigl [103] which is an open source C++ geometry library. The python bindings for libigl were used to implement the ARAP algorithm in this work. The ARAP method was chosen due to its ability to preserve shape, computational speed and simplicity. When considering steady-state wavefields, shape distortion is the primary concern that would lead to an inaccurate estimation of spatial wavelength.

6.1.2 As Rigid as Possible mapping

Given a mesh of triangles, each triangle has the parameters $x_b = (x_b^0, x_b^1, x_b^2)$, locating it in a plane, where b ranges from $b = 1$ to B which is the total numbers of triangles present in the mesh [102]. The area of each element of the mesh is given by A_b. Using a piecewise linear function these 3D coordinates of x_b are mapped to a 2D plane and assigned coordinates as $u_b = (u_b^0, u_b^1, u_b^2)$. A number of transformations are used to transform x_b to u_b. $J_b(u)$ denotes a 2x2 Jacobian matrix which is used to perform this linear transform with auxiliary linear transforms being given by L_b [102]. L_b is one linear transform from a set of allowable transforms B. Equation

(6.1) gives the energy of the paramaterization [102].

$$E(u, L) = \sum_{b=1}^{B} A_b ||J_t(u) - L_b||_F^2 \tag{6.1}$$

The Frobenious norm is donoted by $|| \cdot ||_F$. This now becomes an optimization problem where the energy is to be minimised. Equation (6.2) shows the optimization problem faced where $L = L_1, L_2, ..., L_B$, L being an allowable linear transform. [102].

$$(u, L) = argmin_{(u,L)} E(u, L) \tag{6.2}$$

Conformal mapping is not desirable in this use case as scaling factors can distort triangles, therefore losing length data for a triangle which is of key importance when identifying small changes in wavenumber in the wavefield. As such for ARAP mapping the allowable transforms of rigid rotation, M, are defined by Equation (6.3) [102].

$$M = \left\{ \begin{pmatrix} cos\theta & sin\theta \\ -sin\theta & cos\theta \end{pmatrix} : \theta \in [0, 2\pi] \right\} \tag{6.3}$$

More detailed information on the geometric transform can be found in work by Liu et al. [102].

A further concept when considering geometric transforms is Gaussian curvature. Gaussian curvature, K, is given by the product of the two principle curvatures κ_1 and κ_2, as shown in Equation (6.4).

$$K = \kappa_1 \kappa_2 \tag{6.4}$$

Developable surfaces, by definition, have a Gaussian curvature of zero [104]. The curvature is the inverse of the radius which best describes the curvature in an axis at that point [104]. As such the Gaussian curvature of a sphere of radius, q, is given by Equation (6.5).

$$K = \frac{1}{q^2} \tag{6.5}$$

Once coordinates were mapped onto a Euclidian plane the wavefield was interpolated onto those new coordinates using a cubic spline as described by Dierchx et al. [81]. The data could then be placed into a 3D matrix with two spatial and one temporal axis in the form of $u(x, y, t)$. Once in this form it was processed as described in Chapter 3.1. The spatial Z axis values of the original coordinates were then interpolated over the evenly spaced grid used to calculate the thickness map. This allowed the results to be shown in the form of a 3D surface plot.

6.1.3 Experimental setup

As in previous chapters a Polytec PSV-500-3D-M 3D SLDV was used to capture the velocity at a number of discrete points on the structure. 100 measurements where captured at each spatial point and averaged in the time domain to improve the signal to noise ratio. Two specimens were selected, specimen 1, a 3mm thick aluminium plate with three thickness reductions, was put through a roller to bend it and give it a curvature. The plate did not have a constant radius of curvature as the edges cannot be bent by the roller. With an arc height of $40mm$ the radius of curvature was approximated to be $210mm$. This specimen was labelled as specimen 9. Dimensions of the features of specimen 9 are given Figure 3.1 (b). It is however noted that bending the specimen through rolling will likely have caused a small thickness reduction of the bulk surface area of the plate. The specimen was excited using a FM signal ranging from $30kHz$ to $350kHz$ at 200Vpp, which was driven into the specimen through a single Pancom Pico-Z PZT transducer which was super-glued to the specimen. The measurement area was $260mm$ by $260mm$ with the transducer located at $X = 130mm$ and $Y = 270mm$. Figure 6.1 (a) show the measurement area in red and transducer location.

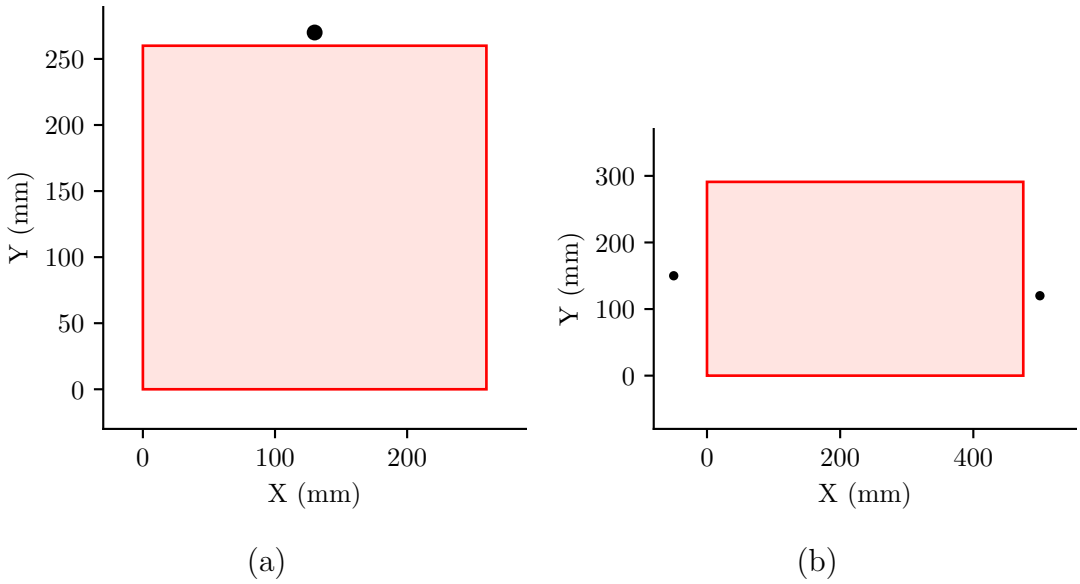

Figure 6.1: Specimen 9 (a) and 10 (b) measurement area (red) and transducer location (black).

A second specimen, specimen 10 is a aluminium panel removed from a Hawk jet. It has a nominal thickness of 0.75mm with regions of 1.75mm and 1.5mm thickness. Likewise it was excited using a $30kHz$ to $350kHz$ FM signal at 200Vpp, which drove two Vallen System VS900-M PZT transducers. These transducers were clamped to the structure with grease used as a coupling agent. The non-developable nature of the surface meant establishing a rectangular measurement area. The measurement

area of specimen 10 was nominally 475mm by 291mm. The transducers were located at $X = -50mm$, $Y = 150mm$ and $X = 500$, $Y = 120mm$. The transducer location in relation to the measurement area is shown in Figure 6.1 (b). Specimen 10 also had a hatch in the scan area. The thickness of the hatch material was 1.75mm. It was attached with three screws and a silicate sealant. Images of the rear faces of both specimens 9 and 10 are shown in Figure 6.2.

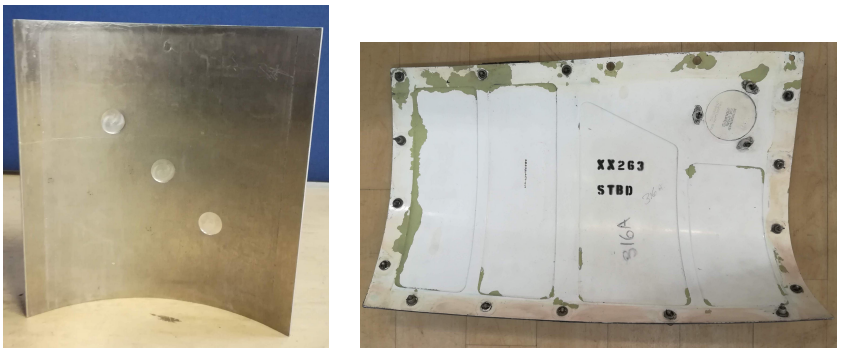

(a) (b)

Figure 6.2: Rear faces of (a) specimen 9 and (b) specimen 10.

As well as the measurement data, geometric data were taken from the 3D SLDV. These data were generated through the 3D alignment of the lasers as well as the 3D triangulation that is performed at every ten scan point. During 3D alignment each laser head is turned off individually and the vision system confirms the alignment of all three lasers onto the same point. This information further updates the geometric model which is exported in the form of a tri mesh giving the coordinates of each measurement point once the measurement is completed. Better estimates of the surface geometry of parts can be obtained from the 3D SLDV by first determining the exact positions of the lasers and their relation to the vision system with a calibration tool that gives. The calibration tool gives points a known distance apart. This step was however not performed as it represented an increase in measurement setup time. When considering real world application it would be advantageous not to have to perform this step.

6.2 Results and Discussion

6.2.1 Specimen 9 results

Specimen 9 was processed using the same WMS process as used to process specimen 1. A filter bandpass of $k_{pass} = 100m^{-1}$ was applied and filters were calculated at thicknesses between 0.25mm and 3.25mm in 0.125mm intervals. Mode filters were

calculated using a flattop shaped window. To show the benefits of ARAP mapping the results were first found using only the X and Y coordinates. The coordinates were rotated as to minimise the angle between the bottom corners. They were then transformed to ensure the bulk of the surface was perpendicular to the angle of the lasers. This ensures a fair comparison is given between mapped and un-mapped results. As before all X and Y spatial coordinates were re-sampled and interpolated using a cubic spline as in the analysis of Dierckx [81]. to give evenly spaced data points before an FFT was performed. Figure 6.3 (a) shows the WMS results of specimen 9 using only the X and Y coordinates, assuming a flat structure. Figure 6.3 (b) shows the results where WMS has been performed after the coordinates of the measurement points had been projected onto a 2D plane using ARAP algorithm.

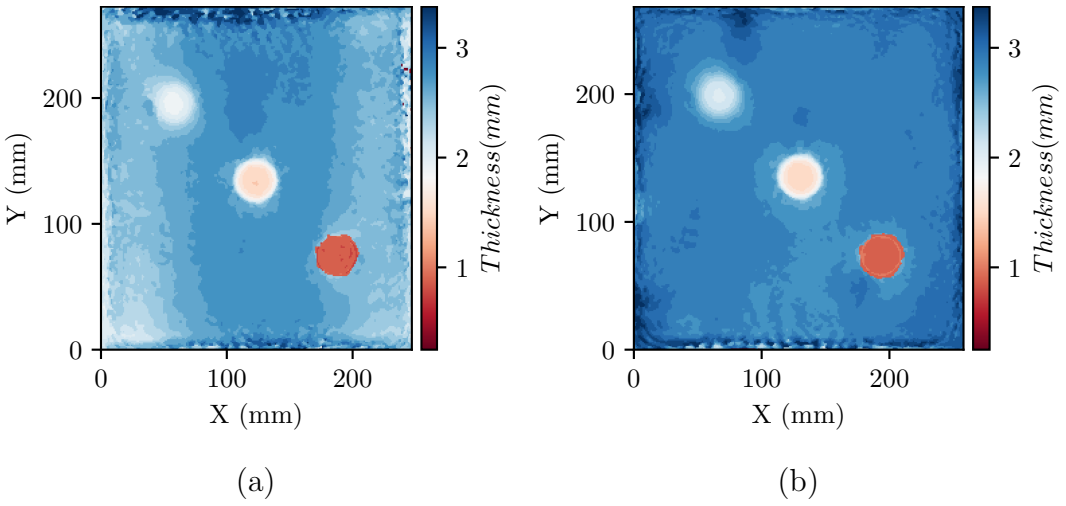

Figure 6.3: Specimen 9 results (a) non-mapped (b) ARAP mapped.

The first notable issue when not mapping coordinates onto a 2D plane is the decrease in length in the X axis. The length in the X axis is measured to be $247mm$ without mapping in comparison to $258mm$ when the geometry is flattened using ARAP mapping. The measurement area was set between two lines marked on the specimen in the X axis. These were nominally 260mm apart. Without mapping, the centre of the panel is estimated to be 2.75mm thick with a reduction of thickness down to 2.5mm at the edges. As the angle between the specimen and the vibrometer increases the wavelength appears to shorten, corresponding to a lower thickness. Figure 6.4 shows a cross section of specimen 9 at $Y = 135mm$.

When coordinates are corrected using ARAP mapping the thickness of the plate structure is estimated to be 2.88mm thick. The area directly around the defect in the centre of the plate was estimated to have a thickness of $2.75mm$ using ARAP mapping. It was confirmed through measurement of the specimen that it had a reduced thickness of 2.9mm over most of the central area ($X = 25mmtoX = 230mm$). This is likely due to the roll bending process. The non-mapped results correctly es-

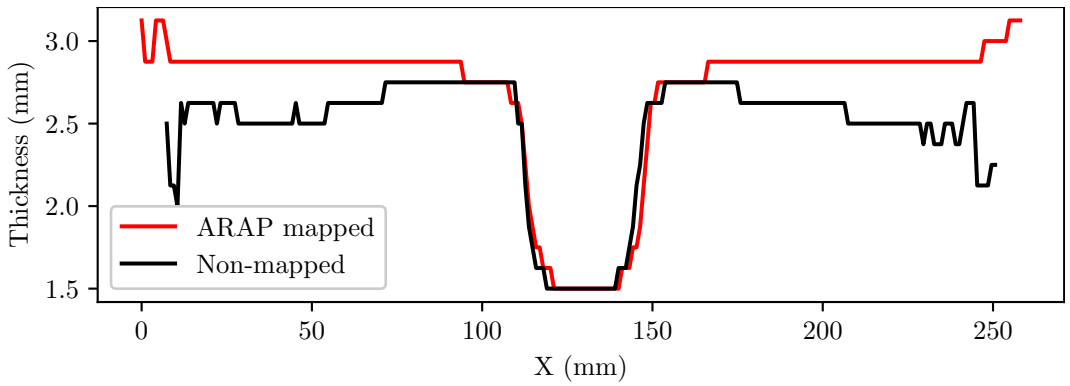

Figure 6.4: Specimen 9 cross section at $Y = 135mm$.

timate the area in the center of the specimen around $80mm < X < 190mm$, where the specimen is perpendicular to the SLDV but then indicates reduced thickness towards the edges.

Once a flat projection of 3D coordinates had been determined and thickness results found, Z axis coordinates were interpolated over the new X and Y coordinates. These were then mapped as a surface with the thickness results. This is shown in Figure 6.5.

A local amplitude map was also calculated for this specimen using the ARAP mapped coordinates and is shown in Figure 6.6. The envelope of the wavefield was found using Equation (2.30) at each time sample and then averaged in the time domain.

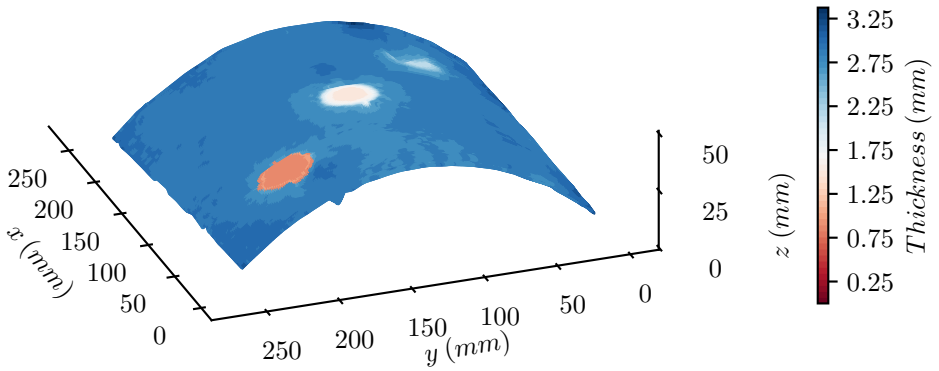

Figure 6.5: Specimen 9 ARAP mapped results in 3D.

The three thickness reductions are clearly shown with good definition of the feature edges. The largest thickness reduction shows the highest amplitude with a decrease in amplitude shown at the greatest material thickness. The relationship between material thickness and local amplitude was found by taking the average amplitude of an area of ten by ten samples at each area of differing thicknesses. Results are shown in Figure 6.7. The line of best fit is in the form of $y = a * e^{-c*x} + d$

also shown, where a, c and d are constants.

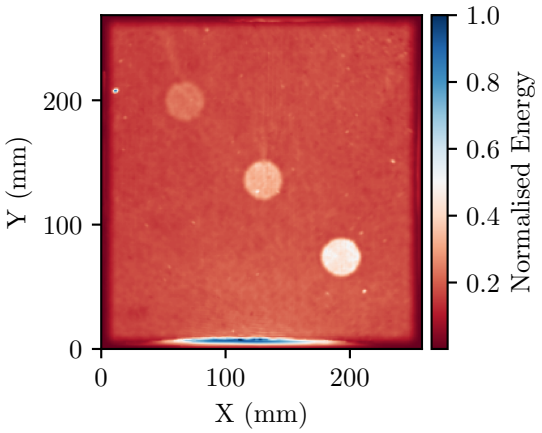

Figure 6.6: Specimen 9 local amplitude map.

When considering the plane wave function, $f(x) = Ae^{\pm ixk}$, where k is wavenumber, A amplitude and x is a spatial coordinate this same relationship is also present. Knowing the thickness of one or more areas of the specimen it may be possible to determine thickness from local amplitude maps.

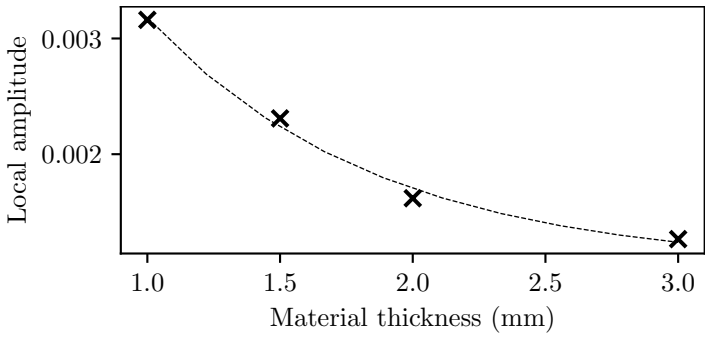

Figure 6.7: Specimen 9 local amplitude thickness relation.

Unlike when local amplitude maps were generated for composite specimens as in Chapter 5.1 full steady-state excitation is achieved allowing clear identification of geometric features. When considering mode filtered results some edges show a gradual change in thickness. This is particularly noticeable for small thickness changes such as that seen around the $1mm$ thickness reduction in specimen 9. The wavelength of the Lamb wave along with the spatial sampling frequency means determining these instantaneous thickness changes can be challenging. Using the local amplitude map a Canny edge detection algorithm was applied as implemented by OpenCV [95]. Figure 6.8 (a) shows the detected edges with a standard deviation of $\sigma = 1.4$. The detected edges can then be shown along with the thickness map generated by mode filtering to help allow the easy identification of geometric features as shown in Figure 6.8 (b).

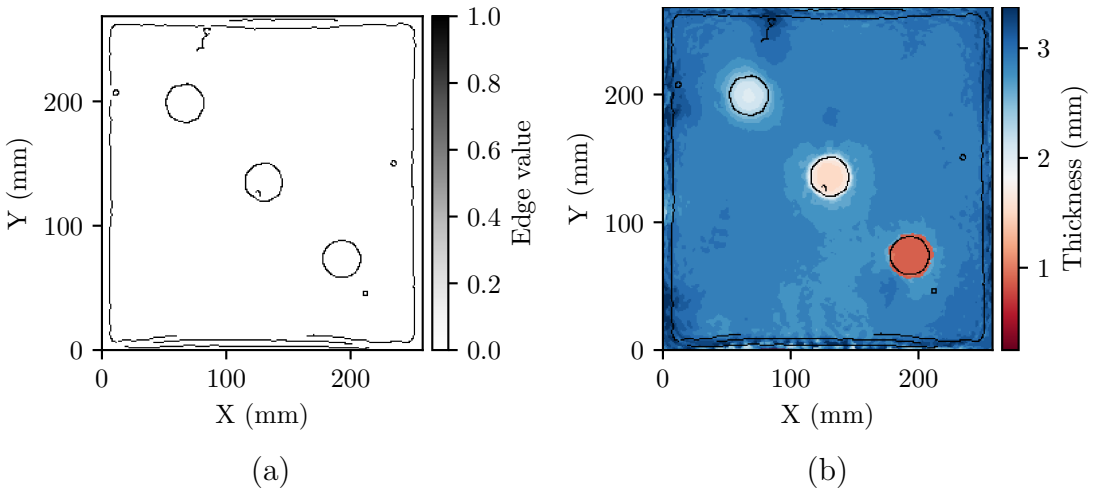

Figure 6.8: Specimen 9 (a) Detected edges in amplitude map and (b) edges overlaid on mode thickness map.

The three thickness changes are clearly identifiable along with an edge around the perimeter of the measurement were the spatial Tukey window was applied. A small number of noise artefacts are also identified as edge features. The edge detection shows the small amount of error present at the edges of the defects. The thinning to $1mm$ is the largest thickness reduction and shows a sharp transition between the 3mm and 1mm thickness. Some area outside of the defect is however incorrectly identified as being 1mm thick instead of 3mm thick. As the change in material thickness reduces, thickness estimates show less abrupt thickness changes. For the region of $2mm$ thickness a gradual transition is visible between the $2mm$ and $3mm$ thick regions. This is due to the filter width selected to process this data. Had a larger k_{pass} value been used this transitional region would have been reduced but so would have depth resolution. As such the edge detection can mitigate some of the trade-offs between spatial and depth resolution by demarcating edges of thickness change. While this would show up defects such as delamination defects that often have abrupt thickness changes it would not be expected to effectively show gradual thickness reductions such as those brought about by corrosion defects.

6.2.2 Specimen 10 results

A more complex geometry was offered by specimen 10. Again the results were first found using only the X and Y coordinates projected onto a flat plane. Before this, alignment and orientation of the coordinates were adjusted so that the four corners would generate a plane perpendicular to the scanning laser. The spatial coordinates were also interpolated to ensure even spatial sampling. Mode filters were calculated using a bandpass width of $k_{pass} = 100m^{-1}$ and a flattop shaped window. Filters were centered around thicknesses between 0.25mm and 2.5mm at 0.125mm intervals.

Figure 6.9 shows the non-mapped and ARAP mapped results.

Using the mapped X and Y coordinates Z coordinates were re-interpolated over those values. The edges of the results were cropped by five samples to remove some of the spatial measurement errors present at the edges. Thickness map results weere mapped onto these 3D coordinates, giving the results shown in Figure 6.10. The un-mapped nature of the results shown in Figure 6.9 (a) can be identified from the curved appearance of the stiffeners.

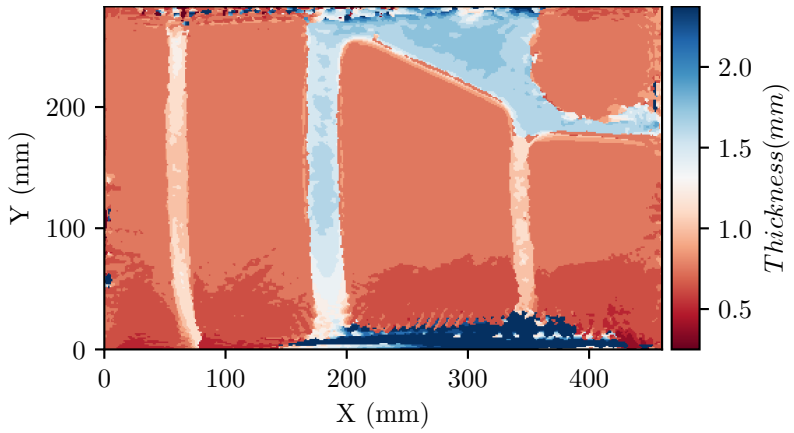

(a)

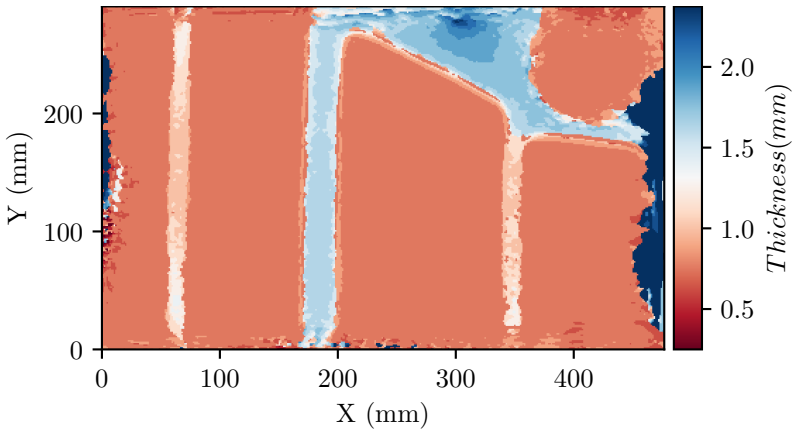

(b)

Figure 6.9: Specimen 10 results (a) non-mapped (b) ARAP mapped.

The greatest angle between the surface of the specimen and the SLDV are in the region of $Y < 100mm$. Substantial levels of spatial distortion thickness estimate error are seen in this region of the non-mapped results in Figure 6.9 (a). As this area of the specimen is at an angle relative to the SLDV the wavelengths would be expected to be interpreted as shorter than they truly are. Reduced wavelength, and therefore increased wavenumber, should result in a lower thickness estimate. This is seen across this area with the bulk of the material estimated at a thickness of $0.65mm$ and in some places thickness reduces to as low as $0.5mm$. There is also a

region of over-estimated thickness between $Y < 40mm$ and $150mm < X < 430mm$. This is likely due to the wavelengths being outside of the range of the wave mode filters.

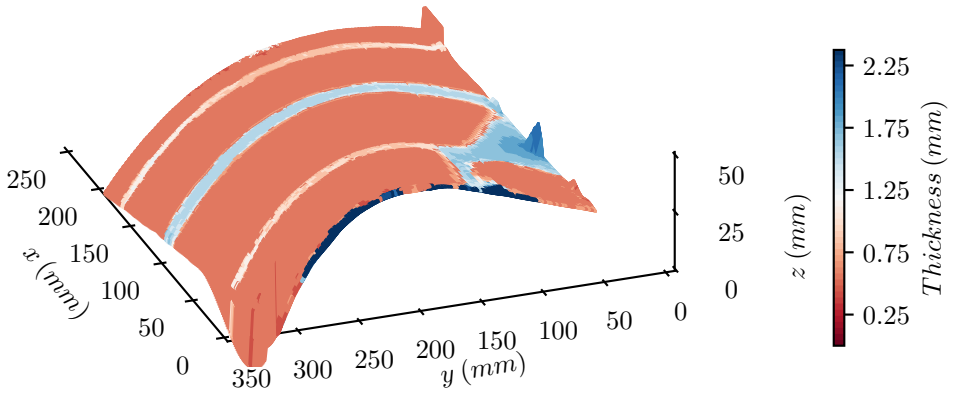

Figure 6.10: Specimen 10 ARAP mapped results in 3D.

The steady-state excitation nature of the measurement combined with its geometry means that while Lamb waves will propagate in all directions, distortion will be dominant in a single axis, resulting in unpredictable measurement errors in certain regions. The nature of the curvature of the specimen can be seen in Figure 6.10. Once coordinates had been recalculated onto a flat plane using ARAP mapping and mode filtering had been performed, the distortion previously seen in the area of $Y < 100mm$ is removed as can be seen in Figure 6.9. The bulk of material is correctly assigned a thickness value of 0.75mm. The stiffeners are now also shown as being straight. Prior to ARAP mapping being performed the stiffener at $X = 180$ was shown to have reduced thickness at $Y < 100mm$. Post mapping a uniform thickness value of $1.625mm$ was assigned to this region.

Post ARAP mapping had been performed new artefacts are introduced at either end. A small region at $X < 10mm$ is estimated to the largest thickness value, as is a region at $X > 250mm$. This is largely due to the geometric transform. As the area over which the wavefield is measured is a rectangle projected onto a complex shape the edges are not straight once projected onto a 2D plane. Without ARAP mapping the X dimension is $460mm$ whereas with mapping is extends to $477mm$. The empty spatial data points that result from mapping the coordinates to a 2D plane are assigned a value of zero. While this accounts for much of the error at the edges in the X axis, which measured $2.5mm$, there are still edge artefacts which appear to cause errors a few millimeters further into the scan area. The spatial Tukey window is applied after the coordinates are mapped onto a 2D plane. As such there will be a step change in the wavefield causing errors when estimating wavenumber. While performing spatial windowing before ARAP mapping is completed might reduce such artefacts in this instance it would still result in an uneven spatial window one

ARAP mapping had been performed. For measurements of complex geometries the scan area would need to be cropped post being projected onto a plane to reduce these effects and minimise the amount of lost data at edges.

At $X = 308mm$ and $Y = 285mm$ a thickness increase is also shown in the thicker area of the stiffeners. To further explore this the Gaussian curvature of the surface was calculated and is shown in Figure 6.11.

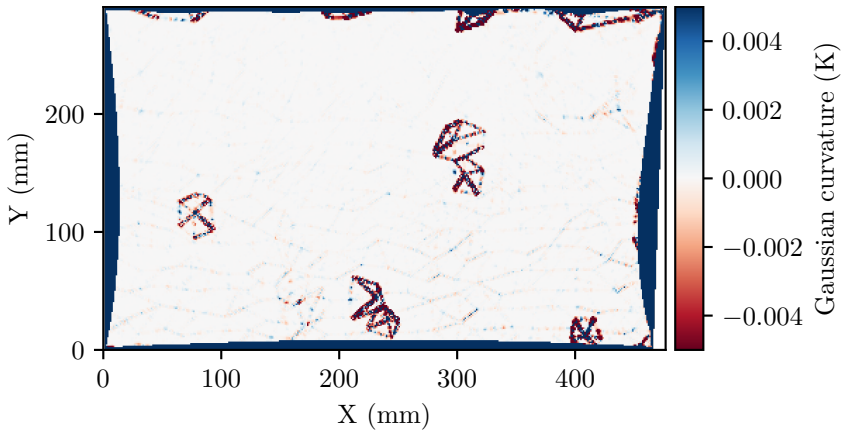

Figure 6.11: Specimen 10 Gaussian curvature.

In the region of $X = 308mm$ and $Y = 285mm$ an area of high Gaussian curvature is shown which indicates a measurement artefact, as the surface of the specimen is smooth. The edges of the measurement area are particularly susceptible to this types of errors. A low Gaussian curvature across the bulk of the geometry shows that the geometry of the specimen can be mapped to a 2D plane with limited distortion. A number of points show higher Gaussian curvature due to measurement errors but seem to introduce limited error in the resulting thickness map. The 3D plot given in Figure 6.10 also shows the distortion present in the geometrical data causing the distortion at $X = 308mm$ and $Y = 285mm$.

A local amplitude map was determined for specimen 10, using the same process as used for specimen 9, and is shown in Figure 6.12. Again the local amplitude map offers a clear view of the geometric features present in the structure. Edges of the thicker stiffener regions are well defined.

The hatch and the three bolts holding it to the structure are also visible. This figure does also serves to show the benefits of WMS. While stiffeners are clearly visible it is not possible to distinguish a thickness difference between the stiffener at $X = 300mm$ and those at $X = 120mm$ and $X = 410mm$. The difference in the thickness of these stiffeners is however clearly shown in the WMS result. The local amplitude map can easily be determined from the data gathered for mode filtering. As such it would offer extra information about the geometry or damage in the structure alongside mode filter mapping. Canny edge detection as implemented by OpenCV [95] was applied to the local amplitude map. Detected edges are shown in

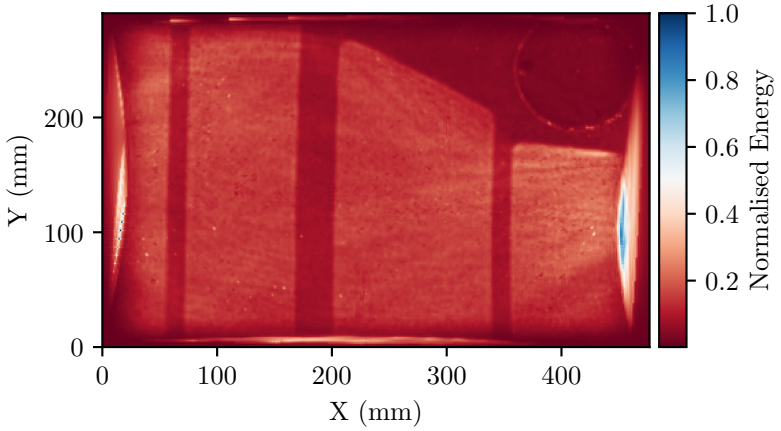

Figure 6.12: Specimen 10 local amplitude.

Figure 6.13 (a). The detected edges were overlaid onto the thickness map determined by the WMS as shown in Figure 6.13 (b).

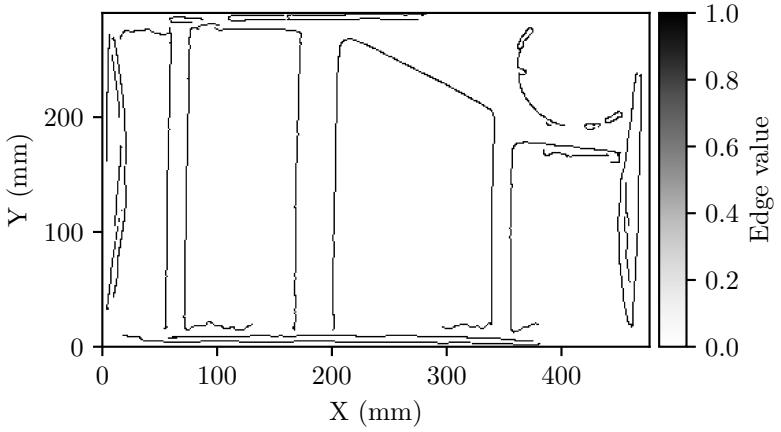

(a)

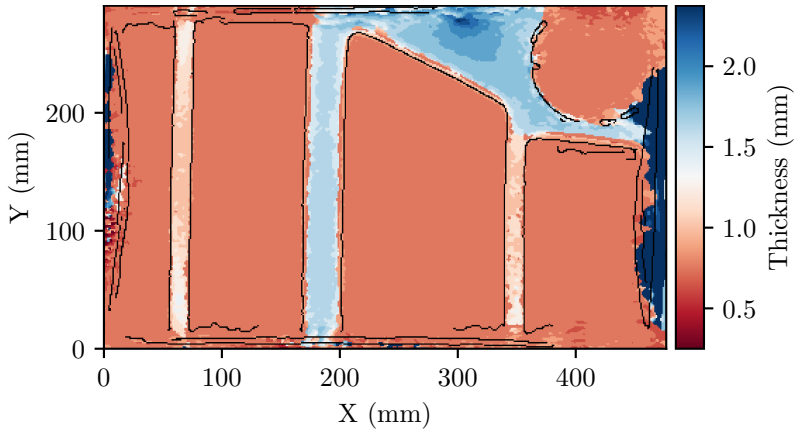

(b)

Figure 6.13: Specimen 9 (a) Detected edges in amplitude map and (b) edges overlaid on mode thickness map.

On specimen 10, as well as specimen 9, artefacts are present around the edge

of the measurement area. These are due to a combination of the spatial Tukey window applied before filtering as well as the ARAP mapping that results in a non-rectangular surface. As local amplitude is not wavelength dependent and it is not liable to the same distortion seen in wavenumber estimation of complex geometries. As such it offers another information source which helps allow true features and artefacts to be distinguished. Likewise the local amplitude map is susceptible to amplitude dependant noise, which WMS is not. For instance an edge is detected around $X = 400m$ and $Y = 180mm$. This does however not relate to any thickness change so can be classed as likely being a measurement artefact. Likewise the error in thickness estimation seen around $X = 300mm$ and $Y = 280mm$ does not coincide with any edges as it is the result of an error in the estimation of the specimen's geometry.

6.3 Conclusions

A method was shown where ARAP mapping was employed to map wavefields of non-developable geometries onto a 2D plane to allow WMS to be completed. The Specimens geometry was extracted from data taken while measuring wavefields using a 3D SLDV, successfully demonstrating a step towards real world application where no prior knowledge of the specimens geometry or orientation to the 3D SLDV is required. The ability to use the spatial coordinates gathered in the measurement represents a significant advantage compared to other solutions that would require a secondary measurement of the geometry. The distortion generated in the wavefield by these complex geometries clearly caused errors when performing WMS. This distortion would likewise be present with other methods that rely on the wavelength of Lamb waves for damage detection. Thicker structures would be more greatly affected by any distortion of wavelength due to the reduced change in wavenumber for a given thickness change at larger thicknesses. It was noted that estimation of the geometry had higher errors at the edges of the measurement area. This could however be easily corrected by excluding these regions. Likewise surface smoothing could be applied to reduce out-of-plane error in the positional coordinates of the measurement points when applying this technique to structures such as wind turbines with smooth surfaces. A novel use of monogenic signal analysis combined with Canny edge detection was also presented. It was shown that using a steady-state multi-frequency excitation allowed for a clear amplitude map to be generated directly from the wavefield data that was free from dominant wavelengths or high amplitude areas due to attenuating waves traveling through the specimen. This allowed for the Canny edge detection algorithm to be applied to clearly identify sudden changes in thickness. This offers the ability for thickness maps to be compared to

known part geometries by referencing edge features.

7. Python package

As part of this work a Python package "CUSP" was created. The purpose of this package is to simplify the task of performing wavenumber and WMS tasks. Gaining the results presented in this work presented a number of computational challenges. At the core, data sets were very large. Once zero buffered to 512 spatial samples and with 1024 temporal samples, wave fields contained $268 * 10^6$ data points.

CUSP offers a general class WaveNumber that consists of tools to perform tasks such a frequency filtering, plotting, windowing, and other filtering and visualisation functions. All operations are performed on WaveNumber objects that contain information such as temporal and spatial sampling frequencies, scan points spatial coordinates and wavefield data in the form of an evenly sampled matrix with two spatial and one temporal axis.

A child class of this is PolytecUFF which facilitates the importing of data directly from Polytec vibrometers in the form of a .UFF file. The class converts the temporal data streams given with a spatial coordinates to an evenly sampled wave field matrix. It also has a number of functions to perform tasks such as rotating spatial sampling points to straighten the lower edge and alighting the spatial coordinates so that the bulk of the geometric face is perpendicular to the SLDV.

A further child class, FilterBank, which generates and manages filters. When processing over a larger thickness range with 24 steps a filter stack will have $9 * 10^9$ data points. When stored in 64bits, that converts to 48GB. This class manages the reading, writing, and naming of these files and also has the capability to split filters into multiple smaller files allowing batch processing. All objects are converted to a byte stream and saved in a .p format using data pickling, a form of data serialisation. The current data handling process does however require enough RAM to simultaneously load the measurement data and a filter and still have a third of the RAM free as protocols such as multiplication of the data and the filter will generate a third object. For most operations this will be no less then 16GB. Further work would be required to ensure this process runs fast on less powerful computers.

The generation of the filter banks presented some challenges in terms of computation time. Initial filters were calculated in a Cartesian coordinate system but when considering the symmetry across the filter in the frequency domain, the computa-

tion of a single filter took in excess of 20 minutes. This time was vastly reduced to around 5 seconds by computing filters in the polar domain where isotropic filters are identical at all angles at a given frequency. The OpenCV package was used to convert these polar domain filters into the Cartesian domain through a C implemented function. This reduced the computational time significantly and helped allow a large number of filters and filters of different band pass widths to be calculated.

While the FilterBank package creates mode filters for non-isotropic materials a further module CompositeWave was also created to deal with the specific requirements of non-isotropic or unknown materials. This includes functions to determine and verify frequency-wavenumber relationships as well as wavenumber-wavenumber relationships.

While not written with an end user in mind this package delivers powerful tools for further investigation into wavenumber, wave mode and other frequency domain filtering approaches. With the tools provided mode filtering can be performed in only a few lines of code. Without these tools much of the work presented here would not have been possible.

The full package will be made available at git@bitbucket.org:frederickpurcell/wavenumber.git (This is currently a private repository)

8. Discussion, Conclusions and Future Work

8.1 Discussion

Through this work many challenges faced by wavenumber based NDT methods have been addressed. While much work still needs to be completed before this technique becomes a viable alternative to current methods, such as ultrasonic testing, significant steps have been taken to realise real world implementation. The work presented here offers solutions for many factors that previously limited full-field wavenumber based NDT.

Wavenumber filtering, as proposed by Flynn et al. [65], was limited by its single frequency excitation nature. Existing methods used application of broad band mode filters before performing wavenumber filtering at single temporal frequencies. No only did this method limit the utilisation of the large volume of information contained in a full-field measurement but it also relied purely on out-of-plane data. The use of mode filters as presented in this work allows all temporal frequencies to be considered in a single result. This showed substantially improved results when compared to single frequency measurements. The use of a broad frequency range also helped to reduce dependence on transducer characteristics as well as ensuring energy is driven into the material at all thicknesses. Compared to recently published work using wavenumber to detect damage [101] results achieved using wave mode filtering offer both better spatial and depth resolution.

Previous work had applied wavenumber based damage detection to composite structures. However none of these methods accounted for the fact that dispersion characteristics can vary greatly over different propagation angles [61, 67, 78]. Analysis of dispersion behaviour was performed over the measurements frequency range. Wavefields were captured for a range of composite materials. Using both in-plane and out-of-plane velocity data, wavenumber dispersion curves, as well as polar form phase velocity dispersion curves, were generated. Measured dispersion characteristics were used to build mode filters that allowed relative thickness maps to be determined from multi-frequency wavefield data. The use of multi-frequency exci-

tation for a single result had previously not been achievable due to the requirement to know the frequency-wavenumber relationship for the specific composite. Once again the superior performance of multi-frequency excitation was shown compared to single frequency results. It was shown that considering composite materials as being isotropic caused little error in thickness estimates of quasi-isotropic composites like those used in previous work [61, 67, 78]. When applying the same process on highly anisotropic materials significant error was introduced. By determining the relationship between wavenumber and dispersion angle from the frequency domain measurement data, mode filters were adapted which significantly reduced error in thickness estimates. This not only offered substantial improvements over existing techniques but also ensured wave mode filtering can be applied to thicker composite structures in the future, where smaller wavelength changes correlate to larger thickness changes.

A further significant step toward real world application was made by extending the proposed techniques to geometrically complex parts. Attempts had been made to expand wavenumber based techniques to complex geometries [40, 100]. These did however not prove adequate solutions to allow wavenumber based damage techniques to be practically expanded to parts with complex geometries. The requirement for prior knowledge of the parts geometry and orientation to the measurement device was a significant limitation. By implementing wavefield measurements using a 3D SLDV these limitations were overcome. The errors introduced by assuming surfaces as being flat were also clearly demonstrated. By mapping wavefields onto a 2D plane and minimising distortion of length features it was shown that good results can be obtained even when given a non-developable surface geometry. This work demonstrated the feasibility of this technique to be applied to real world parts in quality control testing as well as in service testing.

8.2 Conclusions

In this work methods were presented that enable damage to be effectively detected in a range of different materials and material thicknesses. The use of Rayleigh-Lamb equations to determine mode filters for multi-frequency narrow band filtering was shown to offer a fast and quantitative way to both detect damage and also identify geometric features. The concept of narrow band mode filtering was developed and demonstrated on two specimens, showing it to be capable of giving a good estimate of thickness. When a large number of thickness changes were introduced over a large thickness range it substantially outperformed other single frequency wavenumber filtering techniques and again produced an accurate estimate of thickness. This comparison also highlighted the inherent limitations faced by single frequency exci-

tation especially when considering parts with thickness greater than 5mm.

A 3D SLDV was used to investigate the dispersive behaviour of a number of carbon composite plates with different fibre layups. The dispersive nature of the materials were compared by analysing both in-plane and out-of-plane data in the frequency domain. This work showed that for highly non-isotropic materials the wavenumber-frequency relationship changed over different angles. Likewise the wavenumber of the dominant A_0 mode was shown to undergo large changes at a given frequency and material thickness depending on the dispersion direction. While dispersion behaviour was observed to be highly complex and vary greatly between different specimens a few key characteristics were identified. For a given frequency the wavenumber varied over different dispersion angles for non-isotropic materials. It was also observed that the gradient of the wavenumber-frequency relationship did not vary greatly over different dispersion angles.

Using these insights the concept of mode filtering was successfully extend to composite materials or any material with unknown properties. This was achieved by removing the reliance on theoretical dispersion relations and instead determining the wavenumber and dispersion angle relationship as well as wavenumber-frequency relationship from the frequency domain measurement data itself. In the frequency domain Canny edge detection was applied to identify the dominant A_0 energy band. Using Canny edge detection rather than identifying areas of high energy ensured this method would be applicable to structures with large thickness ranges where energy bands in the frequency domain are not confined to a distinct area.

The novel mode filtering technique was then shown to be able to identify areas of varying thickness on a range of materials without any prior knowledge of the material or their dispersion characteristics. The technique was demonstrated on a number of different composite materials. In a carbon composite made from twill weave it was clearly able to identify and size a delamination defect and identified the uniform thickness of the rest of the material correctly. It was also shown to be highly effective when tested on a fibre glass specimen with all fibres arranged in a single direction, giving highly isotropic material properties. Single ply thickness changes were identified and areas of the same thickness in different areas of the specimen were correctly identified as such. The use of multiple excitation sources for the generation of a steady-state excitation was also demonstrated on this specimen. This method was shown to be effective in evaluating advanced materials such as GLARE. Multiple transducers were again used to generate a steady-state excitation in the large structure. The high attenuation of these materials was shown to cause low propagation is likely to have reduced the signal-to-noise ratio suggesting results can be further improved. The multiple sources also served to offer a more complete data set in the frequency domain by driving energy over multiple propagation angles,

allowing various relationships to be determined. With a future view of expanding this technique to large structures without boundaries that cause wave reflection, this is of particular importance.

To realise this process on real world structures a final package of work was undertaken to allow these algorithms to be applied to geometrically complex parts. Through the use of the positional coordinate data gathered by the 3D SLDV at each measurement point, it was shown that an adequate estimation of the parts geometry could be gained. Using this geometric information along with an ARAP mapping algorithm the wavefield was mapped onto a 2D plane with limited distortion of length features. A curved aluminium plate and an aluminium panel from a Hawk jet were measured and had wave mode filtering applied to them assuming a flat surface. The error in thickness estimate this caused was clear and significant. By mapping the wavefields to a 2D plane it was shown that length features of the waves were correctly recreated giving accurate and consistent thickness estimates over the specimens. As before, steady-state and multi-source excitation was utilised. Using monogenic signal analysis a local amplitude map was generated from the steady-state wavefield. This map showed great spatial resolution and accurately identified stepped thickness changes in the material. Canny edge detection was applied to identify these changes. They were then overlaid onto the thickness maps giving positional data of where edge features are present. Not only does this help align any measurement with known geometric information of the part but it also helps clarify any areas where the thickness map was not able to accurately represent stepped thickness changes. For isotropic materials wave mode filtering was shown as a feasible real world solution for structures with ether complex or plate like geometry. Good material thickness representation was shown and low sensitivity to different transducers and transducer placement was also demonstrated. The proven use of multiple transducers would also help in future applications on large structures. While composites represented a greater challenge the use of mode based filtering was shown to be able to give highly accurate thickness estimates, showing thinning from damage such as delamination. It was however shown that obtaining a direct measure of material thickness would be challenging to achieve. For industry application it would be expected that some detail of the part would be known. The relative thickness map which was demonstrated in this work could be used in conjunction with knowledge of the part to easily identify and locate variations and damage.

8.3 Future work

For isotropic structures further investigation into window shape and width shows promise in improving results. The direct relation between spatial and depth res-

olution was shown. An adaptive windowing technique could be applied to mode filtering whereby the different filter widths are applied in different regions depending on material thickness and local thickness changes.

The thickness given to each pixel is currently also assigned solely by the thickness of the filter which maximises energy at that point. By considering the energy levels in the other filters and the prevalence of the filter that holds the most energy, it may be possible to identify pixels being assigned a thickness with lower certainty. Likewise areas near stepped thickness changes could be identified using this method.

Furthermore, no work was completed to investigate the frequency ranges used for excitation. While a broad frequency range was used, measurements might be improved by using different frequency ranges. A narrower frequency range would allow more energy to be driven into the specimens at the chosen frequencies. By testing a number of frequencies at a range of sample points an optimum excitation frequency could be established. It could also be beneficial to drive the transducer with a signal that does not have a linear frequency amplitude relation. That is to say flatter frequency characteristics could be produced by driving the transducer at a lower amplitude at its resonance frequencies and a higher amplitude at frequencies where it showed less resonance. While this would require prior knowledge of the transducer and its frequency response it may offer more consistent and accurate results over materials of different thickness ranges.

While this work emphasised improving wavefield based techniques for thicker materials there is an inherent limitation when using the dominant A_0 mode. Within usable frequency ranges the wavelength changes will be very small for a given thickness change at large material thicknesses. At these same frequency thickness ranges the in-plane S_0 mode starts to show large changes in wavelength for a given thickness change. It is therefore expected that mode filtering could be expanded to use the S_0 mode's larger frequency thickness products given found in thicker structures. By considering a material with broad thickness ranges a system that includes filters for multiple modes could be considered.

A further area not covered in this work is adhesive joints. The demonstrated ability of mode filtering to be able to determine defects, such as delamination defects indicates that adhesive joints could also be successfully imaged using this method. While other work has used full non-contact setups, where energy is being driven into the structure though air coupled or laser based ultrasound a lack of access to this instrumentation prevented this from being demonstrated with mode filtering. The comparison between different transducers in Chapter 3.1 does show that mode filtering is not particularly sensitive to the frequency characteristics of the driving transducers. The use of different excitation methods could offer better results if more energy can be driven into the structure, improving signal-to-noise ratio.

When investigating the dispersion behaviour of non-isotropic materials it was noted that the wavenumber-frequency relationship varies over different angles of propagation. If enough energy were to be driven into the specimen it would be possible to determine the wavenumber-frequency relationship at different propagation angles and build mode filters to reflect this behaviour. This would further help to increase the accuracy of this method for non-isotropic materials. It would require ether high amplitude steady-state excitation or multiple transducers to generate high levels of energy in a broad range of propagation directions.

The frequency domain data could foreseeably also be used to determine the approximate material characteristics or even layup by comparing the measured dispersion characteristics with ones modeled for likely materials. When combining this information with a single point of known material thickness a true thickness map could be achieved for composite materials.

The methods in this work represent a significant step towards realising wavenumber based damage detection techniques in real world applications. By implementing the techniques presented with a measurement setup optimised for speed, parts of unknown material and geometry can be measured and defects identified.

On the basis of this work an EPSRC grant was submitted. A final system is to be demonstrated that can complete fast and automated measurements of large and geometrically complex composite structures such as a wind turbine blade. To achieve automation a 3D SLDV is to be mounted on a robot arm with a second arm controlling the placement of an air coupled transducer. Through further optimisation of wave mode filtering the detailed information gained is to be used to update an FEA model of the part being examined to give insight into how any deviation from the planned design or damage might effect performance. By applying methods such as compressive sensing, processing speed can also to be substantially improved. Visualisation of these large data sets is to be aided by virtual reality and augmented reality technologies. The final system will offer significant improvements to how NDT is performed on large composite. The deep insight gained will have the potential to drive a step change in how NDT is performed and drive data based quality control.

9. References

[1] C. R. Farrar and K. Worden. "An introduction to structural health monitoring". In: *Philosophical transactions of the Royal Society of London. Series A: Mathematical, physical, and engineering sciences* 365.1851 (2007), pp. 303–315. ISSN: 1364-503X.

[2] K. Worden and J. M. Dulieu-Barton. "An Overview of Intelligent Fault Detection in Systems and Structures". In: *Structural Health Monitoring* 3.1 (2004), pp. 85–98. ISSN: 14759217. DOI: 10.1177/1475921704041866.

[3] B. Hull and V. John. *Non-Destructive Testing*. Frist. London: British Library Cataloguing in Publication Data, 1988.

[4] Q. Y. Lu and C. H. Wong. "Additive manufacturing process monitoring and control by non-destructive testing techniques: challenges and in-process monitoring". In: *Virtual and Physical Prototyping* 13.2 (2018), pp. 39–48. ISSN: 17452767. DOI: 10.1080/17452759.2017.1351201.

[5] E. Baravelli, M. Senesi, M. Ruzzene, and L. De Marchi. "Fabrication and characterization of a wavenumber-spiral frequency-steerable acoustic transducer for source localization in plate structures". In: *IEEE Transactions on Instrumentation and Measurement* 62.8 (2013), pp. 2197–2204. ISSN: 00189456. DOI: 10.1109/TIM.2013.2255992.

[6] A. S. Purekar and D. J. Pines. "Damage detection in thin composite laminates using piezoelectric phased sensor arrays and guided lamb wave interrogation". In: *Journal of Intelligent Material Systems and Structures* 21.10 (2010), pp. 995–1010. ISSN: 1045389X. DOI: 10.1177/1045389X10372003.

[7] L. Qiu, B. Liu, S. Yuan, and Z. Su. "Impact imaging of aircraft composite structure based on a model-independent spatial-wavenumber filter". In: *Ultrasonics* 64 (2016), pp. 10–24. ISSN: 0041624X. DOI: 10.1016/j.ultras.2015.07.006. URL: http://dx.doi.org/10.1016/j.ultras.2015.07.006.

[8] Y. Ren, L. Qiu, S. Yuan, and Z. Su. "A diagnostic imaging approach for online characterization of multi-impact in aircraft composite structures based on a scanning spatial-wavenumber filter of guided wave". In: *Mechanical Systems and Signal Processing* 90 (2017), pp. 44–63. ISSN: 10961216. DOI: 10.1016/j.ymssp.2016.12.005. URL: http://dx.doi.org/10.1016/j.ymssp.2016.12.005.

[9] M. D. Rogge and C. A. Leckey. "Characterization of impact damage in composite laminates using guided wavefield imaging and local wavenumber domain analysis". In: *Ultrasonics* 53.7 (Sept. 2013), pp. 1217–1226. DOI: 10.1016/j.ultras.2012.12.015. URL: http://dx.doi.org/10.1016/j.

ultras.2012.12.015%20https://linkinghub.elsevier.com/retrieve/pii/S0041624X13000607.

[10] E. B. Flynn, J. Lee, G. Jarmer, and G. Park. "Frequency-wavenumber processing of laser-excited guided waves for imaging structural features and defects". In: *6th European Workshop on Structural Health Monitoring* (2012), pp. 1–8. URL: http://ndt.net/article/ewshm2012/papers/th2e3.pdf.

[11] L. Yu, C. A. Leckey, and Z. Tian. "Study on crack scattering in aluminum plates with Lamb wave frequency-wavenumber analysis". In: *Smart Materials and Structures* 22.6 (2013). ISSN: 09641726. DOI: 10.1088/0964-1726/22/6/065019.

[12] E. B. Flynn, S. Y. Chong, G. J. Jarmer, and J. R. Lee. "Structural imaging through local wavenumber estimation of guided waves". In: *NDT and E International* 59 (2013), pp. 1–10. ISSN: 09638695. DOI: 10.1016/j.ndteint.2013.04.003. URL: http://dx.doi.org/10.1016/j.ndteint.2013.04.003.

[13] N. Malhotra, P. K. Shah, P. Kumar, P. Acharya, S. Panchal, and J. Malhotra. *Ultrasound in Obstetrics & Gynecology*. FOGSI publication. Jaypee Brothers,Medical Publishers Pvt. Limited, 2014. ISBN: 9789351521587. URL: https://books.google.co.uk/books?id=q74DBAAAQBAJ.

[14] J. L. Rose. *Ultrasonic Waves in Solid Media*. First. Cambridge: The Press syndicate of the university of Cambridge, 1999. ISBN: 0521548896.

[15] A. Raghavan and C. E. Cesnik. *Lamb-Wave Based Structural Health Monitoring*. 2005, pp. 235–258. ISBN: 9780470869079. DOI: 10.1002/0470869097.ch11.

[16] J. L. Rose. *Ultrasonic Guided Waves in Solid Media*. First. New York: Cambridge University Press, 2014. ISBN: 978-1-10704895-9.

[17] W. Gao, C. Glorieux, and J. Thoen. "Laser ultrasonic study of Lamb waves: Determination of the thickness and velocities of a thin plate". In: *International Journal of Engineering Science* 41.2 (2003), pp. 219–228. ISSN: 00207225. DOI: 10.1016/S0020-7225(02)00150-7.

[18] A. Kamal and V. Giurgiutiu. "Stiffness Transfer Matrix Method (STMM) for stable dispersion curves solution in anisotropic composites". In: *Health Monitoring of Structural and Biological Systems 2014*. Vol. 9064. 2014, p. 906410. ISBN: 9780819499905. DOI: 10.1117/12.2044789.

[19] B. Pavlakovic and M. Lowe. "Disperse: A General Purpose Program for Creating Dispersion Curves". In: *Review of Progress in Quantitative Nondestructive Evaluation*. Springer, Boston, MA, 1997, pp. 185–192.

[20] A. Nayfeh. "General Layered Media". In: *Wave Propagation in Layered Anisotropic Media, Volume 39 1st Edition*. North Holland: North-Holland, 1995. Chap. 9, pp. 117–133. ISBN: 9780080543734.

[21] L. Wang and F. G. Yuan. "SCIENCE AND Group velocity and characteristic wave curves of Lamb waves in composites : Modeling and experiments". In: *Composites Science and Technology* 67 (2007), pp. 1370–1384. DOI: 10.1016/j.compscitech.2006.09.023.

[22] W. H. Ong, N. Rajic, W. K. Chiu, and C. Rosalie. "Determination of the elastic properties of woven composite panels for Lamb wave studies". In: *Composite Structures* 141 (2016), pp. 24–31. ISSN: 0263-8223. DOI: 10.1016/j.compstruct.2015.12.017. URL: http://dx.doi.org/10.1016/j.compstruct.2015.12.017.

[23] M. Ruzzene, S. M. Jeong, T. E. Michaels, J. E. Michaels, and B. Mi. "Simulation and measurement of ultrasonic waves in elastic plates using laser vibrometry". In: *AIP Conference Proceedings* 760.August 2014 (2005), pp. 172–179. ISSN: 0094243X. DOI: 10.1063/1.1916675.

[24] S. Kumar, M. Vishwakarma, and P. Akhilesh. "ScienceDirect Advances and Researches on Non Destructive Testing : A Review". In: *Materials Today: Proceedings* 5.2 (2018), pp. 3690–3698. ISSN: 2214-7853. DOI: 10.1016/j.matpr.2017.11.620. URL: https://doi.org/10.1016/j.matpr.2017.11.620.

[25] Z. Su, L. Y. Ã, and Y. Lu. "Guided Lamb waves for identification of damage in composite structures : A review". In: *Journal of Sound and Vibration* 295.3-5 (2006), pp. 753–780. DOI: 10.1016/j.jsv.2006.01.020.

[26] K. K. Shung, J. M. Cannata, and Q. F. Zhou. "Piezoelectric materials for high frequency medical imaging applications: A review". In: *Journal of Electroceramics* 19.1 (2007), pp. 139–145. ISSN: 13853449. DOI: 10.1007/s10832-007-9044-3.

[27] H. Miao, Q. Huan, and F. Li. "Excitation and reception of pure shear horizontal waves by using face-shear d24 mode piezoelectric wafers". In: April (2016). ISSN: 10897550. DOI: 10.1063/1.4948473.

[28] I. Babu and G. de With. "Highly flexible piezoelectric 0-3 PZT-PDMS composites with high filler content". In: *Composites Science and Technology* 91 (2014), pp. 91–97. ISSN: 02663538. DOI: 10.1016/j.compscitech.2013.11.027. URL: http://dx.doi.org/10.1016/j.compscitech.2013.11.027.

[29] G. Haghiashtiani and M. A. Greminger. "Fabrication , polarization , and characterization of PVDF matrix composites for integrated structural load sensing". In: *Smart Materials and Structures* 24.4 (2015), p. 45038. ISSN: 1361-665X. DOI: 10.1088/0964-1726/24/4/045038. URL: http://dx.doi.org/10.1088/0964-1726/24/4/045038.

[30] C. Rosen Z. and V. Basavaraj, eds. *Key Papers in Physics: PIEZOELECTRICITY*. New York: American Institute of Physics, 1992. ISBN: 0-88318-647-0.

[31] S. Cochran. "Piezoelectricity and basic configurations for piezoelectric ultrasonic transducers". In: *Ultrasonic Transducers: Materials and Design for Sensors, Actuators and Medical Applications* (2012), pp. 3–35. DOI: 10.1533/9780857096302.1.3.

[32] J. A. Jim and J. G. Espa. "The implementation of the acoustic impedance for the monitoring of industrial processes". In: *Communication, Journal O F Computer-mediated* 9.February 2017 (2012), pp. 1343–1350.

[33] D. Callens, C. Bruneel, and J. Assaad. "Matching ultrasonic transducer using two matching layers where one of them is glue". In: *NDT and E International* 37.8 (2004), pp. 591–596. ISSN: 09638695. DOI: 10.1016/j.ndteint.2004.03.005.

[34] A. Safari and E. Koray Akdogan. *Piezoelectric and Acoustic Materials for Transducer Applications*. New York: Springer Science+Business Media, 2008.

[35] K. Nakamura. *Electrical evaluation of piezoelectric transducers*. Woodhead Publishing Limited, 2012, pp. 264–276. ISBN: 9781845699895. DOI: 10.1533/9780857096302.2.264. URL: http://dx.doi.org/10.1533/9780857096302.2.264.

[36] G. Kaduchak, D. N. Sinha, D. C. Lizon, and M. J. Kelecher. "A non-contact technique for evaluation of elastic structures at large stand-off distances: Applications to classification of fluids in steel vessels". In: *Ultrasonics* 37.8 (2000), pp. 531–536. ISSN: 0041624X. DOI: 10.1016/S0041-624X(99)00109-2.

[37] M. D. Espinosa and F. R. "Piezoelectric transducers for air-coupled operation in the frequency range 0.3-2.5 mhz." In: *Ultrasonics* (), pp. 3–8.

[38] M. Johansmann and G. Wirth. *Laser Doppler vibrometry for measuring vibration in ultrasonic transducers*. Woodhead Publishing Limited, 2012, pp. 277–313. ISBN: 9781845699895. DOI: 10.1533/9780857096302.2.277. URL: http://dx.doi.org/10.1533/9780857096302.2.277.

[39] W. J. Staszewski, B. C. Lee, and R. Traynor. "Fatigue crack detection in metallic structures with Lamb waves and 3D laser vibrometry". In: *Measurement Science and Technology* 18.3 (2007), pp. 727–739. ISSN: 13616501. DOI: 10.1088/0957-0233/18/3/024.

[40] E. A. C. Koskelo and E. B. Flynn. "Full-field inspection of three-dimensional structures using steady-state acoustic wavenumber spectroscopy". In: *AIP Conference Proceedings* 1806 (2017). ISSN: 15517616. DOI: 10.1063/1.4974547.

[41] Y. Shen and C. E. S. Cesnik. "Hybrid local FEM/global LISA modeling of guided wave propagation and interaction with damage in composite structures". In: *Proc. of SPIE* 9438.734 (2015), 94380J. ISSN: 1996756X. DOI: 10.1117/12.2083346. URL: http://proceedings.spiedigitallibrary.org/proceeding.aspx?doi=10.1117/12.2083346.

[42] S. Pierce, B. Culshaw, and Q. Shan. "Laser generation of ultrasound using a modulated continuous wave laser diode". In: *Applied Physics Letters* 1030.December 1997 (1998), pp. 27–30. DOI: 10.1063/1.120955.

[43] N. Hosoya, A. Yoshinaga, A. Kanda, and I. Kajiwara. "Non-contact and non-destructive Lamb wave generation using laser-induced plasma shock wave". In: *International Journal of Mechanical Sciences* 140.September 2017 (2018), pp. 486–492. ISSN: 00207403. DOI: 10.1016/j.ijmecsci.2018.03.023. URL: https://doi.org/10.1016/j.ijmecsci.2018.03.023.

[44] T. W. Murray and J. W. Wagner. "Thermoelastic and Ablative Generation of Ultrasound: Source Effects". In: *Review of Progress in Quantitative Nondestructive Evaluation* 17 (1998), pp. 619–625. DOI: 10.1007/978-1-4615-5339-7{_}80.

[45] R. Yang, Y. He, and H. Zhang. "Progress and trends in nondestructive testing and evaluation for wind turbine composite blade". In: *Renewable and Sustainable Energy Reviews* 60.July (2016), pp. 1225–1250. ISSN: 18790690. DOI: 10.1016/j.rser.2016.02.026.

[46] J. Blitz and G. Simpson. *Ultrasonic Methods of Non-destructive Testing*. First. London: Chapman & Hall, 1996. ISBN: 0412604701.

[47] S. Gholizadeh. "A review of non-destructive testing methods of composite materials". In: *Procedia Structural Integrity* 1 (2016), pp. 50–57. ISSN: 24523216. DOI: 10.1016/j.prostr.2016.02.008. URL: http://dx.doi.org/10.1016/j.prostr.2016.02.008.

[48] S. Pudovikov, A. Bulavinov, and R. Pinchuk. "Innovative ultrasonic testing (UT) of nuclear components by sampling phased array with3D visualization of ..." In: February 2016 (2016).

[49] W. Bisle, T. Meier, S. Mueller, and S. Rueckert. "In-Service Inspection Concept for GLARE ® – An Example for the Use of New UT Array In- spection Systems". In: *EC NDT* (2006), pp. 1–9.

[50] M. Jolly, A. Prabhakar, B. Sturzu, K. Hollstein, R. Singh, S. Thomas, P. Foote, and A. Shaw. "Review of Non-destructive Testing (NDT) Techniques and their Applicability to Thick Walled Composites". In: *Procedia CIRP* 38.December (2015), pp. 129–136. ISSN: 22128271. DOI: 10.1016/j.procir.2015.07.043. URL: http://dx.doi.org/10.1016/j.procir.2015.07.043.

[51] V. P. Vavilov and D. D. Burleigh. "Review of pulsed thermal NDT: Physical principles, theory and data processing". In: *NDT and E International* 73 (2015), pp. 28–52. DOI: 10.1016/j.ndteint.2015.03.003. URL: http://dx.doi.org/10.1016/j.ndteint.2015.03.003.

[52] F. Wang, J. Liu, O. Mohummad, and Y. Wang. "Experimental Study on GFRP Surface Cracks Detection Using Truncated-Correlation Photothermal Coherence Tomography". In: *International Journal of Thermophysics* 39.4 (2018), pp. 1–10. ISSN: 0195928X. DOI: 10.1007/s10765-018-2370-7. URL: https://doi.org/10.1007/s10765-018-2370-7.

[53] S. K. Dwivedi, M. Vishwakarma, and P. A. Soni. "Advances and Researches on Non Destructive Testing: A Review". In: *Materials Today: Proceedings* 5.2 (2018), pp. 3690–3698. ISSN: 22147853. DOI: 10.1016/j.matpr.2017.11.620. URL: https://doi.org/10.1016/j.matpr.2017.11.620.

[54] P. D. Welch. *The Fast Fourier Transform and Its Applications by E. Oran Brigham*. Vol. 12. 1. 1988, pp. 27–34. ISBN: 0133075052.

[55] M. Johansson. "The Hilbert transform". In: *October* 19.1 (2006), pp. 1–12. ISSN: 14726963. DOI: 10.1186/1472-6963-9-90. URL: http://www.fuchs-braun.com/media/d9140c7b3d5004fbffff8007fffffff0.pdf.

[56] K. Langley and S. J. Anderson. "The Riesz transform and simultaneous representations of phase, energy and orientation in spatial vision\\". In: *Vision Research* 50.17 (2010), pp. 1748–1765. ISSN: 00426989. DOI: 10.1016/j.visres.2010.05.031. URL: http://dx.doi.org/10.1016/j.visres.2010.05.031.

[57] C. P. Bridge. "Introduction To The Monogenic Signal". In: (2017), pp. 1–21. URL: http://arxiv.org/abs/1703.09199.

[58] J. Rao, M. Ratassepp, and Z. Fan. "Limited-view ultrasonic guided wave tomography using an adaptive regularization method". In: *Journal of Applied Physics* 120.19 (2016). DOI: 10.1063/1.4967790. URL: http://dx.doi.org/10.1063/1.4967790.

[59] Y. K. An, Z. Shen, and Z. Wu. "Stripe-PZT sensor-based baseline-free crack diagnosis in a structure with awelded stiffener". In: *Sensors (Switzerland)* 16.9 (2016). ISSN: 14248220. DOI: 10.3390/s16091511.

[60] M. Ruzzene. "Frequency-wavenumber domain filtering for improved damage visualization". In: *AIP Conference Proceedings* 894 (2007), pp. 1556–1563. ISSN: 0094243X. DOI: 10.1063/1.2718150.

[61] T. E. Michaels, J. E. Michaels, and M. Ruzzene. "Frequency-wavenumber domain analysis of guided wavefields". In: *Ultrasonics* 51.4 (2011), pp. 452–466. ISSN: 0041624X. DOI: 10.1016/j.ultras.2010.11.011. URL: http://dx.doi.org/10.1016/j.ultras.2010.11.011.

[62] O. Mesnil, C. a. Leckey, and M. Ruzzene. "Instantaneous and local wavenumber estimations for damage quantification in composites". In: *Structural Health Monitoring* (2014), pp. 1–12. ISSN: 1475-9217. DOI: 10.1177/1475921714560073.

[63] L. Yu, Z. Tian, and C. A. Leckey. "Crack imaging and quantification in aluminum plates with guided wave wavenumber analysis methods". In: *Ultrasonics* 62 (2015), pp. 203–212. ISSN: 0041624X. DOI: 10.1016/j.ultras.2015.05.019. URL: http://dx.doi.org/10.1016/j.ultras.2015.05.019.

[64] J. Y. Jeon, S. Gang, G. Park, E. Flynn, T. Kang, and S. Woo. "Damage detection on composite structures with standing wave excitation and wavenumber analysis". In: *Advanced Composite Materials* 3046.November (2017), pp. 1–13. ISSN: 0924-3046. DOI: 10.1080/09243046.2017.1313577. URL: https://doi.org/10.1080/09243046.2017.1313577.

[65] E. B. Flynn. "Embedded Multi-Tone Ultrasonic Excitation and Continuous-Scanning Laser Doppler Vibrometry for Rapid and Remote Imaging of Structural Defects". In: *7th European Workshop on Structural Health Monitoring* (2014), pp. 1561–1567.

[66] P. D. Juarez and C. A. C. Leckey. "Multi-frequency local wavenumber analysis and ply correlation of delamination damage". In: *Ultrasonics* 62 (2015), pp. 56–65. ISSN: 0041624X. DOI: 10.1016/j.ultras.2015.05.001. URL: http://dx.doi.org/10.1016/j.ultras.2015.05.001.

[67] O. Mesnil, H. Yan, M. Ruzzene, and K. Paynabar. "Fast wavenumber measurement for accurate and automatic location and quantification of defect in composite". In: *Structural Health Monitoring* 15 (2016). DOI: 10.1177/1475921716636375.

[68] G. Fan, H. Zhang, H. Zhang, W. Zhu, and X. Chai. "Lamb Wave Local Wavenumber Approach for Characterizing Flat Bottom Defects in an Isotropic Thin Plate". In: *Applied Sciences* 8.9 (2018), p. 1600. ISSN: 2076-3417. DOI: 10.3390/app8091600. URL: http://www.mdpi.com/2076-3417/8/9/1600.

[69] S. Kang, E. B. Flynn, J. Jeon, and G. Park. "Damage Detection on Thin Walled Structures With Single Frequency Excitation and Wavenumber Filtering". In: *8th European Workshop On Structural Health Monitoring (EWSHM 2016)* (2016), pp. 1–10.

[70] D. H. Kim, J. Y. Jeo, G. H. Park, T. Kang, and S. W. Han. "Thickness estimation of damages using laser scanning sensing and 2-D wavelet wavenumber filtering". In: *Journal of The Korean Society for Nondestructive Testing* 37.5 (2017), pp. 310–318. DOI: 10.7779/jksnt.2017.37.5.310.

[71] J. Y. Jeon, H. K. Jung, D. H. Kim, G. Park, T. Kang, and S. W. Han. "Experimental study on guided and standing waves based full field laser scanning for damage detection". In: *9th European Workshop on Structural Health Monitoring, EWSHM 2018* (2018), pp. 1–12.

[72] C. Gonnet, B. Torrésani, C. Gonnet, B. Torrésani, and L. Frequency. "Local Frequency Analysis with Two-Dimensional Wavelet Transform To cite this version : HAL Id : hal-01739702". In: (2018).

[73] T. C. Truong and J. R. Lee. "Thickness reconstruction of nuclear power plant pipes with flow-accelerated corrosion damage using laser ultrasonic wavenumber imaging". In: *Structural Health Monitoring* 17.2 (2018), pp. 255–265. ISSN: 17413168. DOI: 10.1177/1475921716689733.

[74] J. E. Michaels, S. J. Lee, A. J. Croxford, and P. D. Wilcox. "Chirp excitation of ultrasonic guided waves". In: *Ultrasonics* 53.1 (Jan. 2013), pp. 265–270. ISSN: 0041-624X. DOI: 10.1016/J.ULTRAS.2012.06.010. URL: https://www.sciencedirect.com/science/article/abs/pii/S0041624X12001333?via%3Dihub.

[75] K. Ono and A. Gallego. "Attenuation of Lamb Waves in CFRP Plates". In: *Journal of Acoustic Emission* 30.August (2012), pp. 109–124.

[76] A. Norton. *Dynamic Fields and Waves*. First Edit. Milton Keynes: The Open University, 2000.

[77] D. N. Alleyne and P. Cawley. "The Interaction of Lamb Waves with Defects". In: *IEEE Transactions on Ultrasonics, Ferroelectrics, and Frequency Control* 39.3 (1992), pp. 381–397. ISSN: 08853010. DOI: 10.1109/58.143172.

[78] E. B. Flynn and N. D. Stull. "Toward Utilizing Full-Field Laser-Ultrasound for Practical Nondestructive Inspection with Acoustic Wavenumber Spectroscopy". In: *2018 IEEE International Ultrasonics Symposium (IUS)*. IEEE, Oct. 2018, pp. 1–7. ISBN: 978-1-5386-3425-7. DOI: 10.1109/ULTSYM.2018.8579833. URL: https://ieeexplore.ieee.org/document/8579833/.

[79] F. Harris. "On the use of windows for harmonic analysis with the discrete Fourier transform". In: *Proceedings of the IEEE* 66.1 (1978), pp. 51–83. DOI: 10.1109/PROC.1978.10837. URL: http://ieeexplore.ieee.org/lpdocs/epic03/wrapper.htm?arnumber=1455106.

[80] D. R. Lide. *CRC Handbook of Chemistry and Physics*. Internet V. Boca Raton, FL, CRC Press, 2005. URL: http://www.hbcpnetbase.com.

[81] P. Dierckx. "An Algorithm for Surface-Fitting with Spline Functions". In: *IMA Journal of Numerical Analysis* 1.3 (1981), pp. 267–283.

[82] M. Bansal, R. Sharma, and P. Grover. "Performance evaluation of Butterworth Filter for Signal Denoising". In: *International Journal of Electronics & Communication Technology* 1.Dec (2010), pp. 1–5. DOI: 10.13140/RG.2.1.4809.8161.

[83] M. Felsberg and G. Sommer. "The monogenic signal". In: *IEEE Transactions on Signal Processing* 49.12 (2001), pp. 3136–3144. ISSN: 1053587X. DOI: 10.1109/78.969520.

[84] M. Felsberg and G. Sommer. "The monogenic scale-space: A unifying approach to phase-based image processing in scale-space". In: *Journal of Mathematical Imaging and Vision* 21.1 (2004), pp. 5–26. ISSN: 09249907. DOI: 10.1023/B:JMIV.0000026554.79537.35.

[85] M. Hidalgo-Gato and V. C. F. Barbosa. *The monogenic signal of potential-field data: A Python Implementation*. 2017. DOI: 10.1190/GEO2016-0099.1.. URL: https://github.com/pinga-lab/paper-monogenic-signal.

[86] E. B. Flynn and G. S. Jarmer. "High-Speed, Non-Contact, Baseline-Free Imaging of Hiddden Defects Using Scanning Laser Measurements of Steady-State Ultrasonic Vibration". In: *9th International Workshop on Structural Health MonitoringVolume: 1*. 9th International Workshop on Structural Health MonitoringVolume: 1. 2013.

[87] H. Lamb. "On Waves in an Elastic Plate". In: *Journal of Applied Mathematics and Mechanics* 24.3 (1917), pp. 640–652. ISSN: 00218928. DOI: 10.1016/0021-8928(60)90171-4.

[88] A. C. Bovik and S. T. Acton. *Basic Linear Filtering with Application to Image Enhancement*. 1st ed. Vol. 2. Elsevier, 2009, pp. 225–239. ISBN: 9780123744579. DOI: 10.1016/B978-0-12-374457-9.00010-X. URL: http://dx.doi.org/10.1016/B978-0-12-374457-9.00010-X.

[89] A. Gallina, L. Ambrozinski, P. Packo, L. Pieczonka, T. Uhl, and W. J. Staszewski. "Bayesian parameter identification of orthotropic composite materials using Lamb waves dispersion curves measurement". In: *Journal of Vibration and Controll* 26.April 2015 (2017). DOI: 10.1177/1077546315619264.

[90] M. Kersemans, N. Lammens, W. Van Paepegem, K. Van Den Abeele, L. Pyl, F. Zastavnik, H. Sol, and J. Degrieck. "Efficient extraction of the directional wave curves from a pulsed ultrasonic polar scan experiment". In: *12th International Conference of the Slovenian Society for Non-Destructive Testing: Application of Contemporary Non-Destructive Testing in Engineering, ICNDT 2013 - Conference Proceedings* (2013), pp. 171–178.

[91] A. R. Nandyala, A. K. Darpe, and S. P. Singh. "Effective stiffness matrix method for predicting the dispersion curves in general anisotropic composites". In: *Archive of Applied Mechanics* 89.9 (2019), pp. 1923–1938. ISSN: 14320681. DOI: 10.1007/s00419-019-01552-x. URL: https://doi.org/10.1007/s00419-019-01552-x.

[92] M. Stévenin, A. Lhémery, and S. Grondel. "An efficient model to predict guided wave radiation by finite-sized sources in multilayered anisotropic plates with account of caustics". In: *Journal of Physics: Conference Series* 684.1 (2016). ISSN: 17426596. DOI: 10.1088/1742-6596/684/1/012004.

[93] J. Canny. "A Computational Approach to Edge Detection". In: *IEEE TRANSACTIONS ON PATTERN ANALYSIS AND MACHINE INTELLIGENCE* PAMI-8.6 (1986).

[94] J. Matas, C. Galambos, and J. Kittler. "Progressive Probabilistic Hough Transform". In: *British Machine Vision Conf., Southampton* (1998), pp. 1–26. DOI: 10.5244/c.12.26.

[95] G. Bradski. "The OpenCV Library". In: *Dr. Dobb's Journal of Software Tools* (2000).

[96] V. Iglovikov, S. Mushinskiy, and V. Osin. "Satellite Imagery Feature Detection using Deep Convolutional Neural Network: A Kaggle Competition". In: (2017). URL: http://arxiv.org/abs/1706.06169.

[97] H.-y. Chang. "Damage imaging in a stiffened curved composite sandwich panel with wavenumber index via Riesz transform". In: *Structural Health Monitoring* (2019). DOI: 10.1177/1475921719858432.

[98] P. Helmut and W. Johannes. *Computational Line Geometry*. Berlin: Springer Berlin Heidelberg, 2001. ISBN: 9783540420583.

[99] T. Kang, S. J. Han, S. Moon, S. Han, J. Y. Jeon, and G. Park. "Lamb-wave sparse-frequency interdigital-transducer-based scanning laser Doppler vibrometry for quantitative depth-wise visualization of defects in plates". In: *NDT and E International* 107.May (2019), p. 102137. ISSN: 09638695. DOI: 10.1016/j.ndteint.2019.102137. URL: https://doi.org/10.1016/j.ndteint.2019.102137.

[100] J. Spytek, J. Mrowka, L. Pieczonka, and L. Ambrozinski. "Multi-resolution non-contact damage detection in complex-shaped composite laminates using ultrasound". In: *NDT and E International* 116.September (2020), p. 102366. ISSN: 09638695. DOI: 10.1016/j.ndteint.2020.102366. URL: https://doi.org/10.1016/j.ndteint.2020.102366.

[101] T. Gao, H. Sun, Y. Hong, and X. Qing. "Hidden corrosion detection using laser ultrasonic guided waves with multi-frequency local wavenumber estimation". In: *Ultrasonics* 108.December 2019 (2020), p. 106182. ISSN: 0041624X. DOI: 10.1016/j.ultras.2020.106182. URL: https://doi.org/10.1016/j.ultras.2020.106182.

[102] L. Liu, L. Zhang, Y. Xu, C. Gotsman, and S. J. Gortler. "A local/global approach to mesh parameterization". In: *Eurographics Symposium on Geometry Processing* 27.5 (2008), pp. 1495–1504. ISSN: 17278384.

[103] A. Jacobsonn, D. Panozzo, and Other. *libigl: A simple C++ geometry processing library*. 2018. URL: https://libigl.github.io/.

[104] J. Stillwell. *Geometry of Surfaces*. Ed. by E. J.H and F. Gehring. Second Edi. Stillwell1992: Springer-Verlag New York, Inc., 1992.